



Dipl.-Ing. Andrea Maier

**Orbit determination and gravity field recovery
from tracking data to geodetic satellites
and the Lunar Reconnaissance Orbiter**

DISSERTATION

zur Erlangung des akademischen Grades
Doktorin der technischen Wissenschaften
eingereicht an der

Technischen Universität Graz

Betreuer
Univ.-Prof. Dr.-Ing. Torsten Mayer-Gürr
Institut für Geodäsie

Graz, März 2015

EIDESSTATTLICHE ERKLÄRUNG

AFFIDAVIT

Ich erkläre an Eides statt, dass ich die vorliegende Arbeit selbstständig verfasst, andere als die angegebenen Quellen/Hilfsmittel nicht benutzt, und die den benutzten Quellen wörtlich und inhaltlich entnommenen Stellen als solche kenntlich gemacht habe. Das in TUGRAZonline hochgeladene Textdokument ist mit der vorliegenden Dissertation identisch.

I declare that I have authored this thesis independently, that I have not used other than the declared sources/resources, and that I have explicitly indicated all material which has been quoted either literally or by content from the sources used. The text document uploaded to TUGRAZonline is identical to the present doctoral dissertation.

Datum / Date

Unterschrift / Signature

For Hans-Peter Grahl,
with whom I am proud to share my love with.

Abstract

Artificial satellites orbiting planetary bodies are sensitive to a variety of gravitational and non-gravitational forces. This thesis focuses on the recovery of the long wavelengths of the Earth's and the Moon's gravity field using ground-based tracking data. Since the gravity field is derived from satellite perturbation, a major part of the thesis at hand is dedicated to precise orbit determination. As far as the Earth is concerned, the largest and hence most crucial gravity field coefficient is the dynamical flattening term C_{20} . It can be most precisely determined from two-way optical satellite laser ranges to geodetic satellites. Their simple spherical shape along with their large area-to-mass ratio minimize the disturbing effects of non-gravitational forces, which are difficult to model. Laser ranges to six geodetic satellites (LAGEOS-1/2, Ajisai, Stella, Starlette, Larets) were analyzed over a time span of almost 14 years (January 2000 to October 2013). On the one hand, a static gravity field solution was computed up to spherical harmonic degree and order 4. On the other hand, monthly sets of coefficients were estimated that reflect the temporal variability of the Earth's gravity field. Concerning the Moon, tracking data to the Lunar Reconnaissance Orbiter were analyzed. This satellite has been routinely tracked with optical one-way laser ranges to assist orbit determination; two-way Doppler range-rates represent the primary tracking data type. Orbit overlap tests were conducted to find the optimal parametrization. In total, 13 months of Doppler data (January 2011 to February 2012) were analyzed. Orbit overlap differences indicate an orbital precision of 13.8 m, 14.2 m, and 1.3 m in along track, cross track, and radial direction, respectively. The modeling of the satellites clock, which is necessary when the orbit shall be estimated using both tracking data types turned out to be a delicate issue. Approximating the clock's variation with a second-degree polynomial, which is supported by the software used, resulted in less precise orbits compared to those based on Doppler-only. Thus, the gravity field coefficients, which were estimated up to degree and order 60, are based solely on Doppler data.

Kurzfassung

Die Bahnen künstlicher Satelliten, die planetare Körper umkreisen, werden von gravitativen und nicht-gravitativen Kräften beeinflusst. Die vorliegende Arbeit behandelt die Bestimmung des langwelligen Anteiles des Schwerefeldes der Erde sowie des Mondes mittels Beobachtungen von Bodenstationen zu Satelliten. Da die Schwerefeldinformation aus Bahnstörungen abgeleitet wird, nimmt die präzise Bahnbestimmung eine zentrale Rolle ein. Im Fall der Erde ist der wichtigste (da numerisch größte) Schwerefeldkoeffizient der dynamische Abplattungsterm C_{20} . Dieser kann am genauesten mittels optischen Zweiweg-Laserdistanzmessungen zu geodätischen Satelliten bestimmt werden. Über einen Zeitraum von fast 14 Jahren (Jänner 2000 bis Oktober 2013) wurden Laserdistanzen zu sechs geodätischen Satelliten (LAGEOS-1/2, Ajisai, Stella, Starlette, Larets) analysiert. Es wurde einerseits eine statische Schwerefeldlösung bis zu sphärisch harmonischem Grad und Ordnung 4 berechnet, andererseits wurden monatliche Lösungen geschätzt welche die zeitliche Variabilität des Erdschwerefeldes widerspiegeln. Um Informationen über das Mondschwerefeld zu gewinnen, wurden Beobachtungen zum Lunar Reconnaissance Orbiter verwendet. Neben dem primären Beobachtungstyp Zweiweg-Dopplermessungen stehen optische Einweg-Laserdistanzmessungen zur Verfügung. Um die optimale Parametrisierung der Satellitenbahn zu eruieren wurden Bahndifferenzen in zeitlich überlappenden Bahnbögen untersucht. Die Trajektorie wurde zwischen Jänner 2011 und Februar 2012 aus Dopplermessungen berechnet. Die Bahndifferenzen in den Überlappungsbereichen lassen auf eine Präzision von 13.8 m in along-track, 14.2 m in cross-track, sowie 1.3 m in radialer Richtung schließen. Für die Schätzung der Bahn aus Doppler- und Lasermessungen gemeinsam muss die Satellitenuhr modelliert werden. Deren Approximation durch ein Polynom zweiten Grades, welches von der verwendeten Software unterstützt wird, resultierte jedoch in einer weniger präzisen Bahn verglichen mit jener die nur aus Dopplerdaten bestimmt wurde. Aus diesem Grund basieren die Schwerefeldkoeffizienten, welche bis Grad und Ordnung 60 geschätzt wurden, auf jener Bahn in deren Bestimmung ausschließlich Dopplermessungen eingeflossen sind.

Acknowledgments

First of all, I want to express my gratitude to my supervisor Dr.-Ing. Oliver Baur. The mixture of giving me a free hand and steering my thoughts into the right direction when I was stuck was just right. Further, I am indebted to Univ.-Prof. Dr.-Ing. Torsten Mayer-Gürr for asking questions that showed me more than once that I had not yet fully understood the core of things. I would also like to express my thanks to Prof. Dr. Adrian Jäggi who stepped in at short notice as an examiner and whose comments have improved this document a lot. Many thanks to my former colleagues at the Space Research Institute of the Austrian Academy of Sciences who gave me a warm welcome five years ago. Special thanks to Dr.techn. Sandro Krauss with who it was a pleasure to share an office with as well as numerous coffee breaks. Moreover, we did a great part of the satellite laser ranging analysis together in the framework of a project.

I also want to thank Dave Rowlands for his kind support concerning the NASA software package GEODYN II. Further, I appreciate Erwan Mazarico's help with the external attitude information for the Lunar Reconnaissance Orbiter and comments on my results. I am also grateful that Pieter Visser provided the Delft Lunar Albedo Model in spherical harmonic expansion.

My deep gratitude goes to my parents, Josef and Aurelia Maier, who supported me and endured my strained nerves. I would also like to thank my sisters Christiane Schiavinato and Martina Maier-Hirschl who gave me the joy of being an aunt of four great kids. Klara, Lorenz, Alice, and Laura, you are the best!

The one person who witnessed all ups and downs a PhD comes with is Hans-Peter Grahsl. Thank you for being at my side for the last twelve years. I have lost track how often you encouraged me to keep on and stay focused. I am sure you feel as much relieved as I do when I have finally managed it!

Contents

List of Figures	iii
List of Tables	vii
Nomenclature	ix
List of abbreviations	xvii
1 Introduction	1
2 Precise orbit determination	5
2.1 Force models	9
2.1.1 Acceleration due to gravitational forces	9
2.1.2 Acceleration due to non-gravitational forces	16
2.1.3 Empirical acceleration	26
2.2 Observation models	26
2.2.1 Observation model for geodetic satellites	27
2.2.2 Observation models for LRO	29
2.2.3 Station displacements	34
2.2.4 Media corrections	34
2.2.5 Relativistic light time correction	37
2.3 Least squares adjustment	38
2.4 Key issues and quality assessment	40
3 Gravity field recovery	43
4 Geodetic satellites	47
4.1 Data set	49
4.2 Parametrization and modeling	52
4.3 Results	56
4.3.1 Precise orbit determination	56
4.3.2 Gravity field	58

4.4	Discussion and conclusions	62
5	The Lunar Reconnaissance Orbiter	65
5.1	Tracking data	69
5.1.1	Optical laser ranges	69
5.1.2	Doppler range-rates	73
5.2	Simulation study	77
5.2.1	Setup	77
5.2.2	Results	79
5.2.3	Discussion and conclusions	85
5.3	Precise orbit determination	86
5.3.1	Finding the optimal parametrization	93
5.3.2	Results	96
5.4	Gravity field recovery	107
5.5	Discussion and conclusions	112
6	Discussion	115
	Bibliography	117
	Appendices	131
A	Computation of the light time τ	133
B	Weighting SLR measurements	135
C	LRO	137
C.1	Maneuvers	137
C.2	Dimensional layouts	141
D	Raw data conversions	145
D.1	From NPs to GEODYN format	145
D.2	From Doppler range-rates to GEODYN format	146
E	The SPICE module by NAIF	149

List of Figures

2.1	Zonal, tesseral, and sectorial spherical harmonic coefficients . . .	11
2.2	The lunar albedo model DLAM-1	23
2.3	Conical Earth shadow model	25
2.4	The motion of a geodetic satellite and a ground station during the signal travel time of two-way range measurements	27
2.5	Schematic view of the LRO laser ranging flight system	29
2.6	Center of mass correction for LRO	31
2.7	The motion of LRO and a ground station during the signal travel time of two-way Doppler measurements	33
2.8	The electromagnetic spectrum	35
4.1	Illustration of the LAGEOS-1 satellite	47
4.2	ILRS station network	48
4.3	Spatial distribution of NPs per satellite in January 2007	51
4.4	Number of NPs per laser station in January 2007	51
4.5	Estimated measurement biases per orbital arc from YARL to LAGEOS-1 and Starlette	56
4.6	RMS of post-fit range residuals and 10.7-cm solar radio flux	57
4.7	Monthly gravity field coefficients of degree 2	60
4.8	Degree-wise error amplitudes	61
5.1	Artist concept of LRO	65
5.2	Earth and Sun from LRO's perspective	68
5.3	Variation of the solar beta angle	69
5.4	'True', measured, and estimated distance between MDOL and LRO	71
5.5	Number of NPs	72
5.6	Range-rates and declination of LRO	73
5.7	Number of Doppler range-rates	74
5.8	Number of Doppler range-rates to LRO during the nominal mission phase, averaged over a $1^\circ \times 1^\circ$ grid	75

5.9	Time of observed laser ranges vs. time of observed Doppler range-rates per tracking station	76
5.10	Difference between ‘true’ and estimated orbit	80
5.11	Difference between ‘true’ and estimated gravity field coefficients in terms of selenoid height	81
5.12	Singular value decomposition	82
5.13	The L-curve and its curvature	83
5.14	Regularized vs. unregularized solution	84
5.15	Spectral leakage effect	84
5.16	LRO spacecraft and macro-model approximation	90
5.17	Interpolated spacecraft mass	92
5.18	Illustration of overlapping short, medium, and long arcs	94
5.19	Range-rate residuals for short arcs and medium arcs.	95
5.20	Estimated measurement biases for the ground stations tracking LRO via two-way Doppler range-rates	97
5.21	Range-rate residuals for the primary station and the Universal Space Network (USN) stations and the dependence on the Earth viewing geometry angle	98
5.22	RMS values of Doppler range-rate residuals	99
5.23	RMS values of orbit overlaps	99
5.24	Differences between the estimated LRO orbit and the science orbit	101
5.25	Pass per pass measurement biases for four stations tracking Lunar Reconnaissance Orbiter (LRO) via optical laser ranges.	103
5.26	LRO clock drift and aging rate estimated from all stations	104
5.27	Acceleration due to third bodies	104
5.28	Acceleration due to gravitational forces	105
5.29	Acceleration due to Schwarzschild field	105
5.30	Acceleration due to non-gravitational forces	106
5.31	Residual norm vs. solution norm for a Tikhonov-Phillips regularization	107
5.32	Degree-wise signal and errors of various regularized lunar gravity field solutions	108
5.33	Degree-wise signal and errors of the estimated lunar gravity field coefficients	109
5.34	Differences in selenoid height between the regularized gravity field solution and the a priori gravity field model	110
5.35	Differences in selenoid height between the regularized gravity field solution and the a priori gravity field model (nearside)	110
5.36	Selenoid uncertainties for the regularized gravity field solution	111

5.37 Selenoid uncertainties for the regularized gravity field solution (nearside)	111
B.1 Impact of different observation weighting on the monthly grav- ity field estimates	136
C.1 Dimensional layout of LRO (stowed)	142
C.2 Dimensional layout of LRO (deployed)	143
D.1 Observed range-rates and weather data	147

List of Tables

4.1	Characteristics of considered geodetic satellites	50
4.2	Number of NPs per satellite from Jan 2000 to Oct 2013	50
4.3	POD standards for geodetic satellites	53
4.4	Estimated arc and global parameters	55
4.5	RMS of post-fit range residuals and of orbit connecting points	58
5.1	LRO mission phases	66
5.2	Orbital characteristics during LRO’s polar mapping phase	67
5.3	Stations performing laser ranging measurements to LRO	72
5.4	Stations performing Doppler measurements to LRO	74
5.5	Settings for the simulation of tracking data	77
5.6	Number of simulated observations	78
5.7	POD standards for LRO (simulation)	79
5.8	RMS of the differences between ‘true’ and recovered orbit	80
5.9	List of gravitational parameters	87
5.10	POD standards for LRO	87
5.11	LRO macro-model	91
5.12	RMS of overlap differences and residuals (short arcs)	94
5.13	RMS of overlap differences and residuals (medium arcs)	95
5.14	RMS of overlap differences and residuals (long arcs)	96
5.15	Estimated arc and global parameters for orbits based on Doppler range-rates	97
5.16	RMS of orbit overlap differences and of orbit differences w.r.t. the science orbits	100
5.17	Estimated arc parameters for orbits based on laser ranges	102
A.1	Computation of the downlink light travel time for geodetic satellites	134
C.1	List of maneuvers	137

D.1 Example for extracted ASCII data from a binary range-rate observation file	146
---	-----

Nomenclature

A, A_i	satellite cross-sectional area, area of satellite plate i
a, a_j	albedo and albedo of planetary spot j , respectively
A	design matrix
$a_0, a_1, a_2, c_0, c_1, c_2$	albedo parameters of planetary radiation model introduced by Knocke et al. (1988)
a_c	semimajor axis of a central body's reference ellipsoid of revolution
A_e, B_e, C_e	empirical parameters (1-cpr coefficients A, B , and constant acceleration bias C); $e = 1, 2, 3$ for along track, cross track, and radial directions
a_{\odot}	semimajor axis of the central body's orbit around the Sun
c	velocity of light
C_D	atmospheric drag coefficient
C_{nm}^a, S_{nm}^a	spherical harmonic coefficients of the albedo map
C_{nm}, S_{nm}	normalized spherical harmonic coefficients
C_R	solar radiation pressure coefficient
D	Doppler cycle count
d	atmospheric density
dA_j	surface area of planetary spot j

$dPdH$	lapse rate
E	vector pointing from the tracking point to LRO's center of mass
e, e_j	emissivity and emissivity of planetary spot j , respectively
$e_0, e_1, e_2, k_0, k_1, k_2$	emissivity parameters of planetary radiation model introduced by Knocke et al. (1988)
F , $\hat{\mathbf{F}}$	vector pointing from the ground station to the tracking point and the unit vector, respectively
f_{bias}	bias frequency
f_r	received (Doppler shifted) frequency at ground station
f_t	transmitted frequency at ground station
G_0	solar flux at the distance of 1 AU
G_j^e	radiation flux component due to emissivity originating from planetary spot j
G_j	radiation flux originating from planetary spot j
G_j^a	radiation flux component due to albedo originating from planetary spot j
$GM_c, GM_\odot, GM_\oplus, GM_b$	gravitational parameter of central body, Sun, Earth, planetary body b, respectively
$G(\mathbf{X}_i, t_i)$	nonlinear observation-state relationship
h	station height
I	identity matrix
J	total number of planetary surface elements
JD	Julian date of interest
K	spacecraft transponder turnaround ratio
K	regularization matrix

\mathbf{L}	diagonal matrix containing the inverse of the degree variances known as Kaula's rule
l	number of observations
M	frequency-dependent factor
m	satellite mass
N	total number of macro-model plates
$\hat{\mathbf{n}}, \hat{\mathbf{n}}_i$	normal unit vector of satellite surface and plate i , respectively
n, m	spherical harmonic degree and order, respectively
\mathbf{P}	observation weight matrix
P_0	mean sea level pressure
P_1, P_2	Legendre polynomials of first and second degree, respectively
P_{nm}	4π -normalized associated Legendre functions of the first kind of degree n and order m
$\mathbf{r}, \dot{\mathbf{r}}, \ddot{\mathbf{r}}$	position, velocity, acceleration of the satellite, respectively
$\dot{\mathbf{r}}_{\text{atm}}$	satellite velocity relative to the atmosphere
\mathbf{r}_b	position of planetary body b
$\ddot{\mathbf{r}}_C$	acceleration due to the Coriolis force
$\mathbf{r}_c, \dot{\mathbf{r}}_c$	position and velocity of the central body
$\ddot{\mathbf{r}}_{\text{cb}}$	acceleration due to the central body's gravity field
$\ddot{\mathbf{r}}_d$	acceleration due to atmospheric drag
$\ddot{\mathbf{r}}_{\text{dr}}$	acceleration due to diffuse reflection
$\ddot{\mathbf{r}}_{\text{emp}}$	acceleration due to empirical forces
$\ddot{\mathbf{r}}_{\text{ep}}$	acceleration due to solid earth pole tide
$\ddot{\mathbf{r}}_{\text{et}}$	acceleration due to solid Earth tides

$\ddot{\mathbf{r}}_g$	acceleration due to gravitational forces
$\ddot{\mathbf{r}}_i$	acceleration due to specular reflection (incidence)
r_j	distance between spacecraft and planetary spot j
$\ddot{\mathbf{r}}_{LT}$	acceleration due to the Lense-Thirring precession
$\ddot{\mathbf{r}}_{mt}$	acceleration due to solid Moon tides
$\ddot{\mathbf{r}}_n$	acceleration due to third bodies
$\ddot{\mathbf{r}}_{ng}$	acceleration due to non-gravitational forces
$\ddot{\mathbf{r}}_o$	acceleration due to ocean tides
$\ddot{\mathbf{r}}_{ob}$	acceleration due to oblateness
$\ddot{\mathbf{r}}_{op}$	acceleration due to ocean pole tide
$\ddot{\mathbf{r}}_p$	acceleration due to planetary radiation
r, φ, λ	spherical coordinates
$\ddot{\mathbf{r}}_r$	acceleration due to specular reflection (reflection)
$\ddot{\mathbf{r}}_{rel}$	acceleration due to relativistic effects
$\ddot{\mathbf{r}}_S$	acceleration due to Schwarzschild field
$\ddot{\mathbf{r}}_s$	acceleration due to solar radiation pressure
$\ddot{\mathbf{r}}_{sr}$	acceleration due to specular reflection
\mathbf{r}_{stat}	position of the ground station
$\mathbf{r}_\odot, \dot{\mathbf{r}}_\odot$	position and velocity of the Sun
$\ddot{\mathbf{r}}_t$	acceleration due to tidal effects
$\ddot{\mathbf{r}}_{th}$	acceleration due to thermal radiation
$\hat{\mathbf{s}}$	unit vector pointing from the satellite to the Sun
$\hat{\mathbf{s}}_j$	unit vector pointing from planetary spot j to the satellite
T_c	Doppler count interval

t_p	epoch of the periodic terms
t_{refLRO}	reference time of LRO
t_{refstat}	reference time of ground station
u_1, u_2	LRO clock drift rate and clock aging rate, respectively
V	potential of a planetary body
\mathbf{X}	satellite state
$\mathbf{x}, \hat{\mathbf{x}}$	state deviation and estimated state deviation, respectively
\mathbf{X}^*	satellite's reference position
\mathbf{X}_0	true initial state
\mathbf{X}_0^*	satellite's nominal initial state
$\hat{\mathbf{x}}_\eta$	estimated state deviation using the regularization parameter η
\mathbf{X}_k	satellite state at arbitrary epoch t_k
\mathbf{x}_k	state deviation at arbitrary epoch t_k
\mathbf{y}	observation deviation
\mathbf{Y}^*	computed observations
\mathbf{Y}_i	observation of the state at epoch t_i
α, β	coefficient of absorption and reflection, respectively
β	constant parameters to be estimated
Δ_{atm}	displacement due to atmospheric pressure loading
ΔD	change in the Doppler cycle count
Δ_{ep}	displacement due to Earth pole tide loading
Δ_{et}	displacement due to the solid Earth tides
Δ_{o}	displacement due to the ocean tide loading

Δ_{op}	displacement due to ocean pole tide loading
$\Delta\rho_{\text{cl}}$	clock correction
$\Delta\rho_{\text{com}}$	center of mass correction
$\Delta\rho_{\text{rel}}$	general relativity correction
$\Delta\rho_{\text{trop}}$	tropospheric delay correction
$\tilde{\rho}_{\text{u}}, \tilde{\rho}_{\text{d}}$	corrected uplink and downlink range, respectively
Δ_{t}	total displacement due to tidal effects
$\Delta\tau_1, \Delta\tau_2$	observed one-way and two-way light travel time
ϵ_i	observation residual at epoch t_i
η	regularization parameter
γ_j	angle between the unit normal of planetary spot j and the direction to the satellite
κ	shadow function
κ_j	shadow function of planetary spot j
ν	true anomaly
Ω	angular velocity of the base vectors of the inertial geocentric reference system with respect to the barycentric reference system
ω	frequency of periodic Earth radiation coefficients
ω_{c}	rotation rate of the central body
Φ	state transition matrix
ρ	distance between ground station and satellite
$\dot{\rho}^{\text{o}}, \dot{\rho}^{\text{c}}$	observed and computed one-way range-rate, respectively
$\rho^{\text{o}}, \rho^{\text{c}}$	observed and computed one-way distance between station and satellite, respectively
$\rho_{\text{u}}, \rho_{\text{d}}$	uplink and downlink range, respectively

σ_n^2	degree variances
τ_u, τ_d	uplink and downlink light travel time, respectively
θ	angle between the satellite surface normal and the direction to the Sun
θ_i	angle between the satellite surface normal of plate i and the direction to the Sun
θ_{ij}	angle between normal vector of satellite plate i and planetary spot j
θ_j	angle between the satellite surface normal and planetary spot j
θ_j^\odot	angle between the unit normal of planetary spot j and the direction to the Sun
ζ, δ	specular and diffuse reflectivity, respectively
ζ_i, δ_i	specular and diffuse reflectivity of plate i , respectively

List of Abbreviations

1-cpr	1-cycle per revolution
ASCII	American Standard Code for Information Interchange
AU	Astronomical Unit
CDDIS	Crustal Dynamics Data Information System
CHAMP	Challenging Minisatellite Payload
CRD	Consolidated Laser Ranging Data Format
CSR	Center for Space Research
dH	delta-H
DLAM-1	Delft Lunar Albedo Model 1
d/o	degree and order
DTM	Drag Temperature Model
DSN	Deep Space Network
EDC	EUROLAS Data Center
EIGEN	European Improved Gravity model of the Earth by New techniques
EOP	Earth Orientation Parameter
FES	Finite Element Solution
FDf	Flight Dynamics Facility
Fortran	Formula Translating System

GNSS	Global Navigation Satellite System
GOCE	Gravity Field and Steady-State Ocean Circulation Explorer
GOCO	Gravity Observation Combination
GOT	Goddard Ocean Tide
GPS	Global Positioning System
GRACE	Gravity Recovery and Climate Experiment
GRAIL	Gravity Recovery and Interior Laboratory
GSFC	Goddard Space Flight Center
HGA	High Gain Antenna
HPF	High-level Processing Facility
IAU	International Astronomical Union
ICRF	International Celestial Reference Frame
IERS	International Earth Rotation and Reference Systems Service
ILRS	International Laser Ranging Service
IR	Infrared
JB	Jacchia-Bowman
JPL	Jet Propulsion Laboratory
JPL DE	Jet Propulsion Laboratory Development Ephemeris
LAGEOS	Laser Geodynamics Satellite
LOLA	Lunar Orbiter Laser Altimeter
LEO	Low Earth Orbiter
LP	Lunar Prospector
LPRP	Lunar Precursor Robotic Program
LRO	Lunar Reconnaissance Orbiter
LS	Least Squares

MF	Mapping Function
MRO	Mars Reconnaissance Orbiter
MSIS	Mass Spectrometer Incoherent Scatter Radar
NAIF	Navigation and Ancillary Information Facility
NASA	National Aeronautics and Space Administration
NGSLR	Next Generation Satellite Laser Ranging
NRL	Naval Research Laboratory
NP	Normal Point
PDS	Planetary Data System
PGR	Postglacial Rebound
POD	Precise Orbit Determination
RMS	Root Mean Square
SA	Solar Array
SELENE	Selenological and Engineering Explorer
SM	Science Mission Phase
SFF	Small Forces Files
SLR	Satellite Laser Ranging
SPICE	Spacecraft Planet Instrument C-matrix Events
SK	Station Keeping
SVD	Singular Value Decomposition
TAI	International Atomic Time
TDB	Dynamical Barycentric Time
TDT	Terrestrial Dynamical Time
TEC	Total Electron Content
TIRV	Tuned Inter-Range Vector

TOPEX	Topography Experiment
US	United States
USN	Universal Space Network
UTC	Coordinated Universal Time
UTDF	Universal Tracking Data Format
VLBI	Very Long Baseline Interferometry
VMF	Vienna Mapping Function

Chapter 1

Introduction

Background and rationale

Satellites in free fall around a planetary body give important clues on its gravity field. The Earth's gravity field is known in detail thanks to a large number of realized satellite missions. Among them are geodetic satellites as well as dedicated gravity field missions such as the Challenging Minisatellite Payload (CHAMP) project (Reigber, 2002), the Gravity Recovery and Climate Experiment (GRACE), see Tapley et al. (2004a), and the Gravity Field and Steady-State Ocean Circulation Explorer (GOCE), see Drinkwater et al. (2006). Different data types are complementary due to different measurement principles, accuracies, as well as spatial distribution and resolution. Consequently, combined satellite-only gravity field models benefit from the data types' individual strengths. While the Earth's dynamical flattening term, C_{20} , can be determined most precisely with Satellite Laser Ranging (SLR) measurements to geodetic satellites, long- to medium-wavelengths of the gravity field are mainly determined from GRACE data. GOCE contributes significantly to the short wavelengths. Examples¹ for combined satellite-only gravity field models include GO_CONS_GCF_2_DIR_R5 (Bruinsma et al., 2013), EIGEN-6S2 (Rudenko et al., 2014), and the Gravity Observation Combination (GOCO) model GOCO03S (Mayer-Gürr et al., 2012). The Earth's gravity field is not static but undergoes temporal variations due to mass redistributions in the oceans, of glaciers, ice sheets, inland water reservoirs, the atmosphere, etc. Consequently, knowledge about the temporal variations of gravity allows to infer dynamic processes on the Earth's surface. This is particularly relevant in the context of global climate change (IPCC, 2013).

¹a comprehensive overview is given at <http://icgem.gfz-potsdam.de/ICGEM/>

Using Earth-based satellite tracking data, only the long wavelengths of the central body's gravity field can be resolved. The resolution accomplished with SLR measurements to geodetic satellites, however, is significantly lower due to high orbital altitudes of up to several thousands of kilometers. Thus, only the very long wavelengths of the Earth's gravity field (up to degree and order (d/o) 4) are investigated in this thesis. Among the estimated coefficients, those of degree 2 are of special interest as they are related to the tensor of inertia (e.g. Heiskanen and Moritz, 1967).

Furthermore, this thesis deals with gravity field recovery of the Moon, again using ground-based tracking data. Lunar exploration from space started in 1966 with the launch of the lunar orbiter mission Luna-10. It was followed by further satellites of the Luna program, the Lunar Orbiters, the subsatellites of Apollo, and Clementine. Lunar Prospector (LP), launched in 1998, orbited the Moon at low altitudes (30 to 100 km) allowing the creation of a first detailed gravity field model (Konopliv et al., 2001). In general, lunar gravity field recovery is severely hampered by the 1:1 spin-orbit resonance of the Earth-Moon system since direct tracking over the Moon's farside is impossible. The Japanese Selenological and Engineering Explorer (SELENE), launched in 2007, provided the first global data set of the Moon by incorporating three satellites: a main orbiter in a circular orbit and two sub-satellites in elliptical orbits (Namiki et al., 1999). In addition to classical radiometric tracking data, 4-way Doppler tracking between a ground station, the main orbiter, and a subsatellite was employed as well as Very Long Baseline Interferometry (VLBI) between the sub-satellites and two ground stations (Goossens et al., 2011b; Kikuchi et al., 2009). In 2011, the Gravity Recovery and Interior Laboratory (GRAIL) mission was launched. By means of low-low satellite-to-satellite tracking between two spacecraft in the same orbit, an unprecedented resolution of the lunar gravity field could be achieved (Zuber et al., 2013).

The Lunar Reconnaissance Orbiter (LRO) was launched in 2009. Its main purpose is to prepare for future in-situ lunar exploration. LRO is pioneering in the sense that it is the first satellite in interplanetary space routinely tracked with optical laser ranges in addition to radiometric techniques (Zuber et al., 2010). These optical laser ranges are the reason why tracking data to LRO are investigated in this thesis since they provide a strong link to the geodetic satellites that are tracked with optical laser ranges as well. Again, gravity field information is inferred from orbit perturbations. Unlike the Earth's gravity field, the Moon's gravity field hardly shows any temporal variability as the Moon has neither oceans nor atmosphere. Thus, solely the

Moon's static gravity field is focused on in this work.

To enhance spatial coverage, tracking is typically performed by a station network. For this work, the International Laser Ranging Service (ILRS) network and the Universal Space Network (USN) are relevant as they track geodetic satellites and LRO, respectively. Despite of numerous tracking stations, the sampling of the gravity field remains incomplete. This is particularly true for the Moon due to the farside data gap. Notice that this thesis is confined to the recovery of global gravity field coefficients. One might argue that this is not the best choice as far as the Moon is concerned where almost one half lacks observations². Due to the integral behavior of the satellite orbit, however, some gravity field signals can also be captured at the farside (Floborghagen, 2002). Moreover, global gravity field models are a prerequisite for mission design; in particular, low orbiting satellites are severely perturbed by the gravity field.

Objectives

The objective of this thesis is to recover the very long wavelengths of the Earth's and the Moon's gravity field using Earth-based satellite tracking data. This intent is intrinsically related to the field of Precise Orbit Determination (POD). Finding the optimal parametrization of the satellite's motion for the purpose of gravity field recovery plays herein a crucial role. Unfortunately, parametrization is not the same for geodetic satellites and the LRO spacecraft: different satellite shapes (spherical vs. complex), measurement types (two-way laser ranges vs. one-way laser ranges/Doppler range-rates), spatial coverage (gaps over polar regions and oceans vs. farside gap), and different environments (perturbed by the atmosphere vs. unperturbed by the atmosphere) require different parametrization.

The orbital quality of geodetic satellites and LRO is assessed via observation residuals. Further, orbit connecting points were analyzed for geodetic satellites and extensive overlap analysis tests were conducted for LRO. Moreover, LRO orbits are externally validated with orbits published by the National Aeronautics and Space Administration (NASA).

Temporal variations of the Earth's static gravity field were examined as well. These variations are validated against externally computed time series. Apart from small tidal variations, the lunar gravity field has no temporal variability

²due to lunar librations 59% of the Moon's surface is visible from the Earth

which is why solely the static part is focused on.

Chapter 2

Precise orbit determination

The Precise Orbit Determination (POD) problem involves the determination of a satellite's state (position and velocity) by means of observations. Basically, there exist three approaches for orbit determination. First, the dynamic approach (e.g. Tapley et al., 2004b) where the satellite trajectory is a particular solution of the equation of motion of which force models are an integral part. The precision of dynamic orbits mainly depends on the dynamic models. Second, the kinematic or geometric approach (Svehla and Rothacher, 2005) that is not dependent on the dynamical description of the satellite and the equations of motion (although force models do play a role for the state determination of Global Navigation Satellite System (GNSS) satellites). The ephemeris are provided at discrete measurement epochs. The third approach is the reduced dynamic approach, which is mainly used for GNSS. The dynamic model parameters are held fixed once convergence is achieved. Additional accelerations are estimated using the observation geometry alone. Concerning POD based on Satellite Laser Ranging (SLR) measurements or Doppler range-rates, the dynamic approach is used. Dynamic orbit determination is also implemented within GEODYN II (McCarthy et al., 1993), a software package provided by the Goddard Space Flight Center (GSFC). All results presented in this thesis are based on this software.

The solution of the POD problem requires the solution of the equation of motion of a satellite, which can be expressed as a system of first-order differential equations (note that the representation of the POD problem has been adopted from Tapley, 1973; Tapley et al., 2004b):

$$\frac{d}{dt}\mathbf{X}(t) = \dot{\mathbf{X}}(t) = F(\mathbf{X}, t), \quad \mathbf{X}(t_k) \equiv \mathbf{X}_k \quad (2.1)$$

where \mathbf{X} is the unknown satellite state vector and t_k denotes an arbitrary epoch. \mathbf{X} contains the position (X, Y, Z) , the velocity $(\dot{X}, \dot{Y}, \dot{Z})$, and a vector $\boldsymbol{\beta}$ composed of constant parameters that shall be solved for (e.g. solar radiation pressure coefficient and gravity field coefficients):

$$\mathbf{X} = \begin{pmatrix} X \\ Y \\ Z \\ \dot{X} \\ \dot{Y} \\ \dot{Z} \\ \boldsymbol{\beta} \end{pmatrix} = \begin{pmatrix} \mathbf{r} \\ \dot{\mathbf{r}} \\ \boldsymbol{\beta} \end{pmatrix} \quad (2.2)$$

$$\dot{\mathbf{X}} = \begin{pmatrix} \dot{\mathbf{r}} \\ \ddot{\mathbf{r}} \\ 0 \end{pmatrix} = \begin{pmatrix} \dot{\mathbf{r}}(t) \\ \ddot{\mathbf{r}}(t, \mathbf{r}, \dot{\mathbf{r}}, \boldsymbol{\beta}) \\ 0 \end{pmatrix}$$

The satellite is observed from Earth-based ground stations. These observations are related to the state in a nonlinear manner. The observation-state relationship can be expressed as

$$\mathbf{Y}_i = G(\mathbf{X}_i, t_i) + \boldsymbol{\epsilon}_i, \quad i = 1, \dots, l \quad (2.3)$$

where \mathbf{Y}_i is a p -dimensional observation vector of the state at epoch t_i ¹, $G(\mathbf{X}_i, t_i)$ is the nonlinear function relating the observation with the state, $\boldsymbol{\epsilon}_i$ is the observation residual at epoch t_i , and l is the number of observations. The inability to observe the state directly, the nonlinear relation between the observation and the state, the fact that the number of observations per epoch is generally smaller than the number of unknowns, and the errors in the observations make the estimation of the satellite's state a complex nonlinear estimation problem (Tapley et al., 2004b).

If the satellite's reference initial state, \mathbf{X}_0^* , is known, a reference trajectory, \mathbf{X}^* , can be computed by integrating Equation (2.1). The trajectory of the actual motion can then be expanded in a Taylor's series about the reference trajectory. Only if the true trajectory, \mathbf{X} , and the reference trajectory remain close, the linearization procedure is successful and convergence is met.

¹ $p > 1$ if more than one quantity is observed at a single epoch (e.g. if Doppler range-rate and radiometric range are observed at a single epoch, $p = 2$ hold true)

The linear relationship for the observation deviation is expressed in a similar manner as a function of the observation, \mathbf{Y} , and of the computed observation, \mathbf{Y}^* . For the linearization procedure, the state deviation, \mathbf{x} , and the observation deviation, \mathbf{y} , are defined as

$$\mathbf{x}(t) = \mathbf{X}(t) - \mathbf{X}^*(t), \quad \mathbf{y}(t) = \mathbf{Y}(t) - \mathbf{Y}^*(t). \quad (2.4)$$

From the first term of Equation (2.4) follows

$$\dot{\mathbf{x}}(t) = \dot{\mathbf{X}}(t) - \dot{\mathbf{X}}^*(t). \quad (2.5)$$

Both the state and the observations have to be linearized, yielding

$$\begin{aligned} \dot{\mathbf{X}}(t) &= F(\mathbf{X}, t) = \overbrace{F(\mathbf{X}^*, t)}^{\dot{\mathbf{X}}^*(t)} + \overbrace{\left[\frac{\partial F(t)}{\partial \mathbf{X}(t)} \right]^*}_{\mathbf{B}(t)} [\mathbf{X}(t) - \mathbf{X}^*(t)] \\ &\quad + O_F[\mathbf{X}(t) - \mathbf{X}^*(t)] \\ \mathbf{Y}_i &= G(\mathbf{X}_i, t_i) + \epsilon_i = \underbrace{G(\mathbf{X}_i^*, t_i)}_{\mathbf{Y}^*} + \underbrace{\left[\frac{\partial G}{\partial \mathbf{X}} \right]_i^*}_{\tilde{\mathbf{H}}_i} [\mathbf{X}_i - \mathbf{X}_i^*] \\ &\quad + O_G[\mathbf{X}_i - \mathbf{X}_i^*] + \epsilon_i \end{aligned} \quad (2.6)$$

If the Taylor expansions [cf. Equation (2.6)] are truncated after the linear terms (O_F , O_G indicate terms higher than the first order), state deviation and observation deviation can be described by a set of linear differential equations:

$$\begin{aligned} \dot{\mathbf{x}}(t) &= \dot{\mathbf{X}}(t) - \dot{\mathbf{X}}^*(t) = \mathbf{B}(t) \mathbf{x}(t), \\ \mathbf{y}_i &= \mathbf{Y}_i - \mathbf{Y}_i^* = \tilde{\mathbf{H}}_i \mathbf{x}_i + \epsilon_i \end{aligned} \quad (2.7)$$

The general solution for the first system in Equation (2.7) can be expressed as

$$\mathbf{x}(t) = \Phi(t, t_k) \mathbf{x}_k, \quad \Phi(t, t_k) = \frac{\partial \mathbf{X}(t)}{\partial \mathbf{X}_k} \quad (2.8)$$

where \mathbf{x}_k is the value of \mathbf{x} at arbitrary time t_k , and $\Phi(t, t_k)$ is referred to as the state transition matrix. The state transition matrix maps deviations in the state vector from one time to another. The differential equation for the state transition matrix is obtained by differentiating Equation (2.8) yielding

$$\dot{\mathbf{x}}(t) = \dot{\Phi}(t, t_k) \mathbf{x}_k. \quad (2.9)$$

Inserting $\dot{\Phi}(t, t_k) \mathbf{x}_k$ for the left hand side of Equation (2.9) and $\mathbf{B}(t) \Phi(t, t_k) \mathbf{x}_k$ for the right hand side, gives the differential equation of the state transition matrix

$$\dot{\Phi}(t, t_k) = \mathbf{B}(t) \Phi(t, t_k). \quad (2.10)$$

With the initial conditions \mathbf{x}_0 and the special case that $t_k = t_0$, the state transition matrix reduces to the identity matrix $\Phi(t_0, t_0) = \mathbf{I}$, and the solution becomes unique. The entries of the state transition matrix are as follows:

$$\Phi(t, t_0) = \frac{\partial \mathbf{X}(t)}{\partial \mathbf{X}_0} = \begin{pmatrix} \frac{\partial \mathbf{r}(t)}{\partial \mathbf{X}_0} \\ \frac{\partial \dot{\mathbf{r}}(t)}{\partial \mathbf{X}_0} \\ \frac{\partial \beta(t)}{\partial \mathbf{X}_0} \end{pmatrix} \quad (2.11)$$

Differentiating Equation (2.11) gives the second-order differential equation

$$\dot{\Phi}(t, t_0) = \frac{\partial \dot{\mathbf{X}}(t)}{\partial \mathbf{X}_0} = \begin{pmatrix} \frac{\partial \dot{\mathbf{r}}(t)}{\partial \mathbf{X}_0} \\ \frac{\partial \ddot{\mathbf{r}}(t)}{\partial \mathbf{X}_0} \\ 0 \end{pmatrix} = \underbrace{\begin{pmatrix} \frac{\partial \dot{\mathbf{r}}(t)}{\partial \mathbf{X}(t)} \\ \frac{\partial \ddot{\mathbf{r}}(t)}{\partial \mathbf{X}(t)} \\ 0 \end{pmatrix}}_{\frac{\partial \dot{\mathbf{X}}(t)}{\partial \mathbf{X}(t)}} \underbrace{\begin{bmatrix} \frac{\partial \mathbf{X}(t)}{\partial \mathbf{X}_0} \end{bmatrix}}_{\Phi(t, t_0)}, \quad (2.12)$$

with

$$\frac{\partial \dot{\mathbf{X}}(t)}{\partial \mathbf{X}(t)} = \begin{pmatrix} \frac{\partial \dot{\mathbf{r}}}{\partial \mathbf{r}} & \frac{\partial \dot{\mathbf{r}}}{\partial \dot{\mathbf{r}}} & \frac{\partial \dot{\mathbf{r}}}{\partial \beta} \\ \frac{\partial \ddot{\mathbf{r}}}{\partial \mathbf{r}} & \frac{\partial \ddot{\mathbf{r}}}{\partial \dot{\mathbf{r}}} & \frac{\partial \ddot{\mathbf{r}}}{\partial \beta} \\ 0 & 0 & 0 \end{pmatrix}. \quad (2.13)$$

Note that the estimation of force model parameters (in particular gravity field coefficients) is an integral part of this thesis. If no parameters were

estimated, i.e. if only POD were of interest, Equation (2.13) would reduce to the first two lines and the first two columns since then $\ddot{\mathbf{r}}$ would not depend on $\boldsymbol{\beta}$. How the differential equation of the observation deviation is solved is shown in Section 2.3.

Summing up, the solution of the orbit determination problem requires

1. the equation of motion describing the forces acting on the satellite (cf. Section 2.1),
2. the observation model describing the relation of the observations to the satellite state (cf. Section 2.2), and
3. a least squares estimation algorithm used to obtain the estimate (cf. Section 2.3).

2.1 Force models

The overall acceleration of the satellite, $\ddot{\mathbf{r}}$, can be subdivided into the acceleration due to gravitational forces, $\ddot{\mathbf{r}}_g$, and the acceleration due to non-gravitational forces, $\ddot{\mathbf{r}}_{ng}$. Since the modeling of those two forces is not perfect, empirical accelerations, $\ddot{\mathbf{r}}_{emp}$, are introduced, yielding

$$\ddot{\mathbf{r}} = \ddot{\mathbf{r}}_g + \ddot{\mathbf{r}}_{ng} + \ddot{\mathbf{r}}_{emp}. \quad (2.14)$$

Within the following sections, the non-gravitational forces are described in more detail than the gravitational forces. Information about the latter can be easily retrieved from the International Earth Rotation and Reference Systems Service (IERS) conventions (Petit and Luzum, 2010).

2.1.1 Acceleration due to gravitational forces

The primary gravitational force an orbiter is exposed to is the gravity field of the central body (central body acceleration $\ddot{\mathbf{r}}_{cb}$). To a minor extent, third bodies (n-body point-mass acceleration $\ddot{\mathbf{r}}_n$), the indirect oblateness of Earth and Moon ($\ddot{\mathbf{r}}_{ob}$), relativistic effects ($\ddot{\mathbf{r}}_{rel}$), and tidal effects ($\ddot{\mathbf{r}}_t$) affect the motion of a satellite. Summing these accelerations gives the overall gravitational acceleration, $\ddot{\mathbf{r}}_g$:

$$\ddot{\mathbf{r}}_g = \ddot{\mathbf{r}}_{cb} + \ddot{\mathbf{r}}_t + \ddot{\mathbf{r}}_n + \ddot{\mathbf{r}}_{ob} + \ddot{\mathbf{r}}_{rel}. \quad (2.15)$$

In the sequel, the gravitational forces acting on Earth- and Moon-orbiting satellites are discussed in more detail.

Acceleration due to the central body's gravitational field

The potential of a planetary body, V , in terms of spherical harmonics satisfying the Laplace equation (Kaula, 1966; Heiskanen and Moritz, 1967) can be expressed as

$$V(r, \varphi, \lambda) = \frac{GM_c}{r} \left\{ C_{00} + \sum_{n=1}^{\infty} \sum_{m=0}^n \left(\frac{a_c}{r} \right)^n P_{nm}(\sin \varphi) \times \right. \\ \left. [C_{nm} \cos(m\lambda) + S_{nm} \sin(m\lambda)] \right\}. \quad (2.16)$$

The spherical coordinates r, φ, λ denote the distance from the body-fixed planetocenter, latitude, and longitude, respectively; they refer to a point outside the attracting masses. GM_c is the central body's gravitational parameter, a_c is the semimajor axis of a central body's reference ellipsoid of revolution, and P_{nm} indicate the 4π -normalized associated Legendre functions of the first kind of degree n and order m . Whereas the first term in Equation (2.16) represents the potential of a point mass (or a homogeneous sphere), C_{nm} and S_{nm} are normalized spherical harmonic coefficients describing the deviations of the actual potential from the potential of a homogeneous sphere. Zonal coefficients ($m = 0$) describe masses symmetrical to the equator, tesseral coefficients ($n = m$) describe masses symmetrical to the rotation axis, and sectorial coefficients ($n \neq m$) reflect a chessboard-like mass distribution (see Figure 2.1). In practice, the series in Equation (2.16) is truncated at a maximum degree n_{\max} depending on data sensitivity. The coefficient C_{00} in Equation (2.16) is 1. Further, if the origin of the coordinate system coincides with the center of mass, all terms of degree 1 in the spherical harmonic expansion of the gravity field vanish ($C_{10} = C_{11} = S_{11} = 0$).

The coefficients of degree 2 are of particular interest because they are related to the planet's tensor of inertia (e.g. Heiskanen and Moritz, 1967). Their geometrical meaning is as follows: C_{20} represents the dynamical polar flattening and is for both the Earth and the Moon the largest coefficient describing the deviation of the potential from a homogeneous sphere. Note that in case of the Earth the C_{20} term is two orders of magnitude larger than all other

coefficients. For the Moon, in contrast, C_{20} is only twice as large as C_{22} . The accurate estimation of C_{20} is therefore of crucial importance. The degree 2 order 1 coefficients (C_{21} and S_{21}) are coupled with the polar motion; they would be zero if the rotation axis would coincide with the third principal axis of inertia (*ibid.*). Finally, C_{22} and S_{22} reflect the ellipticity of the equator.

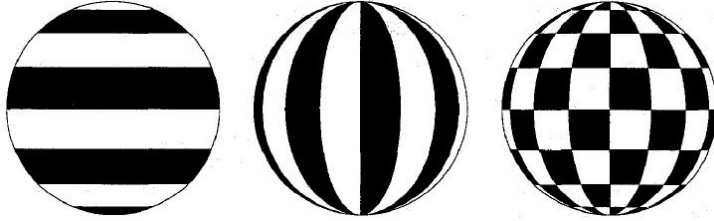


Figure 2.1: Zonal, tesseral, and sectorial spherical harmonic coefficients (from Floberghagen et al. (1996)).

Applying the Nabla operator to the gravitational potential gives the acceleration due to the central body's gravity field

$$\ddot{\mathbf{r}}_{\text{cb}}(r, \varphi, \lambda) = \nabla V(r, \varphi, \lambda). \quad (2.17)$$

Note that for the integration of the equation of motion, Equation (2.17) has to be transferred (1) from spherical to Cartesian coordinates (Kaula, 1966), and (2) to the inertial system.

The Earth's gravity field is not fully described by the static part; temporal variations have to be considered as well. Significant variations arise due to dynamics in the atmosphere (e.g. Chao and Au, 1991; Peters et al., 2002), oceans (e.g. Johnson et al., 2001), cryosphere (e.g. Yoder et al., 1983; Baur and Sneeuw, 2011; Nerem and Wahr, 2011), hydrology (e.g. Chao and O'Connor, 1988; Chen et al., 2005), and due to plate motion (e.g. Biancale et al., 1991). Unlike the Earth, the Moon has no plate motion. Moonquakes exist but they are of much smaller amplitude than earthquakes (Williams and Dickey, 2002). Further, the rotation of the Moon is considerably slower compared to Earth (27.3 days vs. 23 hours and 56 minutes or one sidereal day). Since the Moon lacks atmosphere and oceans the rotation is also more quiet (*ibid.*). For the Gravity Recovery and Interior Laboratory (GRAIL) mission, a time-varying component in the lunar gravity field is taken into account – the motion of an oblate inner core relative to the mantle that introduces a monthly signature in C_{21} and S_{21} (Park et al., 2012; Asmar et

al., 2013). However, since simulations to GRAIL have shown that the core-signature can only be estimated with a relatively tight error margin (Park et al., 2012), this time-varying effect is thought to be uncritical in case of Lunar Reconnaissance Orbiter (LRO) and remains unconsidered for this reason.

Acceleration due to tides

The Earth is not a rigid body, thus responding to the attraction of Moon and Sun (solid Earth tides $\ddot{\mathbf{r}}_{\text{et}}$). Moon and Sun are also responsible for the presence of ocean tides, $\ddot{\mathbf{r}}_{\text{o}}$. The centrifugal effect of polar motion on solid Earth and oceans causes rotational deformation generating the solid Earth pole tide $\ddot{\mathbf{r}}_{\text{ep}}$ and the ocean pole tide $\ddot{\mathbf{r}}_{\text{op}}$ (Petit and Luzum, 2010). Hence, if we consider the Earth to be the central body, the acceleration due to tidal effects, $\ddot{\mathbf{r}}_{\text{t}}$, is composed by:

$$\ddot{\mathbf{r}}_{\text{t}} = \ddot{\mathbf{r}}_{\text{et}} + \ddot{\mathbf{r}}_{\text{o}} + \ddot{\mathbf{r}}_{\text{ep}} + \ddot{\mathbf{r}}_{\text{op}}. \quad (2.18)$$

The Moon responds to the attraction of Earth and Sun by deformation (solid Moon tides, e.g. Lemoine et al. 2013). Thus, for a lunar orbiter such as the LRO, only the acceleration due to solid Moon tides, $\ddot{\mathbf{r}}_{\text{mt}}$, has to be considered:

$$\ddot{\mathbf{r}}_{\text{t}} = \ddot{\mathbf{r}}_{\text{mt}}. \quad (2.19)$$

The analog of the pole tide is less than 1 mm in amplitude (Williams and Dickey, 2002) and remains therefore unconsidered.

Acceleration due to third bodies

The gravitational potential of third bodies (or n-bodies) is modeled as point-masses. In a planetocentric coordinate system, the acceleration due to n-bodies, $\ddot{\mathbf{r}}_{\text{n}}$, can be expressed as

$$\ddot{\mathbf{r}}_{\text{n}} = \sum_{i=1}^{b_{\text{max}}} GM_{b_i} \left(\frac{\mathbf{r}_{b_i} - \mathbf{r}}{\|\mathbf{r}_{b_i} - \mathbf{r}\|^3} - \frac{\mathbf{r}_{b_i}}{\|\mathbf{r}_{b_i}\|^3} \right) \quad (2.20)$$

Here, b denotes the third body modeled as point mass, GM_{b_i} is the i -th body's gravitational parameter, \mathbf{r}_{b_i} is the position of the i -th body, and \mathbf{r} is the position of the satellite both expressed in planetocentric coordinates. The

positions of the perturbing masses are obtained using planetary ephemeris. Since Equation (2.20) describes the satellite motion with respect to the central body's center of mass, which is a non-inertial point, the second term within parentheses accounts for the acceleration of the planetocenter (e.g. Tapley et al., 2004b, p. 63).

Acceleration due to oblateness

The acceleration of a spacecraft relative to the center of integration due to the oblateness of the bodies of the solar system consists of the direct acceleration of the spacecraft due to the oblateness of a body minus the indirect acceleration of the center of integration (Moyer, 1971; Moyer, 2000). Note that the indirect acceleration of the spacecraft relative to the center of integration is the negative of the acceleration of the center of integration due to oblateness. The direct acceleration is obtained from Equation 2.16 after transforming the acceleration to inertial rectangular coordinates. The indirect acceleration is computed only when the center of integration is the Earth or the Moon. According to Moyer (1971) and Moyer (2000), the force of attraction between Earth and Moon has four components:

1. attraction between point-mass Earth and point-mass Moon,
2. attraction between the oblate part of the Earth and point-mass Moon,
3. attraction between the oblate part of the Moon and point-mass Earth, and
4. attraction between the oblate part of the Earth and the oblate part of the Moon.

Attraction 1 is accounted for in the formulation of the acceleration due to third bodies and attraction 4 can be neglected due to its small effect (Moyer, 2000).

Due to the small lunar oblateness, GEODYN does not consider the direct acceleration of geodetic satellites due to the oblateness of the Moon nor the indirect acceleration of the Earth to the oblateness of the Moon. Hence, the acceleration of geodetic satellites relative to the center of integration due to the oblateness of third bodies reduces to the acceleration of the Earth due to the attraction between the oblate part of the Earth and point-mass Moon.

For lunar orbiters such as LRO, the software considers all components given in Moyer (1971): the direct acceleration of LRO due to the oblate part of

the Earth and the indirect acceleration that is composed of the acceleration of the Moon due to the oblateness of the Earth and the acceleration of the Moon due to the oblateness of the Moon.

Acceleration due to general relativity

General relativity has to be considered threefold throughout the POD process. First, the reference systems have to be corrected due to the involvement of various time systems (Ries et al., 1988; Huang et al., 1990). In case the geocentric reference system is used, Terrestrial Dynamical Time (TDT) enters the equation of motion; for a solar-system barycentric reference system, Dynamical Barycentric Time (TDB) is used (Tapley et al., 2004b). Since the time system of measurements is typically Coordinated Universal Time (UTC), which is derived from International Atomic Time (TAI), it has to be related to TDT or TDB. The difference between TAI and TDT is constant (32.184 s). The transformation between TDB and TDT is a purely periodic function depending on the position and velocity of Earth, Moon, planets, and Sun – a relativistic effect (e.g. Ries et al., 1988; Tapley et al., 2004b). Second, the measurement model has to be corrected due to relativistic effects (discussed in Section 2.2.5). Lastly, the equation of motion has to be corrected due to general relativity (discussed in the subsequent paragraphs).

The correction term due to general relativity within the equation of motion is composed by the Schwarzschild field, $\ddot{\mathbf{r}}_S$, the Coriolis force (also called geodesic precession), $\ddot{\mathbf{r}}_C$, and the Lense-Thirring precession, $\ddot{\mathbf{r}}_{LT}$, yielding

$$\ddot{\mathbf{r}}_{\text{rel}} = \ddot{\mathbf{r}}_S + \ddot{\mathbf{r}}_C + \ddot{\mathbf{r}}_{LT}. \quad (2.21)$$

From the three relativistic effects in Equation (2.21), the Schwarzschild field has the largest impact on the motion of both Earth orbiting and Moon orbiting satellites (Iorio, 2001, 2002). This effect, which leads to the precession of the pericenter, poses an acceleration of

$$\ddot{\mathbf{r}}_S = \frac{GM_c}{c^2 \|\mathbf{r}\|^3} \left[\left(4 \frac{GM_c}{\|\mathbf{r}\|} - \|\dot{\mathbf{r}}\|^2 \right) \mathbf{r} + 4 (\dot{\mathbf{r}} \cdot \mathbf{r}) \dot{\mathbf{r}} \right] \quad (2.22)$$

on the satellite, where GM_c is the gravitational parameter of the central body, c is the velocity of light, and \mathbf{r} and $\dot{\mathbf{r}}$ are satellite position and velocity

in the true of date coordinate system. $\|\mathbf{r}\|$ and $\|\dot{\mathbf{r}}\|$ denote the Euclidean lengths of \mathbf{r} and $\dot{\mathbf{r}}$, respectively. Since the satellite state refers to the center of integration, $\|\mathbf{r}\|$ is equivalent to the distance of the satellite from the center of integration.

The relativistic Coriolis force stems from the motion of the central body through the Sun's gravitational field causing a precession of the pole of a satellite orbit (Moyer, 2000). The acceleration due to this effect amounts to

$$\ddot{\mathbf{r}}_C = 2(\boldsymbol{\Omega} \times \dot{\mathbf{r}}), \quad (2.23)$$

where $\boldsymbol{\Omega}$ denotes the angular velocity of the base vectors of the inertial geocentric reference system with respect to the barycentric reference system. For the computation of $\boldsymbol{\Omega}$ the generally valid assumption is made that the Sun is the only significant contributor to the relativistic Coriolis force (Huang et al., 1990), yielding

$$\boldsymbol{\Omega} \approx \frac{3}{2}(\dot{\mathbf{r}}_c - \dot{\mathbf{r}}_\odot) \times \left[\frac{-GM_\odot(\mathbf{r}_c - \mathbf{r}_\odot)}{c^2\|\mathbf{r}_c - \mathbf{r}_\odot\|^3} \right]. \quad (2.24)$$

Here, \mathbf{r}_c , $\dot{\mathbf{r}}_c$ and \mathbf{r}_\odot , $\dot{\mathbf{r}}_\odot$ denote position and velocity of the central body and the Sun, respectively, and GM_\odot is the gravitational parameter of the Sun.

The Lense-Thirring effect (Lense and Thirring, 1918; Mashhoon et al., 1984; Pfister, 2007) originates from the rotation of a solid sphere and causes (to a minor extent compared to the Schwarzschild field, though) a precession in the longitude of the ascending node and a change in the mean motion of a satellite (Combrinck, 2013). This effect is also known as frame dragging: rotating bodies like the Earth (or the Moon) drag spacetime around themselves affecting the orbit of a satellite (Ciufolini and Pavlis, 2004). This precession is always in the direction of the rotation of the central body. The acceleration induced by the relativistic Lense-Thirring effect is

$$\ddot{\mathbf{r}}_{LT} = \begin{pmatrix} \frac{GM_c \omega_c a_c^2}{\|\mathbf{r}\|^2 \|\mathbf{r}\|} \left[\frac{4}{5} \frac{X^2+Y^2-2Z^2}{\|\mathbf{r}\|^2} \dot{Y} + \frac{12}{5} \frac{YZ}{\|\mathbf{r}\|^2} \dot{Z} \right] \\ -\frac{GM_c \omega_c a_c^2}{\|\mathbf{r}\|^2 \|\mathbf{r}\|} \left[\frac{4}{5} \frac{X^2+Y^2-2Z^2}{\|\mathbf{r}\|^2} \dot{X} - \frac{12}{5} \frac{XZ}{\|\mathbf{r}\|^2} \dot{Z} \right] \\ \frac{GM_c \omega_c a_c^2}{\|\mathbf{r}\|^2 \|\mathbf{r}\|} \frac{12}{5} \frac{Z}{\|\mathbf{r}\|} \frac{X\dot{Y}-Y\dot{X}}{\|\mathbf{r}\|} \end{pmatrix}, \quad (2.25)$$

where ω_c and a_c are the rotation rate and the semimajor axis of the central body, respectively, and $X, Y, Z, \dot{X}, \dot{Y}, \dot{Z}$ is the satellite state in true of date coordinates. Equation (2.25) shows that the acceleration due to the Lense-Thirring effect is proportional to the central body's rotation rate implying that this effect is considerably smaller for the slowly rotating Moon than it is for the Earth.

2.1.2 Acceleration due to non-gravitational forces

A satellite orbiting the Earth experiences two types of non-gravitational forces. First, the atmosphere can lead to significant changes in the satellite orbit's semimajor axis and eccentricity for Low Earth Orbiters (LEOs). As such, atmospheric drag is primarily responsible for the limited lifetime of a LEO. Second, space is pervaded by electromagnetic radiation coming from different sources such as the Sun (solar radiation pressure), the planet (planetary radiation pressure), or the spacecraft itself (spacecraft thermal radiation). The magnitude of all non-gravitational forces depends on the satellite's area-to-mass ratio. Keeping the ratio small reduces the effect of non-gravitational forces. To sum up, the overall non-gravitational acceleration acting on a satellite, $\ddot{\mathbf{r}}_{\text{ng}}$, is composed of the accelerations due to atmospheric drag, $\ddot{\mathbf{r}}_{\text{d}}$, solar radiation pressure, $\ddot{\mathbf{r}}_{\text{s}}$, planetary radiation, $\ddot{\mathbf{r}}_{\text{p}}$, and spacecraft thermal radiation, $\ddot{\mathbf{r}}_{\text{th}}$:

$$\ddot{\mathbf{r}}_{\text{ng}} = \ddot{\mathbf{r}}_{\text{d}} + \ddot{\mathbf{r}}_{\text{s}} + \ddot{\mathbf{r}}_{\text{p}} + \ddot{\mathbf{r}}_{\text{th}}. \quad (2.26)$$

Today, the major part of launched spacecraft are of complex shape due to reasons of energy supply and communication. Thus, the main spacecraft bus is often connected with steerable solar arrays and microwave antennas. These structures can produce relatively large non-gravitational perturbations which have to be modeled, as the accuracy of the modeled or computed observations of the satellite orbit should theoretically be at the same level as the observation accuracy. Milani et al. (1987) put the resulting difficulties in a nutshell:

“... when it comes to an accurate orbit computation, all these appendages [power system (e.g. Solar Array (SA)) and steerable antennas] are a real nightmare both because of radiation pressure and because of drag ...”

A complex shaped satellite is approximated by a combination of flat plates (also referred to as panels). Topography Experiment (TOPEX)/

Poseidon is a prominent example where non-gravitational forces were modeled by means of a box-wing model instead of a cannonball model due to the rigorous orbital accuracy requirement of 13 cm in the radial component (Marshall et al., 1992; Tapley et al., 1994). A box-wing model consists of a number of flat plates arranged like a box resembling the spacecraft bus and connected parts such as a SA and a High Gain Antenna (HGA). Knowledge of various plate characteristics and the orientation of each plate in space enables the computation of the non-gravitational forces acting on each plate independently. Summing up the individual accelerations gives the total force acting on the spacecraft.

Acceleration due to atmospheric drag

The acceleration due to atmospheric drag, $\ddot{\mathbf{r}}_d$, can be approximated by

$$\ddot{\mathbf{r}}_d = -\frac{1}{2}C_D \frac{A}{m} d(\mathbf{r}, t) \|\dot{\mathbf{r}}_{\text{atm}}\| \dot{\mathbf{r}}_{\text{atm}}, \quad (2.27)$$

where C_D is the dimensionless drag coefficient, A is the satellite cross-sectional area, m is the satellite mass, $d(\mathbf{r}, t)$ is the atmospheric density at the location of the satellite, and $\dot{\mathbf{r}}_{\text{atm}}$ is the velocity of the satellite relative to the atmosphere. The lift coefficient, which is typically one order of magnitude smaller than the drag coefficient, is neglected in Equation (2.27). Among all quantities of the above equation, the atmospheric density is the least well-known factor (Ries et al., 1993) and on top of that highly unpredictable. It depends on a myriad of factors, such as atmospheric constituents, temperature, current and mean solar flux, the declination of the Sun, and the geomagnetic activity. The dependencies, however, are not well understood (Yunck, 1993). State of the art atmospheric density models used to obtain $d(\mathbf{r}, t)$ include the Naval Research Laboratory (NRL) Mass Spectrometer Incoherent Scatter Radar (MSIS) model NRLMSISE-00 (Picone et al., 2002), the Jacchia-Bowman (JB) model JB2008 (Bowman et al., 2008), and the Drag Temperature Model (DTM) model DTM-2009 (Bruinsma et al., 2012). Depending on the inclination of the satellite surface with respect to the oncoming flow, C_D is typically somewhere in between 2 and 4 (Vallado and Finkleman, 2008). Estimating C_D is an effective way to eliminate (or at least mitigate) the average density model error over the estimation interval resulting in reduced orbit errors in the along track direction (Ries et al., 1993).

The lunar orbit, and with it any spacecraft orbiting the Moon, is too far away

from the Earth to be affected from its atmosphere (Williams and Dickey, 2002). As opposed to the Earth the Moon lacks atmosphere. Consequently, Equation (2.26) reduces to the last three components for LRO.

Acceleration due to solar radiation pressure

Solar radiation exchanges momentum with the satellite. The magnitude of this force depends, again, on the area-to-mass ratio, and on the reflection characteristics of the satellite material. The latter are defined by the coefficient of absorption, α , and the coefficient of reflection, β , of the surface material. The sum of α and β is equal to 1, accounting for the totality of light incident on the surface (Cook, 2001).

In case of geodetic satellites, the expression of effective solar radiation simplifies due to the prevailing constant cross-sectional area and due to the assumption of specular reflectivity, i.e. incident light reflects in only one direction. Diffuse reflection, i.e. reflection of incident light in many directions, is left unconsidered. In this simplified case, the acceleration due to specularly reflected light consists of a component due to incidence, $\ddot{\mathbf{r}}_i$, and a component due to reflection, $\ddot{\mathbf{r}}_r$. Summing these two the total perturbing acceleration due to solar radiation pressure, $\ddot{\mathbf{r}}_s$, reads

$$\ddot{\mathbf{r}}_s = \ddot{\mathbf{r}}_i + \ddot{\mathbf{r}}_r = -(1 + \beta) \frac{G_0}{c} \frac{A}{m} \left(\frac{a_\odot}{r_\odot} \right)^2 \hat{\mathbf{n}}, \quad (2.28)$$

where G_0 is the solar flux at the distance of 1 Astronomical Unit (AU), c is the speed of light, A is the satellite surface area, and m is the satellite mass. The satellite surface normal unit vector, $\hat{\mathbf{n}}$, gives the orientation of surface A . In case of spherical satellites it is assumed that $\hat{\mathbf{n}}$ points in the direction of the Sun, $\hat{\mathbf{s}}$ (Montenbruck and Gill, 2001). The solar irradiance at 1 AU decreases with the square of the distance between satellite and Sun (Cook, 2001). Therefore, a scaling factor depending on the semimajor axis of the central body's orbit around the Sun, a_\odot (i.e. 1 AU), and on the satellite orbital radius from the Sun, r_\odot , is part of Equation (2.28). The term $(1 + \beta)$ in Equation (2.28) is often replaced by the solar radiation pressure coefficient, C_R (Montenbruck and Gill, 2001), leading to the more compact form

$$\ddot{\mathbf{r}}_s = -C_R \frac{G_0}{c} \frac{A}{m} \left(\frac{a_\odot}{r_\odot} \right)^2 \hat{\mathbf{n}}. \quad (2.29)$$

For the LRO spacecraft, which is composed of various materials, the assumption of specular reflectivity does not hold true. Thus, the concept of diffuse reflectivity is introduced by splitting β into specular reflectivity, ζ , and diffuse reflectivity, δ . In addition to accounting for diffuse reflectivity, the constant cross-sectional area has to be replaced by a changing area due to LRO's complex shape. For this more general case, the acceleration due to solar radiation pressure consists of a component due to incidence, $\ddot{\mathbf{r}}_i$, a component due to specular reflection, $\ddot{\mathbf{r}}_{sr}$, and a component due to diffuse reflection, $\ddot{\mathbf{r}}_{dr}$. Summing these three components results in the following expression (Cook, 2001; Milani et al., 1987):

$$\begin{aligned}\ddot{\mathbf{r}}_s &= \ddot{\mathbf{r}}_i + \ddot{\mathbf{r}}_{sr} + \ddot{\mathbf{r}}_{dr} \\ &= -\frac{G_0}{c} \frac{A \cos \theta}{m} \left[\left(\frac{2}{3} \delta + 2\zeta \cos \theta \right) \left(\frac{a_\odot}{r_\odot} \right)^2 \hat{\mathbf{n}} + (1 - \zeta) \left(\frac{a_\odot}{r_\odot} \right)^2 \hat{\mathbf{s}} \right],\end{aligned}\tag{2.30}$$

where θ is the angle between the satellite surface normal and the direction to the Sun, and $\hat{\mathbf{s}}$ is the unit vector from the satellite to the Sun. Further, ζ and δ are given in percent of total incident radiation.

Whenever a satellite's shape is approximated by plates (with N being the total number of plates), the overall solar radiation pressure acting on a spacecraft is computed by summing the accelerations acting on each plate i (Milani et al., 1987; Marshall et al., 1992) using

$$\begin{aligned}\ddot{\mathbf{r}}_s &= -\frac{G_0}{c} \times \\ &\sum_i^N \frac{A_i \cos \theta_i}{m} \left[\left(\frac{2}{3} \delta_i + 2\zeta_i \cos \theta_i \right) \left(\frac{a_\odot}{r_\odot} \right)^2 \hat{\mathbf{n}}_i + (1 - \zeta_i) \left(\frac{a_\odot}{r_\odot} \right)^2 \hat{\mathbf{s}} \right].\end{aligned}\tag{2.31}$$

Here, the term $A_i \cos \theta_i$ denotes the projected plate area that is maximum when the Sun rays strike the plate in a 90° angle. Again, the solar radiation

pressure coefficient C_R is introduced yielding

$$\ddot{\mathbf{r}}_s = -C_R \frac{G_0}{c} \times \sum_i^N \frac{A_i \cos \theta_i}{m} \left[\left(\frac{2}{3} \delta_i + 2\zeta_i \cos \theta_i \right) \left(\frac{a_\odot}{r_\odot} \right)^2 \hat{\mathbf{n}}_i + (1 - \zeta_i) \left(\frac{a_\odot}{r_\odot} \right)^2 \hat{\mathbf{s}} \right]. \quad (2.32)$$

In contrast to the formulation for geodetic satellites, where C_R has a physical meaning, it represents merely an overall scale factor at this place that is usually estimated (Konopliv et al., 2006).

Acceleration due to planetary radiation pressure

A fraction of the solar radiation reaching a planetary body is immediately reflected off the surface as short wavelength (between 0.2 and 4 μm) energy. The remaining part is absorbed by the planet and later emitted as long wavelength (between 4 and 50 μm) Infrared (IR) radiation (Knocke, 1989). The reflected part, which is also called albedo, undergoes considerable variations over an orbital revolution as it depends on the sunlit planetary area. The IR radiation, in contrast, is much smoother. For the computation of the acceleration due to planetary radiation, Knocke et al. (1988) divides the planetary surface seen from the satellite in a number of rings and these rings further into concentric ring segments. For each of these segments or spots, the acceleration due to planetary radiation pressure is computed and then summed, yielding the overall acceleration due to planetary radiation pressure, $\ddot{\mathbf{r}}_p$:

$$\ddot{\mathbf{r}}_p = -\frac{1}{c} \frac{A}{m} \sum_{j=1}^J G_j \cos \theta_j \left[\left(\frac{2}{3} \delta + 2\zeta \cos \theta_j \right) \hat{\mathbf{n}} + (1 - \zeta) \hat{\mathbf{s}}_j \right]. \quad (2.33)$$

Here, G_j is the radiation flux originating from planetary spot j , c is the velocity of light, A is the satellite cross-sectional area, m is the satellite mass, J is the total number of surface elements, θ_j is the angle between the satellite surface normal and planetary spot, ζ and δ denote specular and diffuse reflectivity, respectively, $\hat{\mathbf{n}}$ is the satellite surface normal unit vector, and $\hat{\mathbf{s}}_j$ is the unit vector from planetary spot j to the satellite. The radiation flux G_j has a short wavelength component, G_j^a , due to albedo and a long wavelength component, G_j^e , due to emissivity ($G_j = G_j^a + G_j^e$). In case of

albedo, the amount of radiation received by the spacecraft at distance r_j from the planetary spot due to an elemental planetary surface area dA_j is

$$G_j^a = \frac{a_j G_0}{\pi r_j^2} \left(\frac{a_\odot}{r_\odot} \right)^2 \cos \theta_j^\odot \cos \gamma_j dA_j. \quad (2.34)$$

Here, a_j denotes the albedo of planetary spot j , G_0 is the radiation flux from the Sun at 1 AU, a_\odot is the semimajor axis of the Earth's orbit around the Sun, r_\odot is the satellite orbital radius from the Sun, θ_j^\odot is the angle between the unit normal of planetary spot j and the direction to the Sun, and γ_j is the angle between the unit normal of planetary spot j and the direction to the satellite. The IR radiation received by the satellite amounts to

$$G_j^e = \frac{e_j G_0}{4\pi r_j^2} \left(\frac{a_\odot}{r_\odot} \right)^2 \cos \gamma_j dA_j, \quad (2.35)$$

with e_j denoting the emissivity of planetary spot j . Inserting Equations (2.34) and (2.35) into Equation (2.33) gives

$$\begin{aligned} \ddot{\mathbf{r}}_p = & -\frac{G_0}{c} \left(\frac{a_\odot}{r_\odot} \right)^2 \frac{A}{m} \sum_{j=1}^J \cos \theta_j \frac{dA_j \cos \gamma_j}{\pi r_j^2} \left(a_j \cos \theta_j^\odot + \frac{1}{4} e_j \right) \\ & \left[\left(\frac{2}{3} \delta + 2\zeta \cos \theta_j \right) \hat{\mathbf{n}} + (1 - \zeta) \hat{\mathbf{s}}_j \right]. \end{aligned} \quad (2.36)$$

In case the central body is the Earth, the standard procedure for the computation of albedo and emissivity is to use the model introduced by Knocke et al. (1988) and Knocke (1989) taking the zeroth, first, and second degree zonal harmonics into account. According to Knocke (1989) the model is good enough to simulate both the latitudinal variation in Earth radiation and a small hemispherical asymmetry depending on seasons (Knocke et al., 1988). Albedo and emissivity are expressed as

$$\begin{aligned} a &= a_0 + a_1 P_1(\sin \varphi) + a_2 P_2(\sin \varphi), \quad \text{and} \\ e &= e_0 + e_1 P_1(\sin \varphi) + e_2 P_2(\sin \varphi). \end{aligned} \quad (2.37)$$

Albedo and emissivity parameters of the model are denoted by a_0 , a_1 , a_2 , c_0 , c_1 , c_2 , and e_0 , e_1 , e_2 , k_0 , k_1 , k_2 , respectively, P_1 and P_2 are the Legendre

polynomials of first and second degree, and φ denotes the latitude. Using the model developed by Knocke et al. (1988), the parameters are as follows:

$$\begin{aligned}
 a_0 &= 0.34 \\
 a_1 &= c_0 + c_1 \cos(\omega (JD - t_p)) + c_2 \sin(\omega (JD - t_p)) \\
 a_2 &= 0.29 \\
 c_0 &= 0.00 \\
 c_1 &= 0.10 \\
 c_2 &= 0.00,
 \end{aligned} \tag{2.38}$$

$$\begin{aligned}
 e_0 &= 0.68 \\
 e_1 &= k_0 + k_1 \cos(\omega (JD - t_p)) + k_2 \sin(\omega (JD - t_p)) \\
 e_2 &= -0.18 \\
 k_0 &= 0.00 \\
 k_1 &= -0.07 \\
 k_2 &= 0.00.
 \end{aligned} \tag{2.39}$$

In Equations (2.38) and (2.39), ω is the frequency of periodic Earth radiation coefficients amounting to $2\pi/365.25 \text{ days}^{-1}$, JD is the Julian date of interest, and t_p is the epoch of the periodic terms (December 22, 1981).

For the Moon, a spherical harmonic model describing the albedo up to degree and order (d/o) 15 is available – the Delft Lunar Albedo Model 1 (DLAM-1) (cf. Figure 2.2, bottom). The primary source of this product are images from the Clementine mission (cf. Figure 2.2, top, for an image example); absolute albedo measurements contribute to a minor part. When using DLAM-1, a can be computed for any evaluation point at latitude, φ , and longitude, λ , according to Floberghagen et al. (1999) by

$$a(\varphi, \lambda) = \sum_{n=0}^{15} \sum_{m=0}^n P_{nm}(\sin \varphi) [C_{nm}^a \cos(m\lambda) + S_{nm}^a \sin(m\lambda)]. \tag{2.40}$$

Degree and order are denoted by n and m , respectively, P_{nm} are the associated Legendre functions, and C_{nm}^a, S_{nm}^a are the spherical harmonic coefficients of the albedo map. The emissivity e is equal to 0.97.

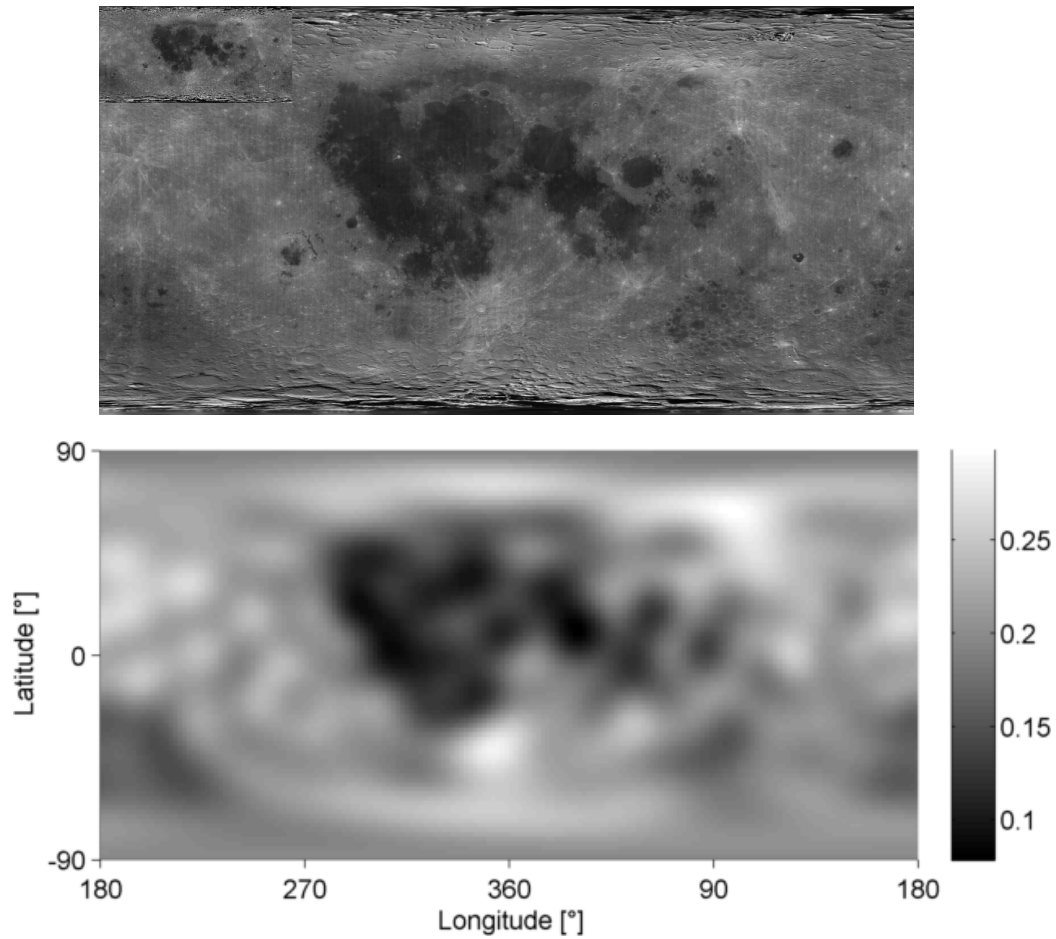


Figure 2.2: Mosaic of Clementine imagery used for the derivation of the lunar albedo model DLAM-1 (top). The spherical harmonic coefficients of DLAM-1 evaluated on a grid (bottom). Regions of high reflectance in the Clementine mosaic have high albedo values in the DLAM-1 and vice versa.

Concerning geodetic satellites the acceleration due to planetary radiation [cf. Equation (2.36)] simplifies to

$$\ddot{\mathbf{r}}_p = -C_R \frac{G_0}{c} \left(\frac{a_\odot}{r_\odot} \right)^2 \frac{A}{m} \sum_{j=1}^J \frac{dA_j \cos \gamma_j}{\pi r_j^2} \left(a_j \cos \theta_j^\odot + \frac{1}{4} e_j \right) \hat{\mathbf{n}}. \quad (2.41)$$

For satellites of complex shape, such as LRO, the acceleration due to planetary radiation is computed for each plate i separately (N being the number of plates). The summation over all plate accelerations gives the total acceleration

$$\ddot{\mathbf{r}}_p = -\frac{G_0}{c} \left(\frac{a_\odot}{r_\odot} \right)^2 \sum_{i=1}^N \sum_{j=1}^J \frac{A_i \cos \theta_{ij}}{m} \frac{dA_j \cos \gamma_j}{\pi r_j^2} \left(a_j \cos \theta_j^\odot + \frac{1}{4} e_j \right) \left[\left(\frac{2}{3} \delta_i + 2\zeta_i \cos \theta_{ij} \right) \hat{\mathbf{n}}_i + (1 - \zeta_i) \hat{\mathbf{s}}_j \right], \quad (2.42)$$

where θ_{ij} denotes the angle between normal vector of satellite plate i and planetary spot j . According to Marshall et al. (1992), the average value for Earth's albedo is about 0.34 (1 for perfect reflection of a white surface), and the average emissivity is 0.68 (1 for a true black body). The average value for Moon's albedo is 0.20, and the average emissivity is 0.97².

Acceleration due to spacecraft thermal radiation

Acceleration due to spacecraft radiation is only listed for the sake of completeness. Its magnitude depends on the temperature of the satellite, which is affected by a complex interaction of external fluxes (solar radiation and planetary radiation) and – for active satellites only – internal fluxes (satellite components dissipate radiation heating the satellite surfaces). Formulas can be found in Marshall et al. (*ibid.*) or Milani and Gronchi (2010, Chapter 14). To the author's knowledge no temperature algorithms are available neither for geodetic satellites nor the LRO spacecraft which is why this non-gravitational acceleration has been neglected.

Shadow function

Both the acceleration due to solar radiation pressure and the acceleration due to planetary radiation pressure depend on the illumination of the satellite.

²both values are based on the DLAM-1 model

To determine the shadow function, GEODYN makes use of a conical model. Instead of distinguishing between two cases (total eclipse or umbra and no eclipse) as it is the case for cylindrical models, conical models are refined by accounting for partial illumination or penumbra (see Figure 2.3). To determine whether the satellite is in umbra, penumbra, or in full Sun, the angle between the satellite and the Sun as seen from the central body is needed as well as the apparent radii of the central body and the Sun³ (see Cook, 2001, for a detailed formulation). The shadow function, κ , describes the eclipse conditions of the satellite and is bounded between 0 and 1:

- $\kappa = 1$ if the satellite is in full Sun
- $0 \leq \kappa \leq 1$ if the satellite is in penumbra
- $\kappa = 0$ if the satellite is in umbra.

In case of penumbra, κ is deduced from the fraction of the solar disk that is not obscured by the eclipsing body.

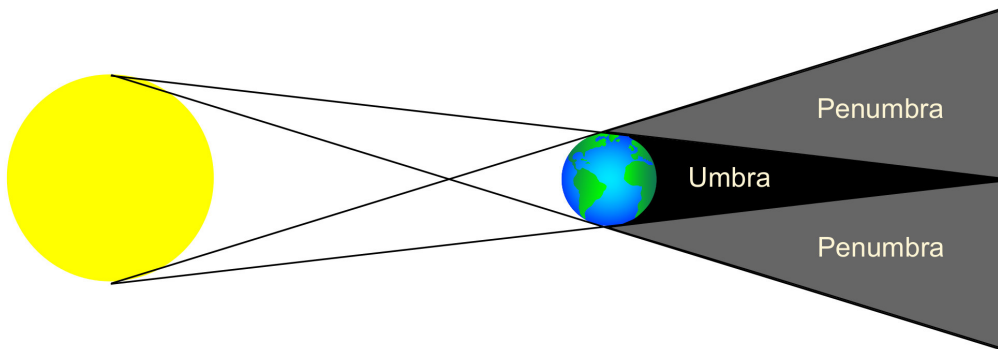


Figure 2.3: Conical Earth shadow model.

At this point expressions are given for geodetic satellites (for LRO the shadow functions are applied in the same way). To account for illumination differences in the acceleration due to solar radiation, Equation (2.29) changes to

$$\ddot{\mathbf{r}}_s = -\kappa C_R \frac{G_0}{c} \frac{A}{m} \left(\frac{a_\odot}{r_\odot} \right)^2 \hat{\mathbf{n}}. \quad (2.43)$$

³The apparent radius of the central body, for instance, is the angular radius of the central body as seen from the satellite's perspective.

Concerning the acceleration induced by planetary radiation, Equation (2.41) is extended by κ in the following manner:

$$\ddot{\mathbf{r}}_p = -C_R \frac{G_0}{c} \left(\frac{a_\odot}{r_\odot} \right)^2 \frac{A}{m} \sum_{j=1}^J \frac{dA_j \cos \gamma_j}{\pi r_j^2} \left(\kappa_j a_j \cos \theta_j^\odot + \frac{1}{4} e_j \right) \hat{\mathbf{n}}. \quad (2.44)$$

Here, κ_j denotes the shadow function of planetary spot j . Note that the emissivity is not affected by the shadow function as it does not cease to exist when the planetary surface is in umbra (Knocke, 1989).

2.1.3 Empirical acceleration

Force modeling – especially non-gravitational force modeling – is imperfect. Thus, empirical parameters are introduced to absorb the residual accelerations. These parameters are estimated in the spacecraft reference frame, that is in along track, cross track, and radial direction. Typically, constant and 1-cycle per revolution (1-cpr) empirical parameters are estimated. The estimation of the latter is motivated by the fact that the attitude of the bus and its appendages relative to the central body and the Sun is repeated almost exactly for each revolution (Colombo, 1989). Considering constant and 1-cpr empirical parameters results in the following expression for the empirical acceleration $\ddot{\mathbf{r}}_{\text{emp}}$ (Colombo, 1989; Montenbruck and Gill, 2001):

$$\ddot{\mathbf{r}}_{\text{emp}} = A_e \cos \nu + B_e \sin \nu + C_e, \quad (2.45)$$

where $e = 1, 2, 3$ for along track, cross track, and radial directions. Further, A , B , and C denote the empirical parameters (A and B are the 1-cpr coefficients, C is a constant acceleration bias), and ν is the true anomaly⁴.

2.2 Observation models

Describing the state deviation and observation deviation by a set of linear differential equations (see Equation 2.7 for more details) gives

$$\mathbf{y}_i = \mathbf{Y}_i - \mathbf{Y}_i^* = \tilde{\mathbf{H}}_i \mathbf{x}_i + \boldsymbol{\epsilon}_i. \quad (2.46)$$

⁴Note that for a non-equatorial orbit, ν is the angle between the satellite position vector and the intersection of the orbit plane with the equator (McCarthy et al., 1993).

This section is dedicated to the expression of the observation, \mathbf{Y}_i , and the computed observation, \mathbf{Y}_i^* , for two-way laser ranges to geodetic satellites, one-way laser ranges to LRO, and two-way Doppler range-rates to LRO.

2.2.1 Observation model for geodetic satellites

Stations performing two-way SLR measurements to geodetic satellites emit laser pulses. The satellites, in turn, reflect the pulses back to the stations as they are equipped with retroreflectors. The observed round-trip light time, $\Delta\tau_2$, of the pulse from the station to the satellite and back to the station can be transferred to the observed one-way distance between station and satellite, ρ^o , following Rim and Schutz (2002):

$$\rho^o = \frac{1}{2}c\Delta\tau_2, \quad (2.47)$$

where c is the speed of light and $\Delta\tau_2$ is affected by measurement errors. Optical measurements are, for instance, subject to tropospheric delays that are discussed later for the computed ranges. Note that for two-way laser ranges to geodetic satellites, \mathbf{Y}_i in Equation 2.46 is given by Equation 2.47.

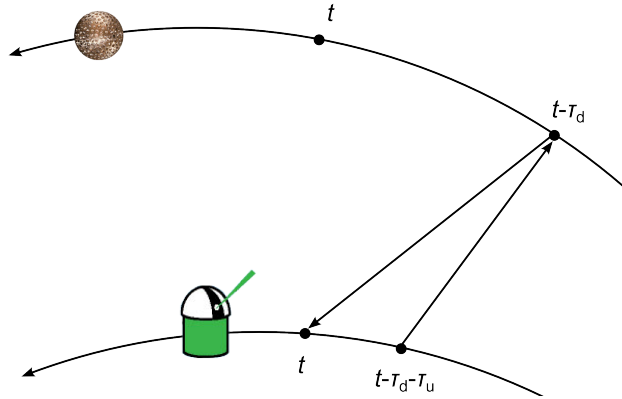


Figure 2.4: The motion of a geodetic satellite and a ground station during the signal travel time of two-way range measurements. When the ground station receives the reflected laser beam at time t , it was reflected by the satellite at $t - \tau_d$ and emitted by the station at $t - \tau_d - \tau_u$.

For the expression of the computed one-way distance between station and satellite one has to keep in mind that the measurement is composed by an

uplink range from the station to the satellite, and a downlink range from the satellite back to the station (see Figure 2.4). When a signal is received at the station at time t , it was reflected at the satellite at time $t - \tau_d$, and transmitted by the station at time $t - \tau_d - \tau_u$. Downlink and uplink light travel time are denoted by τ_d and τ_u , respectively. Downlink range, ρ_d , and uplink range, ρ_u , are thus defined by

$$\begin{aligned}\rho_d &= \|\mathbf{r}(t - \tau_d) - \mathbf{r}_{\text{stat}}(t)\|, \\ \rho_u &= \|\mathbf{r}_{\text{stat}}(t - \tau_d - \tau_u) - \mathbf{r}(t - \tau_d)\|.\end{aligned}\tag{2.48}$$

In the formula above, \mathbf{r}_{stat} and \mathbf{r} specify the geocentric positions of the ground station and the satellite, respectively. Two points in time are involved in the expression for both downlink and uplink range. The computation of the light travel time, τ , which is part of Equation (2.48), is an iterative process (see Appendix A for more details) involving the relativistic light time correction (cf. Section 2.2.5). The iteration process to find the final light travel time of the signal is described in detail by Moyer (2000, Section 8).

The expressions for downlink and uplink [cf. Equation (2.48)], which contain the general relativity correction $\Delta\rho_{\text{rel}}$ through τ , are expanded by tropospheric delay correction, $\Delta\rho_{\text{trop}}$, (cf. Section 2.2.4), and center of mass correction, $\Delta\rho_{\text{com}}$, yielding the expressions for corrected downlink and uplink, $\tilde{\rho}_d$ and $\tilde{\rho}_u$, respectively:

$$\begin{aligned}\tilde{\rho}_d &= \rho_d + \Delta\rho_{\text{trop}} + \Delta\rho_{\text{com}}, \\ \tilde{\rho}_u &= \rho_u + \Delta\rho_{\text{trop}} + \Delta\rho_{\text{com}}.\end{aligned}\tag{2.49}$$

The value of $\Delta\rho_{\text{com}}$ depends on the laser ranging system and on the detection energy level (Otsubo and Appleby, 2003). The computed one-way distance, ρ^c , is finally obtained by averaging the corrected uplink range, $\tilde{\rho}_u$ and the corrected downlink range, $\tilde{\rho}_d$:

$$\rho^c = \frac{1}{2}(\tilde{\rho}_d + \tilde{\rho}_u).\tag{2.50}$$

Note that the computed range given in Equation 2.50 corresponds to \mathbf{Y}_i^* in Equation 2.46.

2.2.2 Observation models for LRO

A small receiver telescope is mounted on and co-aligned with the LRO HGA capturing the uplinked laser signal. A fiber optic cable routes the signal to the Lunar Orbiter Laser Altimeter (LOLA) instrument (cf. Figure 2.5) that records the time of the laser signal based on an ultrastable crystal oscillator (Zuber et al., 2010). According to Sun et al. (2013), the observed one-way optical laser range, ρ^o , between a tracking station on Earth, \mathbf{r}_{stat} , and the LRO satellite, \mathbf{r} , is defined as

$$\rho^o = c\Delta\tau_1 - c(t_{\text{ref}_{\text{LRO}}} - t_{\text{ref}_{\text{stat}}}), \quad (2.51)$$

where c is speed of light, $\Delta\tau_1$ is the one-way light time measurement affected by measurement errors, which is equal to the difference between the time-tag of the laser pulse received at LRO and the time-tag of the corresponding laser pulse transmitted from the ground station. Since the reference time of LRO, $t_{\text{ref}_{\text{LRO}}}$, differs from the reference time of the station, $t_{\text{ref}_{\text{stat}}}$, the observed range contains the difference of the two reference times. The observed one-way range to LRO given in Equation 2.51 corresponds to \mathbf{Y}_i of Equation 2.46.

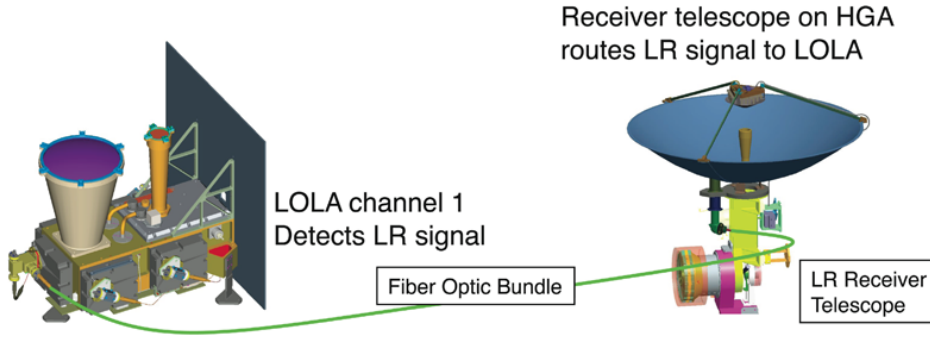


Figure 2.5: Schematic view of the laser ranging flight system from Zuber et al. (2010). The telescope receives the signal from Earth and transmits it to channel 1 of the LOLA receiver via the fiber optic bundle.

For the computed one-way range, GEODYN starts again from the station transmit time, t , and computes the uplink range, ρ_u , using

$$\rho_u = \|\mathbf{r}_{\text{stat}}(t) - \mathbf{r}(t - \tau_u)\|, \quad (2.52)$$

where τ_u is the uplink light travel time⁵. The uplink range is corrected by the same terms as uplink and downlink for geodetic satellites [cf. Equation (2.49)], that is tropospheric delay $\Delta\rho_{\text{trop}}$ (cf. Section 2.2.4), and center of mass correction $\Delta\rho_{\text{com}}$, plus an additional clock correction term, $\Delta\rho_{\text{cl}}$. Note that, as for geodetic satellites, the correction term due to general relativity is implicitly given in τ (see Section 2.2.5 and Appendix A for more details). The corrected uplink, $\tilde{\rho}_u$, which is equal to the final computed one-way distance, ρ^c , thus reads

$$\rho^c = \tilde{\rho}_u = \rho_u + \Delta\rho_{\text{trop}} + \Delta\rho_{\text{com}} + \Delta\rho_{\text{cl}}. \quad (2.53)$$

Note that the computed one-way range given in Equation 2.53 corresponds to \mathbf{Y}_i in Equation 2.46. The center of mass correction in Equation (2.53) is equivalent to the projection of vector \mathbf{E} pointing from the tracking point, i.e. the receiver telescope mounted on the HGA (Zuber et al., 2010), to the satellite's center of mass onto the unit vector of \mathbf{F} , $\hat{\mathbf{F}}$, pointing from the ground station to the tracking point (see Figure 2.6). This correction requires knowledge about the attitude of the main spacecraft bus as well as the HGA and will be discussed in Chapter 5.3. The clock correction term in Equation (2.53) stems from the non-synchronous clocks (one at the ground station and one aboard the spacecraft) involved in the time-tagging of the one-way measurement. The LRO clock has a drift rate in the order of 21 m/s that is not constant over time thus inducing an aging rate (Mao et al., 2011). In GEODYN, the clock correction is modeled as

$$\Delta\rho_{\text{cl}} = u_1 t + u_2 t^2, \quad (2.54)$$

where u_1 is the LRO clock drift rate, u_2 is the LRO clock aging rate, and t is the time elapsed from the epoch to which the clock parameters are referenced and the observation time. Note that the bias between the two clocks is handled by estimating measurement biases (cf. Section 5.1.2).

Doppler observations are based on the Doppler effect (or Doppler shift) utilizing the phenomenon that the frequency of a wave changes for an observer moving relative to the radio source. The signal is thus shifted in frequency. In

⁵The uplink for the computed one-way range to LRO is equivalent to the downlink for the computed one-way range to geodetic satellites [cf. Equation (2.48)].

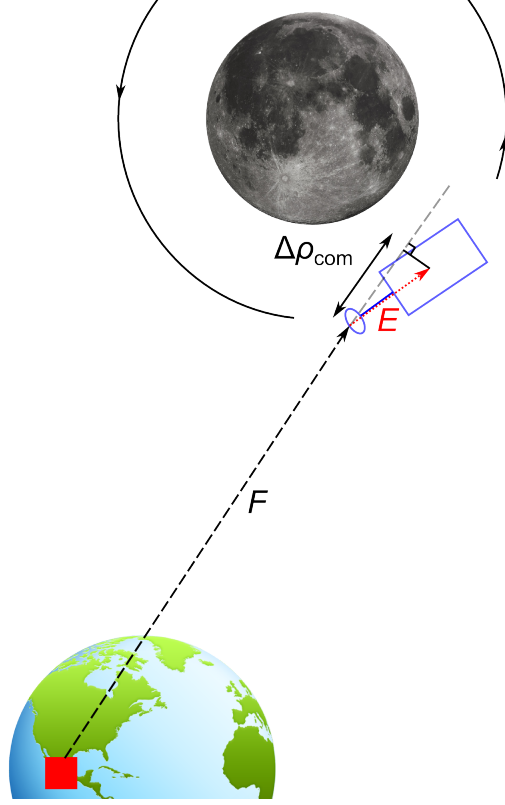


Figure 2.6: For the computation of the center of mass correction, $\Delta\rho_{\text{com}}$, vector \mathbf{E} pointing from the tracking point at the HGA to the satellite's center of mass is projected onto the unit vector of \mathbf{F} , $\hat{\mathbf{F}}$, pointing from the ground station to the tracking point. Hence, the correction term is the dot product between \mathbf{E} and $\hat{\mathbf{F}}$ (McCarthy et al., 1993).

case of two-way Doppler measurements, the spacecraft transponds a signal, which was transmitted from a ground station; the ground-based reference frequency is the same that drives the transmitter aboard the spacecraft (Asmar, 2005). Due to the relative motion between station and satellite caused by the satellite motion, on the one hand, and the rotation of the Earth, on the other hand, the transmitted frequency from the station is shifted in frequency. In case the spacecraft is receding from Earth, the fundamental relationship between transmitted frequency at a station, f_t , and received (Doppler shifted) frequency at the station, f_r , is

$$f_r \cong f_t \left(1 - \frac{1}{c} \frac{d\rho}{dt} \right) = f_t \left(1 - \frac{\dot{\rho}}{c} \right), \quad (2.55)$$

where c is the velocity of light, $\frac{d\rho}{dt}$ is the derivative of the range, ρ , with respect to time, and $\dot{\rho}$ is the relative velocity along the line of sight between observer and satellite (Seeber, 2003).

The Doppler observable, that is the Doppler shift, is derived from the change in the Doppler cycle count D , which accumulates during the count interval T_c at the receiving station on Earth (Moyer, 2000), a bias frequency, f_{bias} , and a frequency-dependent factor, M :

$$f_r - f_t = \frac{1}{M} \left[\frac{\Delta D}{T_c} - f_{\text{bias}} \right]. \quad (2.56)$$

For LRO, M is 1000 as it operates in S-band⁶, T_c is 5 s, and f_{bias} is 240 MHz. Expressing ΔD as a function of D at the time of the present Doppler cycle count, t_2 , and the time of the previous Doppler count, t_1 , gives

$$\Delta D = \frac{D(t_2) - D(t_1)}{T_c}, \quad (2.57)$$

and Equation (2.56) becomes

$$f_r - f_t = \frac{1}{1000} \left\{ \frac{D(t_2) - D(t_1)}{T_c} - 2.4 \times 10^8 \text{ [Hz]} \right\}. \quad (2.58)$$

Rearranging Equation (2.55) so that the relative velocity along the line of sight component is on the left hand side gives

$$\dot{\rho} = \frac{-c}{f_t} (f_r - f_t). \quad (2.59)$$

Hence, the observed one-way range-rate, $\dot{\rho}^o$, has the following form:

$$\dot{\rho}^o = \frac{-c}{2f_t K} \frac{1}{1000} \left\{ \frac{D(t_2) - D(t_1)}{T_c} - 2.4 \times 10^8 \text{ [Hz]} \right\}, \quad (2.60)$$

⁶see http://imbrium.mit.edu/LRORS/DOCUMENT/LRO_DESC_TRK.TXT

with K being the spacecraft transponder turnaround ratio, which is the ratio of the transmitted down-leg frequency at the spacecraft to the received up-leg frequency at the spacecraft (*ibid.*, Section 13). In case that both uplink and downlink frequencies are S-band, as it is the case for LRO, K is $\frac{240}{221}$. For two-way Doppler measurements, \mathbf{Y}_i^* in Equation 2.46 is hence given by Equation 2.60.

The computed one-way Doppler range-rate can be expressed as the difference between the two-way range at the beginning of the count-time interval t_1 , and the two-way range at the end of the count-time interval t_2 (see Figure 2.7)

$$\dot{\rho}^c = \frac{1}{2} \frac{[\tilde{\rho}_u(t_2) + \tilde{\rho}_d(t_2)] - [\tilde{\rho}_u(t_1) + \tilde{\rho}_d(t_1)]}{T_c}, \quad (2.61)$$

where $\tilde{\rho}_u$ and $\tilde{\rho}_d$ denote the uplink and downlink range corrected by tropospheric delay (cf. Section 2.2.4), ionospheric delay (cf. Section 2.2.4), general relativity (cf. Section 2.2.5), and center of mass correction (see Figure 2.6).

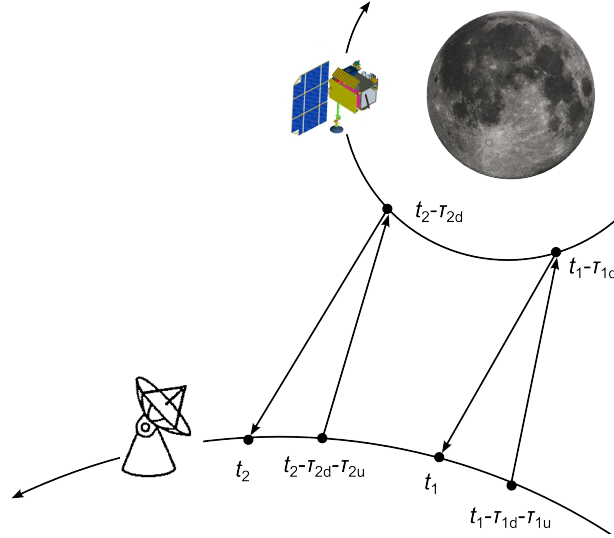


Figure 2.7: The motion of LRO and a ground station during the signal travel time of two-way Doppler measurements. Starting at the end of the count interval t_2 , the signal was transponded by the satellite at $t_2 - \tau_{2d}$, and transmitted by the station at $t_2 - \tau_{2d} - \tau_{2u}$. Similarly, if t_1 denotes the beginning of the count interval T_c , the signal was transponded by the satellite at $t_1 - \tau_{1d}$, and transmitted by the station at $t_1 - \tau_{1d} - \tau_{1u}$.

The corrected downlink and uplink thus read

$$\begin{aligned}\tilde{\rho}_d &= \rho_d + \Delta\rho_{\text{trop}} + \Delta\rho_{\text{ion}} + \Delta\rho_{\text{rel}} + \Delta\rho_{\text{com}}, \\ \tilde{\rho}_u &= \rho_u + \Delta\rho_{\text{trop}} + \Delta\rho_{\text{ion}} + \Delta\rho_{\text{rel}} + \Delta\rho_{\text{com}}.\end{aligned}\tag{2.62}$$

For the expressions of ρ_u and ρ_d see Equation (2.48). The computed range-rate (cf. Equation 2.61) corresponds to \mathbf{Y}_i^* in Equation 2.46.

2.2.3 Station displacements

The position of the tracking station enters all observation models described in the previous sections. Thus, it is necessary to consider the effects of the displacement of the ground station location caused by crustal motions. Among those motions, tectonic plate motion and tidal effects are the most prominent ones (Rim and Schutz, 2002). The total displacement due to tidal effects, Δ_t , is comprised by the displacement due to the solid Earth tides, Δ_{et} , the displacement due to the ocean tide loading, Δ_o , the displacement due to the rotational deformation, i.e. Earth pole tide loading, Δ_{ep} , and ocean pole tide loading, Δ_{op} , and the displacement due to atmospheric pressure loading, Δ_{atm} :

$$\Delta_t = \Delta_{\text{et}} + \Delta_o + \Delta_{\text{ep}} + \Delta_{\text{op}} + \Delta_{\text{atm}}.\tag{2.63}$$

In addition to tidal loading, stations are effected by non-tidal loading such as non-tidal ocean and atmospheric pressure loading. Sošnica (2014), for instance, took the non-tidal atmospheric pressure loading into account to remove the so-called Blue-Sky effect⁷. For some stations this correction is as large as 2.5 mm (*ibid.*).

2.2.4 Media corrections

Electromagnetic signals experience propagation delays due to the atmosphere, i.e. the neutral atmosphere or troposphere, on the one hand, and the charged atmosphere or ionosphere on the other hand. The resulting delay in the measurements depends on atmospheric conditions and on the satellite elevation angle (Hopfield, 1971). In the following, the delays for optical and radio signals due to propagation are briefly discussed.

⁷Optical measurements such as SLR do not penetrate clouds. Thus, the air pressure is generally high deforming the Earth's crust and systematically shifting the station heights.

Tropospheric Refraction

The troposphere is the lower part of the atmosphere (up to approximately 20 km above sea level) and is composed almost entirely of neutral gas. The refractivity decreases with increasing altitude approaching zero at the upper boundary of the troposphere. Generally, the neutral atmosphere can be divided into two constituents, a dry (or hydrostatic) component and a wet (or non-hydrostatic) component. About 90% of the total zenith delay is due to the dry component (Yunck, 1993) which can be accurately modeled as it is highly uniform and stable. Each component consists of the product of the propagation delay experienced in the zenith direction and a Mapping Function (MF) modeling the elevation angle dependence of the zenith atmospheric delay.

Until a few years ago, the atmospheric model developed by Marini and Murray (Marini and Murray, 1973) was commonly used within the SLR community for the correction of observed laser ranges above 10° elevation angle. It is based on meteorological measurements at the laser sites and reflects the slight frequency dependence of the atmospheric delay at optical frequencies (Yunck, 1993). In 2002, Mendes et al. (2002) published two new MFs (one requiring site location and meteorological data, the other requiring only site location) with significant improvements over other MFs. They are based on ray tracing of globally distributed radiosonde stations through the year 1999 and are valid at elevation angles above 3° . In 2004, Mendes and Pavlis (2004) presented improved zenith delay models as well. The use of those delay models together with the new MF is recommended by the IERS (Petit and Luzum, 2010).

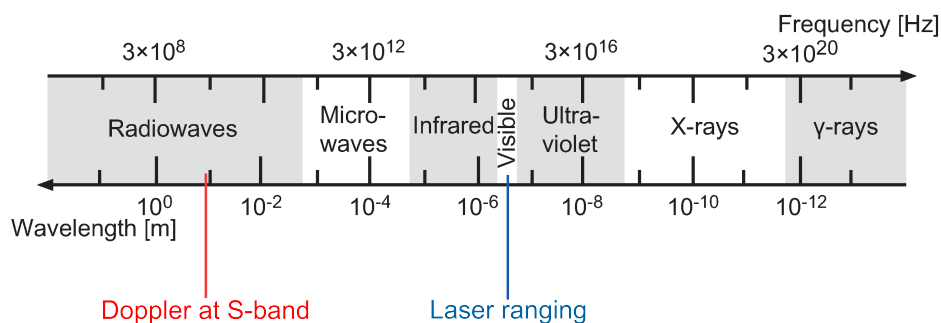


Figure 2.8: The electromagnetic spectrum from radiowaves to γ -rays. Frequency/wavelength of Doppler range-rate measurements to LRO and of optical laser ranges to LRO and geodetic satellites are indicated.

For radio waves, the troposphere is a non-dispersive medium (no frequency dependency in the delay). The troposphere has the effect of steepening the slope of the curve of the Doppler frequency versus time as observed by a tracking station; the satellite appears slightly closer to the station than it actually is (Hopfield, 1963). Contrary to optical signals, the wet component has a larger impact on radio signals (Hopfield, 1971). For the tropospheric correction of radio signals the two-quartic model by Hopfield (Hopfield, 1969) is widely used⁸ yielding an error of less than 10% for elevations above 10° (Montenbruck and Gill, 2001). This model treats the dry and wet components separately representing each by a fourth-degree function of height above the geoid (Hopfield, 1969). An alternative model, which is mainly used to correct GNSS data and Very Long Baseline Interferometry (VLBI) observations, is the Vienna Mapping Function (VMF) 1 by Böhm et al. (2006). As a concluding remark it can be said that the atmospheric dry delay at optical and radio frequencies is nearly the same (Yunck, 1993).

Ionospheric Refraction

The ionosphere, spreading from about 70 km to a height of about 1000 km, is composed of electrons and – considerably heavier – positive ions. Thus, the latter hardly affect the electromagnetic signal (being in principle an oscillating electromagnetic field) and can be ignored (*ibid.*). The ionospheric refractivity is proportional to the inverse of the signal frequency squared and directly proportional to the electron number density. Since optical laser ranges have a frequency in the range of 10^{14} Hz (cf. Figure 2.8), the effect of ionospheric refraction can be neglected (Montenbruck and Gill, 2001). The ionosphere is difficult to model, which is why often global ionospheric models do not provide adequate accuracy (*ibid.*). Thus, measurements of the Total Electron Content (TEC)⁹ are often used to determine the ionospheric refraction. Moreover, multilink observations allow an isolation of the plasma scintillation (Asmar, 2005). Concerning the LRO spacecraft, no multilink observations are available that would isolate the ionospheric effect. Lemoine et al. (2013) computed the ionospheric correction for the two-way Doppler measurements (S-band) to GRAIL by means of TEC maps. The processing of three months of observations to GRAIL showed that the Root Mean Square (RMS) of fit of Doppler measurements improved by a maximum of 0.01 mm/s (varying from arc to arc) when ionospheric correction

⁸Lemoine et al. (2013), for instance, used the Hopfield zenith delay model for the tropospheric correction of Doppler data to the GRAIL spacecraft.

⁹typically, global networks of dual-frequency Global Positioning System (GPS) stations measure the TEC along slant paths connecting receivers and satellites

is applied (*ibid.*, Figure 6). As the precision of Doppler measurements to LRO is ~ 1 mm/s (1σ) (Zuber et al., 2010), the correction due to ionospheric refraction is thought to be uncritical. Hence, it remains unconsidered in this work.

2.2.5 Relativistic light time correction

For satellites orbiting the Earth, the relativistic light time correction, $\Delta\rho_{\text{rel}}$, is expressed in the geocentric reference frame. This correction comes from the space-time curvature produced by the gravitational field and only takes the Earth's rotation during light time into account (Huang et al., 1990):

$$\Delta\rho_{\text{rel}} = 2\frac{GM_{\oplus}}{c^2} \ln \left[\frac{\|\mathbf{r}_{\text{stat}}\| + \|\mathbf{r}\| + \|\mathbf{r}_{\text{stat}} - \mathbf{r}\|}{\|\mathbf{r}_{\text{stat}}\| + \|\mathbf{r}\| - \|\mathbf{r}_{\text{stat}} - \mathbf{r}\|} \right]. \quad (2.64)$$

Here, GM_{\oplus} is the Earth's gravitational parameter, c is the velocity of light, $\|\mathbf{r}_{\text{stat}}\|$ is the distance between station and the geocenter, $\|\mathbf{r}\|$ is the distance between the satellite and the geocenter, and $\|\mathbf{r}_{\text{stat}} - \mathbf{r}\|$ is the computed or geometric range between station and satellite.

For a lunar orbiter, the relativistic light time correction is expressed in a solar-system barycentric coordinate system (Moyer, 2000, Section 8):

$$\begin{aligned} \Delta\rho_{\text{rel}} = & \frac{GM_{\odot}}{c^2} \ln \left[\frac{\|\mathbf{r}_{\text{stat}} - \mathbf{r}_{\odot}\| + \|\mathbf{r} - \mathbf{r}_{\odot}\| + \|\mathbf{r}_{\text{stat}} - \mathbf{r}\| + \frac{GM_{\odot}}{c^2}}{\|\mathbf{r}_{\text{stat}} - \mathbf{r}_{\odot}\| + \|\mathbf{r} - \mathbf{r}_{\odot}\| - \|\mathbf{r}_{\text{stat}} - \mathbf{r}\| + \frac{GM_{\odot}}{c^2}} \right] \\ & + \sum_{i=1}^{10} \frac{GM_{b_i}}{c^2} \ln \left[\frac{\|\mathbf{r}_{\text{stat}} - \mathbf{r}_{b_i}\| + \|\mathbf{r} - \mathbf{r}_{b_i}\| + \|\mathbf{r}_{\text{stat}} - \mathbf{r}\|}{\|\mathbf{r}_{\text{stat}} - \mathbf{r}_{b_i}\| + \|\mathbf{r} - \mathbf{r}_{b_i}\| - \|\mathbf{r}_{\text{stat}} - \mathbf{r}\|} \right]. \end{aligned} \quad (2.65)$$

Here, GM_{\odot} is the Sun's gravitational parameter, $\|\mathbf{r}_{\text{stat}} - \mathbf{r}_{\odot}\|$ is the distance between station and Sun, $\|\mathbf{r} - \mathbf{r}_{\odot}\|$ is the distance between the spacecraft and Sun, and $\|\mathbf{r}_{\text{stat}} - \mathbf{r}\|$ is the distance between station and spacecraft. Furthermore, GM_b denotes the gravitational parameter of planet b , $\|\mathbf{r}_{\text{stat}} - \mathbf{r}_b\|$ refers to the distance between station and planet, and $\|\mathbf{r} - \mathbf{r}_b\|$ is the distance between spacecraft and planet. Note that all coordinates refer to a solar-system barycentric coordinate system. The first term of Equation (2.65) accounts for the relativistic light time delay due to the Sun which has the effect of reducing the coordinate velocity of light below c and for the bending

of the light path (Moyer, 2000). Typically, the same term but neglecting the bending is evaluated for every other celestial body of the solar system, i.e. the eight planets, Pluto, and the Moon.

2.3 Least squares adjustment

In the linearized version of the observation equation [second part of Equation (2.7)], there is an unknown state deviation corresponding to each observation deviation. Inserting Equation (2.8) into Equation (2.7), the observation deviation can be written as

$$y_i = \tilde{\mathbf{H}}_i \Phi(t_i, t_k) \mathbf{x}_k + \epsilon_i. \quad (2.66)$$

Now, the state transition matrix is used to map the state deviation from one time to another. The big advantage is that the state deviation does not have to be known for each time of observation. Note that it is assumed that only one quantity is observed at a single epoch ($p=1$). In detail, Equation (2.66) reads

$$\begin{aligned} y_1 &= \tilde{\mathbf{H}}_1 \Phi(t_1, t_k) \mathbf{x}_k + \epsilon_1, \\ y_2 &= \tilde{\mathbf{H}}_2 \Phi(t_2, t_k) \mathbf{x}_k + \epsilon_2, \\ &\vdots \\ y_l &= \tilde{\mathbf{H}}_l \Phi(t_l, t_k) \mathbf{x}_k + \epsilon_l. \end{aligned} \quad (2.67)$$

Using the definitions according to Tapley et al. (2004b)

$$\mathbf{y} \equiv \begin{pmatrix} y_1 \\ y_2 \\ \vdots \\ y_l \end{pmatrix}, \quad \mathbf{A} \equiv \begin{pmatrix} \tilde{\mathbf{H}}_1 \Phi(t_1, t_k) \\ \tilde{\mathbf{H}}_2 \Phi(t_2, t_k) \\ \vdots \\ \tilde{\mathbf{H}}_l \Phi(t_l, t_k) \end{pmatrix}, \quad \boldsymbol{\epsilon} \equiv \begin{pmatrix} \epsilon_1 \\ \epsilon_2 \\ \vdots \\ \epsilon_l \end{pmatrix}, \quad (2.68)$$

and dropping the subscript k for convenience, Equation (2.67) can be expressed as

$$\mathbf{y} = \mathbf{A} \mathbf{x} + \boldsymbol{\epsilon}, \quad (2.69)$$

with \mathbf{y} being the observation deviation, \mathbf{A} the design matrix, \mathbf{x} the state deviation, and $\boldsymbol{\epsilon}$ the observation residual. In this work, Least Squares (LS) adjustment is used to solve for the unknown state deviation \mathbf{x} . Minimization of the weighted squared sum of observation inconsistencies

$$\boldsymbol{\epsilon}^T \mathbf{P} \boldsymbol{\epsilon} \rightarrow \min! \quad \Leftrightarrow \quad (\mathbf{y} - \mathbf{A}\mathbf{x})^T \mathbf{P} (\mathbf{y} - \mathbf{A}\mathbf{x}) \rightarrow \min_{\mathbf{x}}! \quad (2.70)$$

yields the best linear unbiased estimate¹⁰ of \mathbf{x} ,

$$\hat{\mathbf{x}} = (\mathbf{A}^T \mathbf{P} \mathbf{A})^{-1} \mathbf{A}^T \mathbf{P} \mathbf{y}, \quad (2.71)$$

with \mathbf{P} denoting the observation weight matrix.

Concerning the composition of the estimated state deviation vector, it is common practice to make use of the multi-arc strategy where the time span to be investigated is decomposed into shorter intervals or arcs (Milani and Gronchi, 2010, Chapter 15). Each arc has its own initial conditions as if there were a new spacecraft for each arc. This multi-arc approach distinguishes between local fit parameters and global fit parameters. Details of local-global decomposition can be found in Milani and Gronchi (*ibid.*, Chapter 15). Local fit parameters (or arc-specific parameters) are all parameters that change from arc to arc, such as the initial state vector, atmospheric drag coefficient or solar radiation pressure coefficient. Global fit parameters, in contrast, do not depend on a specific arc but are valid over a longer time span, such as gravity field coefficients or ground station positions.

The first step of the parameter estimation process consists of solving for all local parameters. Since the reference solution is generally not very close to the true solution, several iterations are required that are also called inner iterations. Within this first step the global parameters are fixed to their a priori values. Once this system has converged, normal equations for local and global parameters are set up – one normal equation matrix ($\mathbf{A}^T \mathbf{P} \mathbf{A}$) and one normal equation vector ($\mathbf{A}^T \mathbf{P} \mathbf{y}$) per arc. A companion program to GEODYN, SOLVE (Ullman, 1994), can now be used to stack the normal equations of several arcs (and possibly those of different satellites orbiting the same central body) and estimate the global parameters. This is achieved

¹⁰the best linear unbiased estimate is given by the least squares estimator; ‘best’ refers to the lowest variance of the estimate

by reducing the normal equation system of local and global parameters by the arc-specific part (or local parameters). This procedure is equivalent to solving for all (local and global) parameters simultaneously. Correlations between global and arc parameters are thus taken into account. For more details on this technique the reader is referred to Kaula (1966).

After having estimated the local parameters iteratively and solved for the global parameters, the first global iteration is complete. It is now possible to feed the estimated global parameters back to the system by replacing, for instance, the a priori gravity field coefficients used for the first global iteration with the estimated gravity field coefficients and solving again for the local parameters in an iterative manner. After the second global iteration, the residuals are typically smaller than after the first global iteration and are referred to as post-fit residuals.

2.4 Key issues and quality assessment

According to Luthcke et al. (2003), (1) data use, (2) parametrization, and (3) arc length are key issues in solving an orbit determination problem. The first issue, data use, comprises data editing, weighting of observations of the same type, and relative weighting of observations of different types. Data use is no primary objective in this thesis. Instead, the same weight for all observations of the same type were introduced. Also, the normal equations comprising data to different geodetic satellites are equally weighted in the combination process.

The second issue, parametrization, seeks to find the set of parameters that describe the motion of a satellite in an optimal way. As already mentioned, the perturbing forces affecting the satellite are not perfectly known (e.g. atmospheric drag). Also, some forces may not be known well enough to be modeled at all or there is simply no access to relevant information. Spacecraft thermal radiation (cf. Section 2.1.2) shall be mentioned at this place for which, in practice, a model of the external surface temperatures is typically not available with the required accuracy (Milani and Gronchi, 2010, Chapter 14). Ignoring the presence of this force, though, would lead to a degraded orbit solution. Estimating empirical parameters is an effective way to mitigate this problem (cf. Section 2.1.3). The number of empirical parameters that can be resolved depends primarily on the density and the geometry of the available tracking data (Rowlands et al., 2009). Optimal parametrization with respect to the number and the type of empirical parameters is exhaus-

tively studied within this thesis, especially concerning the POD of the LRO. Unlike POD of a lunar orbiter, POD of geodetic satellites has been practiced for several years at the Space Research Institute of the Austrian Academy of Sciences (see e.g. Maier et al., 2012; Maier et al., 2014); naturally, use was made of this experience.

The third key issue, the arc length, has to be addressed whenever the multi-arc strategy (see Section 2.3 for more details) is used. According to Rowlands et al. (2002), the optimal arc length depends on the geometric strength of the tracking data, the magnitude of unmodeled or imperfectly modeled forces, and the sensitivity of the data to the parameters of interest. If the latter are gravity field coefficients, the sensitivity increases with increasing arc length (Rowlands et al., 2002; Goossens, 2010). Thus, longer arcs are generally preferable. The drawback of longer arcs is, however, that the unmodeled accelerations, which accumulated over time, are larger compared to shorter arcs. Bare in mind that if the errors grow too large, the assumption of linearity on which the least squares adjustment is based, does not hold (Goossens et al., 2011a). Thus, the choice of the optimal arc length represents a trade-off between capturing the dynamics of the satellite motion and keeping the residuals small. The quality of the computed orbits was assessed by means of quality indicators introduced in the subsequent paragraph.

Orbital accuracy can only be assessed by estimating the satellite's trajectory using independent tracking data types. For the LRO spacecraft two independent measurement types are available, optical laser ranges, on the one hand, and Doppler range-rates, on the other hand. As will be shown in Section 5.3.2, however, orbits determined from laser ranges are of considerably lower quality compared to orbits determined from Doppler range-rates; sparse tracking and the involvement of two clocks are thought to be the main reasons. Instead, other quality indicators can be used such as the orbital precision that is typically assessed by orbit overlap tests. In the course of these overlap tests the investigated time span is split into arcs that overlap with respect to time. Since the dynamical modeling and the used measurements for the overlap period are the same, the orbit differences give an indication of the consistency of the orbit determination and thus an indication of the minimum error in the final solution (Zandbergen et al., 2003). Some care should be taken though when analyzing overlap values as the least squares adjustment (cf. Section 2.3) used for the orbit determination tends to result in larger errors at the beginning and at the end of each arc (*ibid.*). The most trivial case of overlap analysis would consist in choosing the arcs so that successive arcs are connected by exactly one point; this would allow an

analysis of the difference of the so-called orbit connecting points (Kang et al., 2006). Note that for estimating gravity field coefficients, non-overlapping arcs have to be used since observations within the overlapping period would count twice otherwise.

Further, observation residuals provide a clue on how well the forces acting on the satellite are modeled. If the forces were modeled perfectly, the residuals would be at the level of tracking data precision (*ibid.*). In case of LRO the estimated orbit can be externally validated using LRO ephemeris computed and published by National Aeronautics and Space Administration (NASA).

Chapter 3

Gravity field recovery

Gravity field recovery can be severely hampered by ill-conditioning of the normal equation system. The solution of an ill-conditioned problem strongly oscillates amplifying data errors and unmodeled signal (Kusche and Klees, 2002). As stated in Kusche and Klees (*ibid.*), ill-conditioning has two reasons. First, the determination of gravity field functionals on the central body's surface from satellite sensors lacks stability (also referred to as downward continuation problem). Secondly, incomplete spatial sampling of the central body has a negative effect (Weigelt et al., 2013).

To some extent, one can try to mitigate ill-conditioning. The usage of observations to satellites having a wide range of inclinations has a positive effect on the condition of the normal equations, for instance; the gravitational field is sampled more adequately in latitude (King-Hele, 1962; King-Hele and Cook, 1965). Also, the inclusion of more observation types has a stabilizing effect.

In case the normal equation system remains unstable, the concept of regularization can be applied by adding a priori information to the solution. The classical global regularization method is referred to as Tikhonov-Phillips regularization (Tikhonov, 1963; Phillips, 1962). The Tikhonov-Phillips regularized version of Equation (2.71) reads

$$\hat{\mathbf{x}}_{\eta} = (\mathbf{A}^T \mathbf{P} \mathbf{A} + \eta \mathbf{K})^{-1} \mathbf{A}^T \mathbf{P} \mathbf{y}, \quad (3.1)$$

where η is the regularization parameter and \mathbf{K} is a symmetric regularization

matrix

$$\mathbf{K} = \mathbf{L}^T \mathbf{L}. \quad (3.2)$$

A Tikhonov-Phillips regularized problem is said to be in standard form if $\mathbf{L} = \mathbf{I}$, and in general form if $\mathbf{L} \neq \mathbf{I}$. Here, the latter applies since the regularization matrix was defined to be the Kaula regularization matrix. Consequently, \mathbf{L} in Equation (3.2) is a diagonal matrix containing the inverse of the empirical degree variances known as Kaula's rule (Kaula, 1966):

$$\sigma_n^2 = \left(\frac{1 \times 10^{-5}}{n^2} \right)^2, \quad (3.3)$$

where n denotes the spherical harmonic degree. The regularized solution, $\hat{\mathbf{x}}_\eta$, is subject to the minimization problem

$$\left\{ \underbrace{\|\mathbf{y} - \mathbf{A}\mathbf{x}\|_{\mathbf{P}}^2}_{\text{residual norm}} + \eta \underbrace{\|\mathbf{x}_\eta\|_{\mathbf{K}}^2}_{\text{solution norm}} \right\} \rightarrow \min_{\mathbf{x}}. \quad (3.4)$$

The so-called L-curve method (e.g. Hansen, 1998; Hansen, 2000) was adopted to find the optimal value of the regularization parameter η . This method makes use of the solution norm and the residual norm [cf. Equation (3.4)]. Note that if regularization is too tight, the residual norm will be too large. On the other hand, if regularization is too loose, the fit will be good but the solution norm will be large as it is dominated by the contributions from the data errors (Hansen, 2000). As such, the optimal value for η represents a compromise between data misfit and the power of the solution. Solution and residual norm are typically plotted against each other on a log-log scale as this scale emphasizes the two different parts of the curve forming an 'L' (Hansen, 1998). The optimal regularization parameter corresponds to the point at the corner of the L-shaped curve.

In order to find the optimal value of η , use can be made of a very elegant way to analyze discrete ill-posed problems (e.g. Hansen, 2008) – the Singular Value Decomposition (SVD) for $\mathbf{L} = \mathbf{I}$ or the generalized SVD for $\mathbf{L} \neq \mathbf{I}$.

These concepts are implemented in `regtools`¹, a MATLAB package for analysis and solution of discrete ill-posed problems, developed by P. C. Hansen. As the regularization matrix is chosen to be the Kaula matrix, the use of `regtools` for generalized SVD shall be shortly discussed at this point. Input to the function `l_corner.m`, which plots the L-curve on a log-log scale and returns the optimal η , is the generalized SVD of the matrix pair \mathbf{A} and \mathbf{L} as well as the residual vector \mathbf{y} . For a total number of 200 different values of η the solution norm and the residual norm is computed. Next, a spline is laid through the points and the optimal regularization parameter is found by computing the maximum curvature of that curve.

¹available at <http://www.imm.dtu.dk/~pcha/Regutools/>

Chapter 4

Geodetic satellites

Laser ranging to geodetic satellites is based on the measurement of the round-trip light travel time: a pulse is emitted at a ground station into the direction of a geodetic satellite. The satellite reflects the signal back to the station. The ground station records the time of pulse emittance and the time of arrival of the reflected signal. These dedicated satellites are completely passive free falling objects of spherical shape covered with corner cube reflectors (cf. Figure 4.1). The round-trip light travel time can be easily converted to unambiguous two-way ranges [cf. Equation (2.47)]. For orbit determination purposes so-called Normal Points (NPs) are used. NPs are statistically derived pseudo-observations from integrated raw Satellite Laser Ranging (SLR) measurements over a certain time span or bin size (Sinclair, 1997); they are precise to 1 to 3 mm (Degnan, 2013).



Figure 4.1: Illustration of the LAGEOS-1 satellite. Its surface is covered by 426 corner cube reflectors (image credit: NASA).

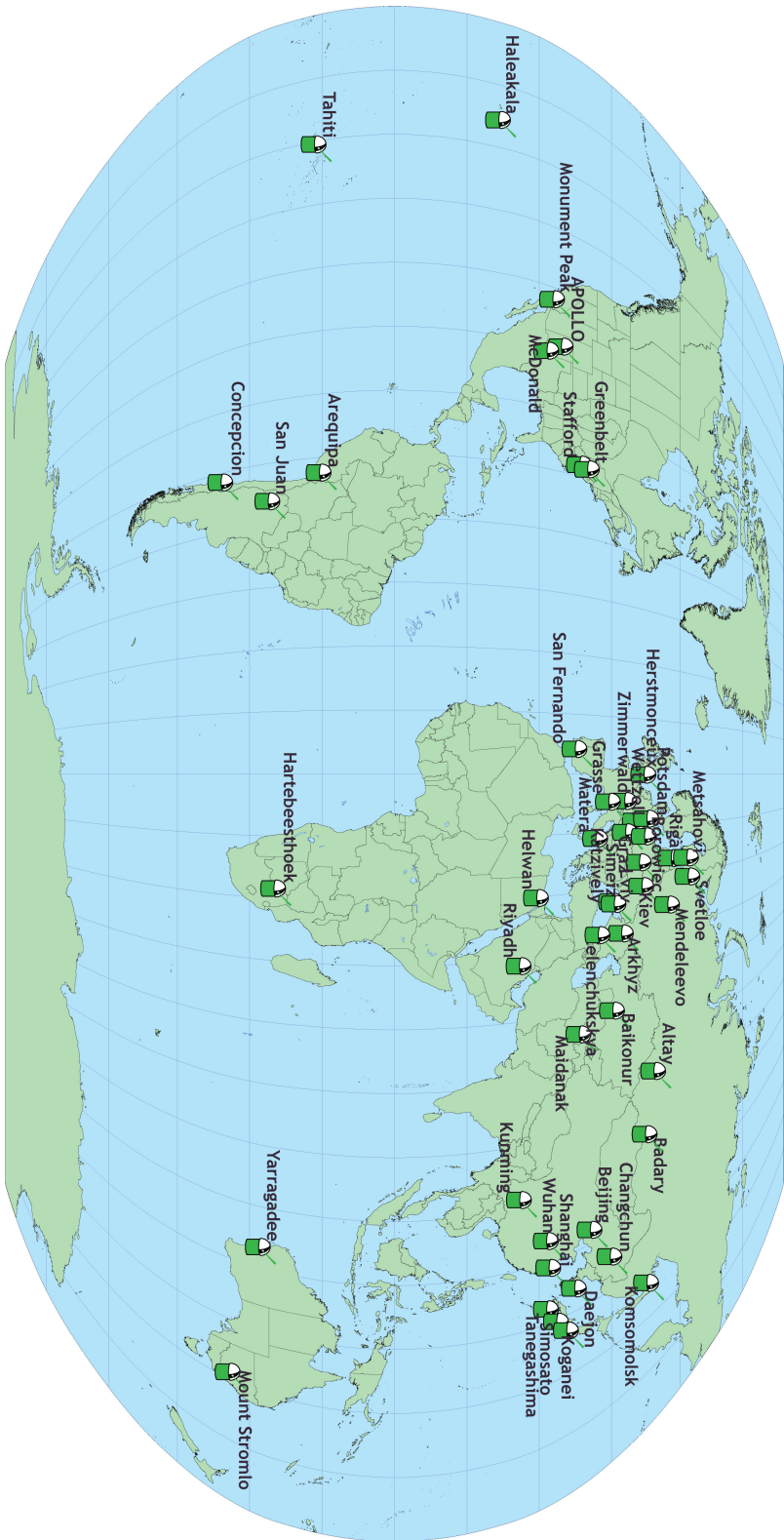


Figure 4.2: ILRS station network (retrieved from <http://ilrs.gsfc.nasa.gov> on July 9, 2014).

The International Laser Ranging Service (ILRS)¹ coordinates satellite tracking by means of optical laser ranges and provides the data to the research community (Pearlman et al., 2002). The ILRS network (Figure 4.2) is a global network and consists of a few tens of stations. It is densest in Europe and is characterized by a hemispheric dichotomy. Stations are missing primarily in the polar regions and in oceanic areas.

4.1 Data set

A total of six geodetic satellites were analyzed over a time span of almost 14 years (January 2000 to October 2013). Satellite parameters, orbital characteristics, and additional information are given in Table 4.1. Some geodetic satellites such as the Laser Geodynamics Satellite (LAGEOS)-1 and Stella have been orbiting the Earth for decades. Their long lifetime can be ascribed to their high orbital altitudes making the atmosphere a negligible perturbing factor. The orbits of all considered satellites are near-circular allowing a uniform sampling of the gravity field with respect to altitude. The satellites have different inclinations decreasing correlations between estimated gravity field coefficients (cf. Chapter 3). Moreover, highly inclined satellites orbiting at high orbital altitudes such as LAGEOS-1 are crucial for expanding the data coverage to the polar regions where no observatories exist (see Figure 4.3). SLR data acquisition is spatially (Figure 4.3) and temporally inhomogeneous; the number of observations per site varies significantly as can be seen from Figure 4.4. Most of the satellites have a small area-to-mass ratio (cf. Table 4.1) diminishing the effect of non-gravitational forces acting on them (cf. Section 2.1.2).

Five out of the six considered satellites have a diameter less or equal to 60 cm. Moreover, the mass of the LAGEOS satellites, Stella, and Starlette is large. Consequently, the area-to-mass ratio of those satellites (cf. Table 4.1) is favorably small as it diminishes the effect of non-gravitational forces acting on them (cf. Section 2.1.2).

Over the ~14-year time span, a total number of about 6.4 million NPs were analyzed. One third of this number amounts to observations to Ajisai. The number of NPs per satellite and the percentage of each satellite contributing to the total number of observations is listed in Table 4.2. All observational data were retrieved from the Crustal Dynamics Data Information System

¹<http://ilrs.gsfc.nasa.gov/>

(CDDIS)², which is discussed in Noll (2010). The EUROLAS Data Center (EDC) is the second data center providing NPs to geodetic satellites. Sośnica et al. (2011) showed that the data provided by CDDIS and EDC is not identical suggesting, thus, to merge the observation files from both centers.

Table 4.1: Characteristics of considered geodetic satellites³.

	LAGEOS-1	LAGEOS-2	Ajisai	Starlette	Stella	Larets
Sponsor	US	US/Italy	Japan	France	France	Russia
Year of launch	1976	1992	1986	1975	1993	2003
Inclination [°]	109.8	52.6	50.0	49.8	98.6	98.2
Eccentricity [-]	0.0045	0.0135	0.0010	0.0206	0.0008	0.0002
Revolution period [min]	225	223	116	104	101	98.5
Perigee [km]	5860	5620	1490	812	800	691
Diameter [cm]	60	60	215	24	24	25
Mass [kg]	407	405	685	47	48	23
Area-to-mass ratio [cm ² /kg]	7	7	53	10	9	20
Bin size of NPs [s]	120	120	30	30	30	30

Table 4.2: Number of NPs per satellite from January 2000 to October 2013.

Satellite	Number of NPs	Percentage
Ajisai	2 176 000	34
Starlette	1 216 000	19
LAGEOS-1	1 088 000	17
LAGEOS-2	1 024 000	16
Stella	576 000	9
Larets	320 000	5
$\Sigma = 6\,400\,000$		

²visit <ftp://cddis.gsfc.nasa.gov>

³all data are retrieved from the ILRS website <http://ilrs.gsfc.nasa.gov> except for the revolution period and the diameter of Larets, which were retrieved from Kucharski et al. (2014)

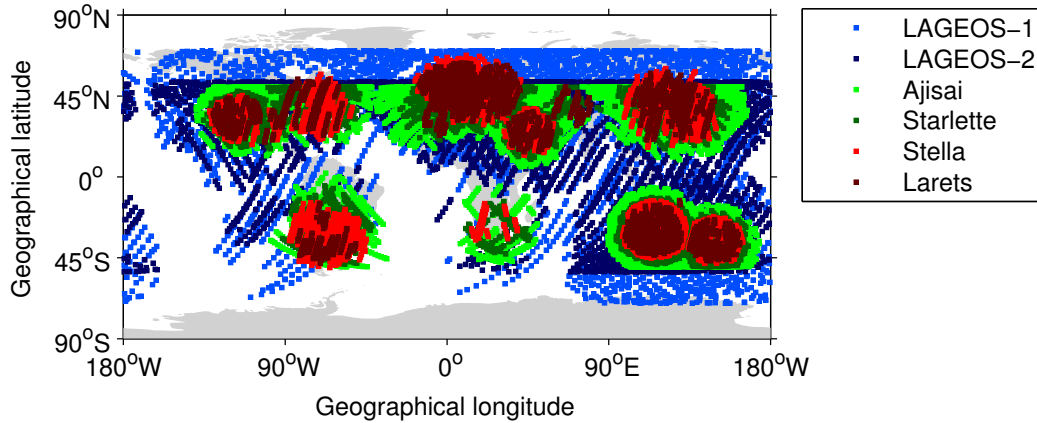


Figure 4.3: Spatial distribution of NPs per satellite in January 2007. Data gaps are located above regions where no stations exist (e.g. polar regions and oceanic areas). LAGEOS-1, which is located at high orbital altitude and is highly inclined (cf. Table 4.1), favorably expands the data coverage into the polar regions.

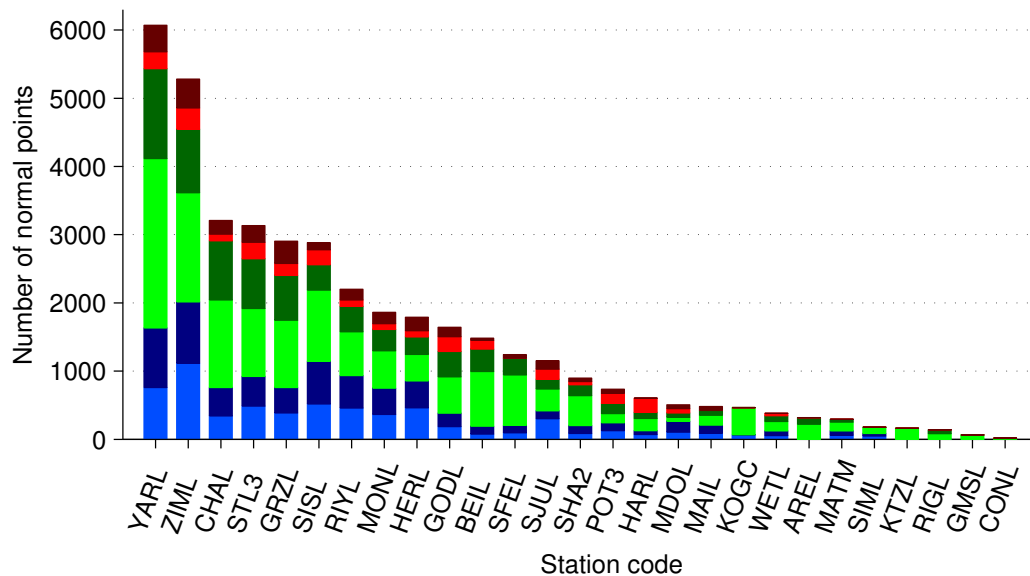


Figure 4.4: Number of NPs per laser station in January 2007. The color scheme is the same as in Figure 4.3.

4.2 Parametrization and modeling

First of all, the NP files were converted to the GEODYN-specific format (cf. Appendix D.1). Then, SLR data of the ~ 14 -year time span were processed in ‘weekly’ batches; each calendar month was subdivided into three seven-day arcs plus a fourth arc of variable length depending on the number of days within the month. Table 4.3 summarizes the standards and models used for Precise Orbit Determination (POD). The adopted standards are motivated by contributing SLR-based normal equations to gravity field models of the Gravity Observation Combination (GOCO) series⁴. For the computation of their latest satellite-only gravity field models, the GOCO consortium agreed to data processing in consistency with the Gravity Field and Steady-State Ocean Circulation Explorer (GOCE) High-level Processing Facility (HPF) standards (EGG-C, 2010). Consequently, the processing of SLR data entering GOCO02S and GOCO03S (the SLR part is the same for both models) is consistent with the GOCE HPF standards. The latter instruct the usage of the Finite Element Solution (FES) ocean tide model FES2004 (Lyard et al., 2006). This model was used for the processing of SLR data that enter the GOCO models. For the analysis of the ~ 14 -year time span presented here, however, the FES model was replaced by the more recent Goddard Ocean Tide (GOT) model GOT4.8 (Ray, 1999), released in 2011.

The satellites orbiting at high altitudes, such as LAGEOS-1 and -2, are less sensitive to the Earth’s gravity field than the lower ones. Sošnica (2014) showed that the LAGEOS satellites are insensitive to coefficients higher than degree and order (d/o) 30 implying that for the analysis of LAGEOS data the a priori gravity field model can be truncated at d/o 30. However, since also lower orbiting satellites were considered in this study, the full d/o of the European Improved Gravity model of the Earth by New techniques (EIGEN), EIGEN-5S, was used for all satellites (d/o 150).

For each satellite, the initial state vector for the very first orbital arc was obtained from predictions in the Tuned Inter-Range Vectors (TIRVs) format⁵ provided by the ILRS. The initial states of all other arcs were taken from the estimated orbit of the respective previous arc, as subsequent arcs were chosen such that they overlap by one point. The integration step size was set to 60 s for all satellites.

The rejection level of NPs was defined as 3.5σ . Further, a minimum number

⁴visit <http://www.goco.eu/> for more information

⁵retrieved from <ftp://cddis.gsfc.nasa.gov/slr/predicts/>

of NPs per station and month was introduced (30 NPs). All laser ranges measured above an elevation angle of 12° were taken into account. Moreover, all measurements were assigned equal weight. The usage of the bin Root Mean Square (RMS) value, which is available for each NP, led to significantly larger range residuals than introducing equal weights for all observations. This might be due to the fact that the computation of the bin RMS value is not standardized. As a consequence, the algorithm to deduce this value might differ from station to station. The impact of using equal weights or the bin RMS value on the estimated monthly sets of gravity field coefficients was investigated: whereas the two observation schemes resulted in nearly the same C_{20} coefficients, the variations of the other degree-two terms were all larger in case the bin RMS was used as observation weight (for more details see Appendix B). This is the reason why equal weights have been introduced.

Table 4.3: Precision orbit determination standards for geodetic satellites

	Standard/model	Reference
<i>Reference frame</i>		
Inertial reference system	ICRF	McCarthy and Petit (2004)
EOPs	IERS 08 C04	Bizouard and Gambis (2007)
Planetary ephemeris	JPL DE-403	Standish et al. (1995)
Polar motion	IERS	McCarthy and Petit (2004)
Precession-nutation model	IAU-2000	Capitaine et al. (2003)
Station coordinates	SLRF2008	Pavlis (2009)
<i>Gravitational force models</i>		
Gravity field model	EIGEN-5S (full d/o)	Förste et al. (2008)
Solid Earth tides	IERS	McCarthy and Petit (2004)
Ocean tides	GOT4.8 up to d/o 20	Ray (1999)
Solid Earth pole tide	IERS	McCarthy and Petit (2004)
Ocean pole tide	IERS	McCarthy and Petit (ibid.)
Third bodies	JPL DE-403	Standish et al. (1995)
Oblateness	indirect acceleration of the Earth due Earth's oblateness	Moyer (1971)
Relativistic corrections	Schwarzschild, Coriolis, Lense-Thirring	
<i>Non-gravitational force models</i>		
Atmospheric drag	atmosphere model MSIS-86	Hedin (1987)
Solar radiation pressure	$G_0=1367.2 \text{ Wm}^{-2}$ at 1 AU, conical shadow model	

Continued on next page

Table 4.3: (continued)

	Standard/model	Reference
Earth radiation pressure	Albedo and emissivity, 2 nd degree zonal model	Knocke (1989)
<i>Satellite parameters</i>		
Cannonball model	Cross sectional area derived from the diameter given in Table 4.1 Mass (cf. Table 4.1)	
<i>Measurement models</i>		
Tropospheric refraction	Mendes-Pavlis zenith delay model	Mendes and Pavlis (2004)
Center of mass correction	FCULa mapping function	Mendes et al. (2002)
	0.9930 m: Ajisai	Sońnica et al. (2012)
	0.2510 m: LAGEOS-1/2	ILRS recommendation
	0.0780 m: Stella/Starlette	Sońnica et al. (ibid.)
Relativistic correction	0.0562 m: Larets	ILRS recommendation
	IERS	McCarthy and Petit (2004)
Station displacement:		
Solid Earth tide loading	IERS	McCarthy and Petit (ibid.)
Ocean tide loading	GOT4.8 up to d/o 20	Ray (1999)
Solid Earth pole tide loading	IERS	McCarthy and Petit (2004)
Ocean pole tide loading	IERS	McCarthy and Petit (ibid.)
Atmospheric pressure loading	not applied	
Non-tidal loading	not applied	

For each week and each satellite the orbit was computed using GEODYN. Various arc parameters (cf. Table 4.4), such as the satellite state vector, were estimated in an iterative manner. After convergence of the orbit a normal equation system was set up for the estimated arc parameters together with the global parameters. The latter consist of gravity field coefficients and station coordinates (cf. Table 4.4). Preceding simulations in Maier et al. (2012) have shown that the recovery of gravity field coefficients is limited to about d/o 5 when using five geodetic satellites. Estimating coefficients up to d/o 10 resulted in large variations of the monthly coefficients due to the increased ill-conditioning of the normal equations (ibid.). Non-global data coverage (cf. Figure 4.3) and the high orbital altitudes of some of the geodetic satellites (cf. Table 4.1) are thought to be responsible for this behavior. SLR data to geodetic satellites have a particular strength for the determination

of the degree-2 terms since errors in non-gravitational force modeling are significantly reduced because of the satellites' spherical shape and large area-to-mass ratio. For this reason and in order to avoid any degradation of the results due to ill-conditioning, the maximum gravity field resolution was set to d/o 4. The coordinate system has been defined to coincide with the Earth's center of mass, implying that the degree-1 coefficients are fixed to zero.

Table 4.4: Estimated arc and global parameters

<i>Arc parameters</i>	
Atmospheric drag coefficient	1 per day
Empirical acceleration	1-cpr along track, constant cross track (1 per day each)
Measurement bias	1 per station and arc
Satellite state vector	1 per arc
<i>Global parameters</i>	
Gravity field coefficients	1 set per month (time-variable solution)
up to d/o 4	1 set over ~ 14 years (static solution)
Station coordinates	same as for gravity field coefficients

From the physical point of view there is no reason why measurement biases should exist since stations are urged to perform system calibrations on a regular basis. Small biases, however, might remain. More importantly, estimated biases can absorb deficiencies in the orbit modeling. Figure 4.5 shows the estimated biases for YARL to LAGEOS-1 and Starlette. The variation is generally larger for the lower orbiting satellite Starlette due to the larger impact of the atmosphere. Moreover, the variations of the biases to Starlette seem to be correlated with the solar activity (see Figure 4.6, bottom) which is small between 2006 and 2010. The estimated measurement biases thus absorb to some extent insufficiently modeled variations of the atmosphere.

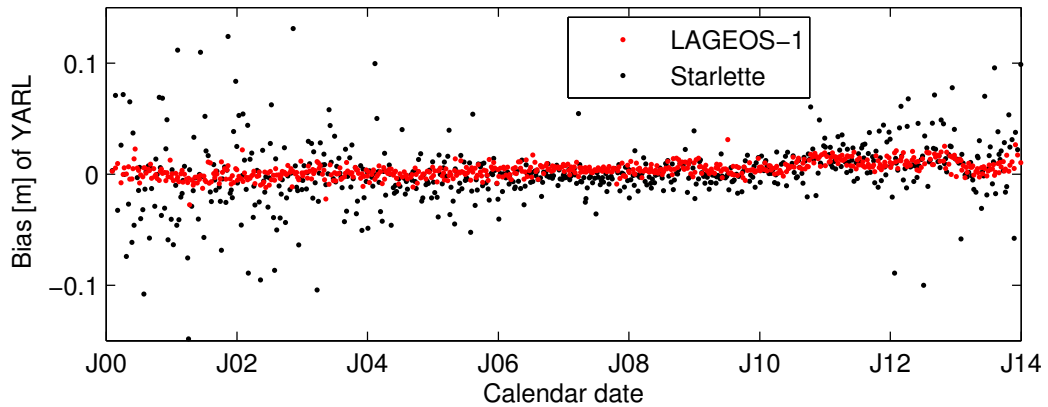


Figure 4.5: Estimated measurement biases per orbital arc from YARL to LAGEOS-1 and Starlette

4.3 Results

The quality of the achieved results can be assessed at the level of computed orbits, on the one hand, and at the level of recovered gravity field coefficients, on the other hand. The outcome of both is presented in this chapter.

4.3.1 Precise orbit determination

As discussed in Section 2.4, observation residuals ($O - C$) are often used as an indicator of how well the the forces acting on the satellite are modeled. Figure 4.6 (top) depicts the RMS values of the post-fit residuals per arc for all considered satellites. The observations can be modeled most precisely for the LAGEOS satellites that are orbiting at altitudes of nearly 6000 km; at altitudes this high the influence of the atmosphere on the motion of the satellite is negligible. The level of the RMS values of the lower satellites is higher, pointing to deficiencies in the modeling of non-gravitational forces such as atmospheric drag and solar radiation pressure. Further, the RMS values of all low-orbiting satellites show a similar pattern: they are large at the beginning and at the end of the investigated time span and small in the middle (cf. Figure 4.6, top). This behavior correlates with the varying activity of the Sun. Figure 4.6 (bottom) depicts the 10.7-cm solar radio flux⁶, which can be considered as a proxy for the solar activity. Table 4.5 contains the RMS values of the post-fit residuals averaged over the investigated time span.

⁶retrieved from <https://celestrak.com/SpaceData/>

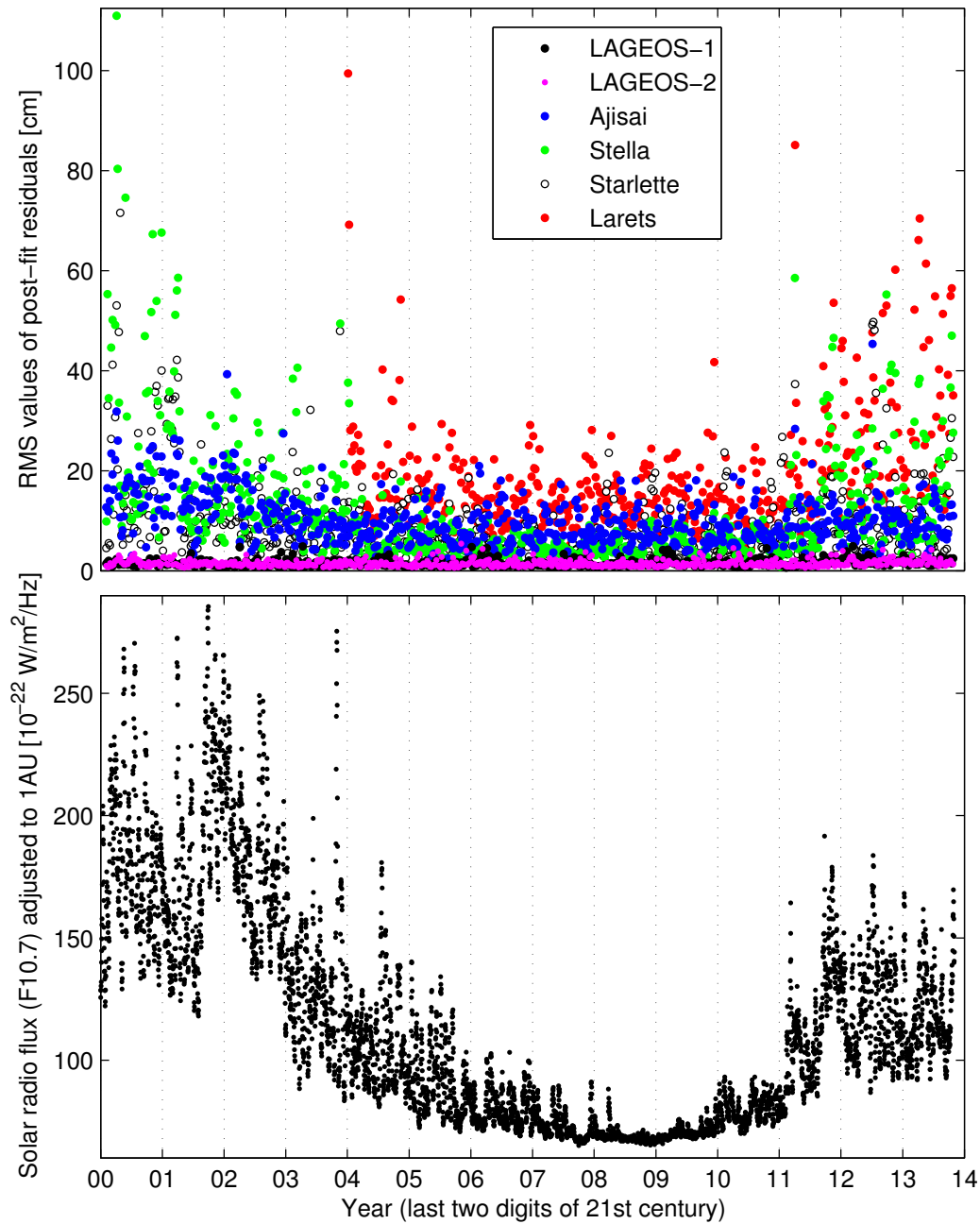


Figure 4.6: Top: RMS values of the post-fit residuals per arc and satellite from January 2000 to October 2013 (the time series of Larets starts in January 2004). The values are smallest for the LAGEOS satellites at ~ 6000 km altitude (cf. Table 4.1). Bottom: 10.7-cm solar radio flux (F10.7) adjusted to 1 AU. The residuals of the low-altitude satellites (Stella, Starlette, Larets) seem to be correlated with the solar activity.

Another indication of the orbital precision provide the so-called orbit connecting points. The RMS values of the differences in orbit connecting points show a similar behavior as the RMS values of the post-fit residuals: they are smallest for the LAGEOS satellites and – concerning the lower satellites – larger at the beginning and at the end of the ~ 14 -year time span (not shown here). The RMS values of orbit connecting points averaged over the investigated time span are given in Table 4.5. The significance of the orbit connecting points is of course limited as successive arcs are connected by only one point. Nonetheless, the tendency of the residuals is clearly reflected in the orbit connecting points (cf. Table 4.5).

Table 4.5: RMS values of post-fit residuals over 7-day arcs from January 2000 to October 2013 and RMS values in total position of orbit connecting points averaged over the investigated time span. The latter indicate the inner precision of the estimated orbits.

Satellite	RMS value [cm] of post-fit residuals	RMS value [cm] of orbit connecting points
LAGEOS-2	1.60	14.09
LAGEOS-1	1.63	19.13
Ajisai	11.46	84.55
Starlette	11.91	100.64
Stella	16.56	130.47
Larets	20.27	170.20

4.3.2 Gravity field

Time-variable gravity field

Monthly sets of gravity field coefficients were estimated and compared with two external solutions, both computed at the Center for Space Research (CSR) at Austin, Texas. One is based on SLR measurements⁷ (Cheng et al., 2011) and one is estimated from Gravity Recovery and Climate Experiment (GRACE) data⁸ (Bettadpur, 2012). For this purpose, the normal equations of all satellites⁹ over one calendar month (three 7-day arcs plus a fourth arc of variable length) were combined and inverted, yielding one

⁷retrieved from ftp://ftp.csr.utexas.edu/pub/slr/degree_2/RL05/

⁸release 05 gravity field solutions; retrieved from <http://isdc.gfz-potsdam.de>

⁹note that Larets was launched at the end of 2003, which is why Larets contributes from January 2004 onwards

set of coefficients per month. To ensure consistency of the time series that shall be compared, the CSR estimates were adjusted as follows: for both the SLR and GRACE time series, the monthly C_{20} coefficients were transferred from the zero-tide system to the tide-free system (Petit and Luzum, 2010, Chapter 6). Further, the monthly average of the atmosphere and ocean de-aliasing product¹⁰ (Flechtner et al., 2014a) was added to the GRACE series. Finally, all spherical harmonic coefficients were scaled to the reference radius of EIGEN-5S (6378.1363 km). Note that there are differences in force modeling between the gravity field solution presented here and those computed by CSR (e.g., a priori gravity field model, ocean tide model, and maximum d/o of ocean tide model), see Cheng et al. (see 2011) and Bettadpur (2012) for more details.

Variations of C_{20} reflect changes in the Earth’s oblateness. Cheng and Tapley (2004) analyzed SLR data over a time span of 28 years (1976 to 2003). They found that the dominant signatures in C_{20} are

1. interannual variations that are related to strong El Niño-Southern Oscillation events,
2. seasonal annual variations (climate related) due to mass redistribution in the atmosphere, ocean, and continental water,
3. a decadal variation due to tidal forcing, and
4. a secular variation that is mainly caused by land uplift due to Post-glacial Rebound (PGR), but has also contributions from the ablation of mountain glaciers and ice sheets, and from changes in water reservoirs.

Seasonal annual variations are clearly visible in the estimated C_{20} time series (cf. Figure 4.7, top) based on SLR data as well as a secular trend. The GRACE-based C_{20} time series reveals unrealistically large amplitudes on the one hand and an offset with respect to the two SLR series on the other hand (cf. Figure 4.7, top). This comparison underpins the superiority of SLR when it comes to the determination of the Earth’s oblateness term. The two solutions based on SLR are in very agreement concerning C_{20} .

In contrast to the C_{20} time series, the GRACE solutions do not show larger amplitudes than the SLR series for order-1 and order-2 terms (cf. Figure 4.7). Variations in C_{21} and S_{21} (cf. Figure 4.7, middle) are caused by mass-induced excitations of polar motion. Besides seasonal variations, these coefficients experience a significant linear trend that is explained by PGR as well as

¹⁰retrieved from <http://isdc.gfz-potsdam.de>

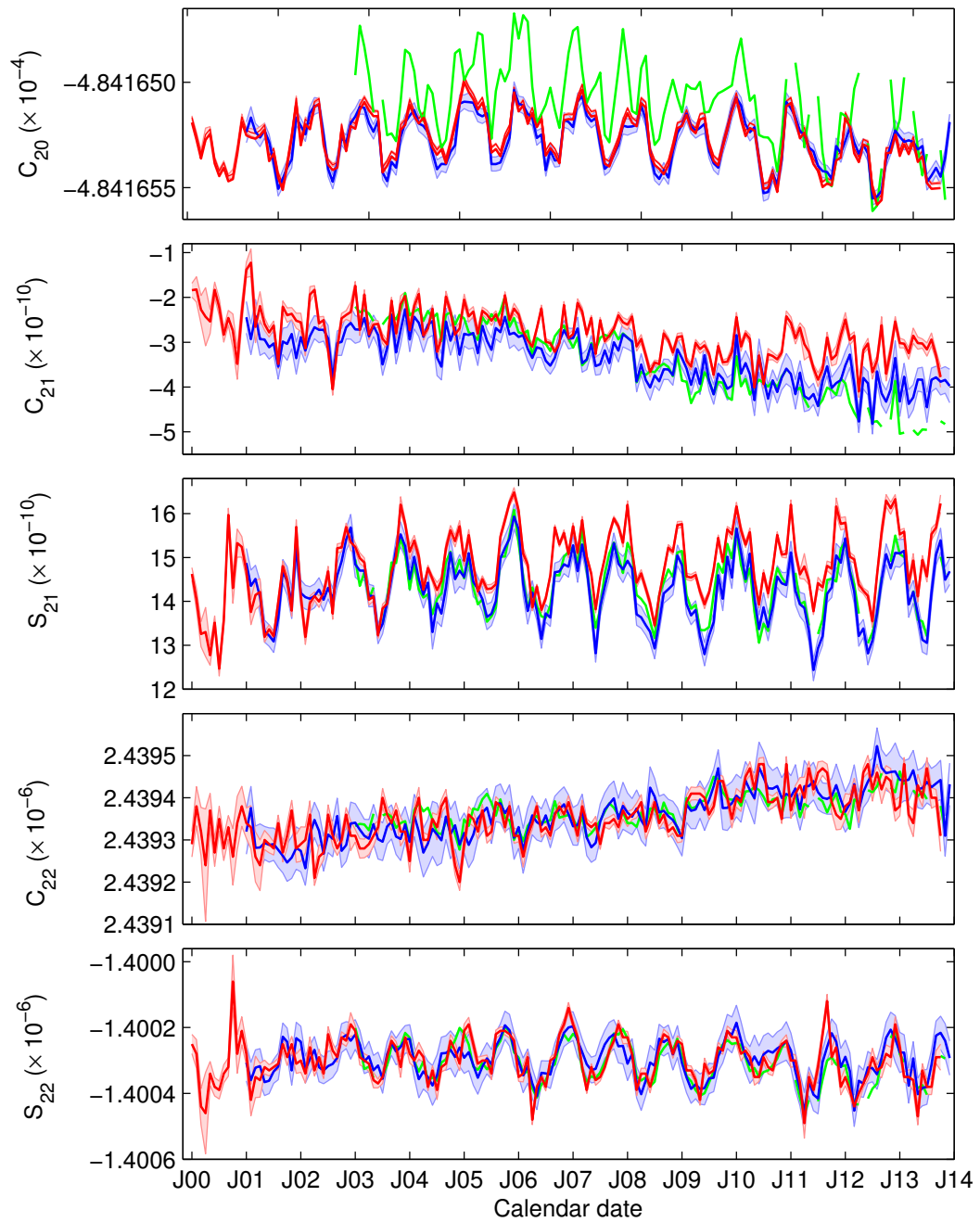


Figure 4.7: Monthly gravity field coefficients of degree 2. Red and light red: estimated coefficients and formal errors. Blue and light blue: SLR-based coefficients by CSR and formal errors (data are available from January 2001). Green: GRACE-based estimates by CSR (data are available from January 2003; gaps: June 2003, January 2011, June 2011, May 2011, October 2012, March 2013, August 2013, September 2013).

present-day mass changes of glaciers and ice sheets (Cheng et al., 2011). The sectorial coefficients of degree two, C_{22} and S_{22} (Figure 4.7, bottom), reflect the ellipticity of the equator and are characterized by mainly seasonal fluctuations. From all coefficients shown in Figure 4.7, the agreement of the C_{21} and C_{22} time series is smallest which might be attributed to the weaker seasonal variability of those coefficients (Chen et al., 2000).

Static gravity field

For the computation of the static gravity field solution, SLR data to all six satellites over the ~ 14 -year time span were analyzed in a joint least-squares adjustment; the normal equation systems of all 7-day arcs and all satellites were stacked. The resulting coefficients represent averaged values (in terms of least squares) over the considered time span. The degree-wise error amplitudes of the static solution are approximately one order of magnitude smaller than those of the monthly estimates (cf Figure 4.8); the error decreases with the square root of the number of stacked normal equations. Note that especially for the degree-2 coefficients the error amplitudes of the static solution are considerably smaller than those of the adopted a priori gravity field model EIGEN-5S (a combination solution of GRACE and 14 years of LAGEOS data). This improvement might be due to the analysis of six geodetic satellites instead of two in case of EIGEN-5S.

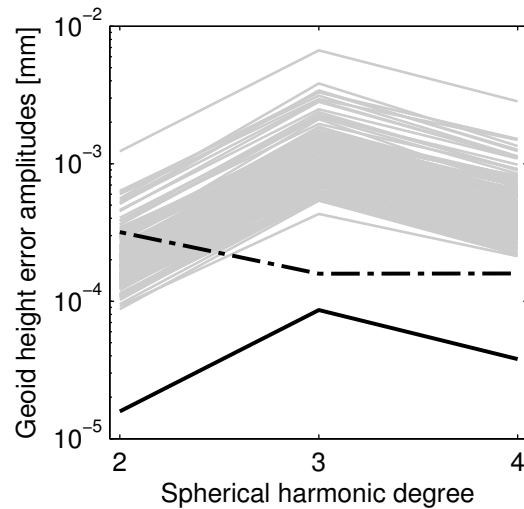


Figure 4.8: Degree-wise error amplitudes in terms of geoid heights. Grey lines: monthly solutions from SLR data; solid black line: static (averaged) solution from SLR data; dashed black line: EIGEN-5S.

4.4 Discussion and conclusions

The RMS values of the post-fit residuals are significantly larger than the measurement precision (1-3 mm). Whereas the residuals of the observations to the LAGEOS satellites do not show a systematic pattern, those of the lower satellites actually do. The applied atmospheric density model, MSIS-86, seems to insufficiently model the densities at times of pronounced solar activity. Even though the new release NRLMSISE-00 might lead to slightly better results, the fluctuations of the atmospheric density remain unpredictable to a large extent (cf. Section 2.1.2). Aside from the systematic patterns due to these fluctuations, the level of residuals (see Figure 4.6, top) is smaller for satellites of high altitude (e.g., LAGEOS) than for lower orbiting satellites (e.g., Stella and Starlette). This behavior can be explained by the perturbing factor of the atmosphere, which increases with decreasing altitude. A further shortcoming might come from the fact that the center of mass corrections were treated as constant values (cf. Table 4.3). Sośnica et al. (2012) showed, however, that Ajisai's center of mass correction, for instance, varies up to 45 mm between different stations.

Simulations over a time span of one year to five geodetic satellites (see Maier et al., 2012, for details) have shown that it is not feasible to estimate gravity field coefficients higher than about d/o 5. The case is different if SLR data are combined on the normal equation level with other satellite data to compute a combined gravity field model (e.g. GOCO models). Then, the resolution could be increased.

The offset in the C_{20} temporal variations of the GRACE-based solution as well as the less pronounced annual signature compared to the SLR-based solutions (cf. Figure 4.7, top) demonstrate that SLR is better suited than GRACE (or any other to date realized space gravimetry mission) to determine the Earth's dynamical oblateness (C_{20}). The reason for the larger amplitudes of the GRACE-based estimates is that they are affected by errors in the applied diurnal-semidiurnal ocean tide model (e.g. Chen et al., 2009; Lavallée et al., 2010). It should be emphasized that C_{20} is the most important gravity field parameter as it has the largest absolute value in the spherical harmonic expansion. As far as the temporal variations of the degree-2 terms are concerned, SLR is able to detect both seasonal changes and secular variations on (and near to) the Earth's surface. The quality of the non-zonal coefficients of degree 2 is similar for SLR and GRACE. Beyond degree two, the benefit of SLR over GRACE becomes less pronounced (not shown see, see e.g. Sośnica et al. (2014)). Since GRACE might be decommissioned at

any time, SLR is likely to gain more emphasis in future gravity field research – at least until the GRACE follow-on mission (Flechtner et al., 2014b) is operational.

The temporal variations of the coefficients of degree 2 agree very well with the SLR-based estimates by CSR. The monthly time series of degree 2 can be retrieved from <http://geodesy.iwf.oeaw.ac.at/>.

Chapter 5

The Lunar Reconnaissance Orbiter

National Aeronautics and Space Administration (NASA)'s Lunar Reconnaissance Orbiter (LRO) project NASA (cf. Figure 5.1) is the first mission in the framework of the Lunar Precursor Robotic Program (LPRP). This program shall support the return of the United States (US) to the moon by executing lunar robotic missions to conduct research and prepare for future human exploration. LRO's main objectives being aligned with this vision include global mapping of the lunar surface, acquisition of topography, radi-



Figure 5.1: Artist concept of the Lunar Reconnaissance Orbiter (©NASA). The dimension of the main spacecraft bus is approximately $1.3 \times 1.4 \times 2.2$ m. Several scientific instruments are attached to the bus along with a single solar array and a high gain antenna.

ation characterization, and water ice identification. The Lunar Orbiter Laser Altimeter (LOLA) is one of seven instruments aboard LRO (see Chin et al., 2007, for a description of the instruments). LOLA determines the shape of the Moon by measuring the range from the spacecraft to the lunar surface using five beams with a nominal accuracy of 10 cm (Smith et al., 2010). To take maximum advantage of LOLA’s precision the radial component of the orbit of LRO must be reconstructed to the sub-meter-level (Zuber et al., 2010).

LRO, a 3-axis stabilized spacecraft, was launched in June 2009. A one-year nominal mission phase was followed by a two-year science mission phase, and an extended science mission phase (cf. Table 5.1). To meet the mission objectives, LRO was orbiting the Moon in a polar (for total coverage), near-circular (for collecting almost uniform science data), and low altitude orbit (for high-resolution mapping of the topography) for about two years¹ (cf. Table 5.2). These two years are also referred to as the polar mapping phase. One full mapping cycle is completed within 27.4 days. In December 2011, LRO was moved to a quasi-frozen orbit² at an eccentricity of 0.043, or a $\sim 30 \times 216$ km altitude orbit (Beckman, 2006; Keller et al., 2014).

Table 5.1: LRO mission phases

Launch	Jun 18, 2009
Cruise	Jun 18, 2009 to Jun 23, 2009
Lunar orbit acquisition	Jun 23, 2009
Commissioning	Jun 23, 2009 to Sep 14, 2009
Nominal mission	Sep 15, 2009 to Sep 15, 2010
Science mission	Sep 16, 2010 to Sep 15, 2012
First extended science mission	Sep 16, 2012 to Sep 15, 2014
Second extended science mission	since Sep 16, 2014

At an altitude of 50 km, the non-spherical lunar gravitational potential is the dominant perturbing factor. It causes a variation of the eccentricity and of the argument of periapsis (Beckman, 2006). Due to the changes in eccentricity, orbital altitude varies. If left uncorrected, LRO would impact the Moon after about 60 days (Houghton et al., 2007). Since the altitude of 50 km shall

¹entire nominal mission phase and the first year of the science mission phase

²a quasi-frozen orbit is an orbit for which the parameters have been selected to bound one or more orbital elements in the presence of perturbations (Beckman, 2006); for LRO, the eccentricity and the argument of perigee were bounded

Table 5.2: Orbital characteristics during LRO’s polar mapping phase

Orbital period	113 min
Inclination	90° w.r.t. the lunar equator
Eccentricity	~0
Altitude	50 km (± 20 km)

be maintained within ± 20 km, the eccentricity has to be bounded by Station Keeping (SK) maneuvers. Every lunar orbit period, i.e. every 27.4 days, SK is performed while the Earth is in full view of the spacecraft (cf. Figure 5.2). In the course of these maneuvers, eccentricity and argument of periapsis are reset to their initial values. SK is accomplished with two-step burns being performed approximately three hours apart (see Appendix C.1 for a list of maneuvers). Apart from SK, delta-H (dH) maneuvers are performed once a month: LRO fires its thrusters to desaturate the momentum wheels, which absorb angular momentum caused by disturbing torques acting on the spacecraft. Unlike the orbit of the polar mapping phase (cf. Table 5.2), the quasi-frozen orbit to which the spacecraft moved in late 2011, can be maintained for many months without any SK maneuvers (cf. Table C.1); the periselene is located near the lunar south pole (Beckman, 2006). According to Keller et al. (2014), LRO has enough fuel onboard to maintain this quasi-frozen orbit for another 11 years.

LRO is in full sunlight twice a year for about one month (cf. Figure 5.2). During these periods, the solar beta angle³ varies between $\pm 76.4^\circ$ and $\pm 90^\circ$. During the rest of the year the spacecraft experiences eclipses of up to 48 minutes during each orbit (Beckman, 2006; Houghton et al., 2007); the maximum eclipse duration occurs at zero solar beta angle. LRO’s single Solar Array (SA) is mounted on the -Y face of the spacecraft bus frame (cf. Figure 5.16). As the sunlight comes from the opposite direction every six months, LRO performs a yaw flip maneuver twice a year (cf. Appendix C.1 for the dates of the maneuvers). Figure 5.3 illustrates the variation of the solar beta angle from September 1, 2010 to September 1, 2011.

³the solar beta angle is the angle between the orbital plane and the Sun

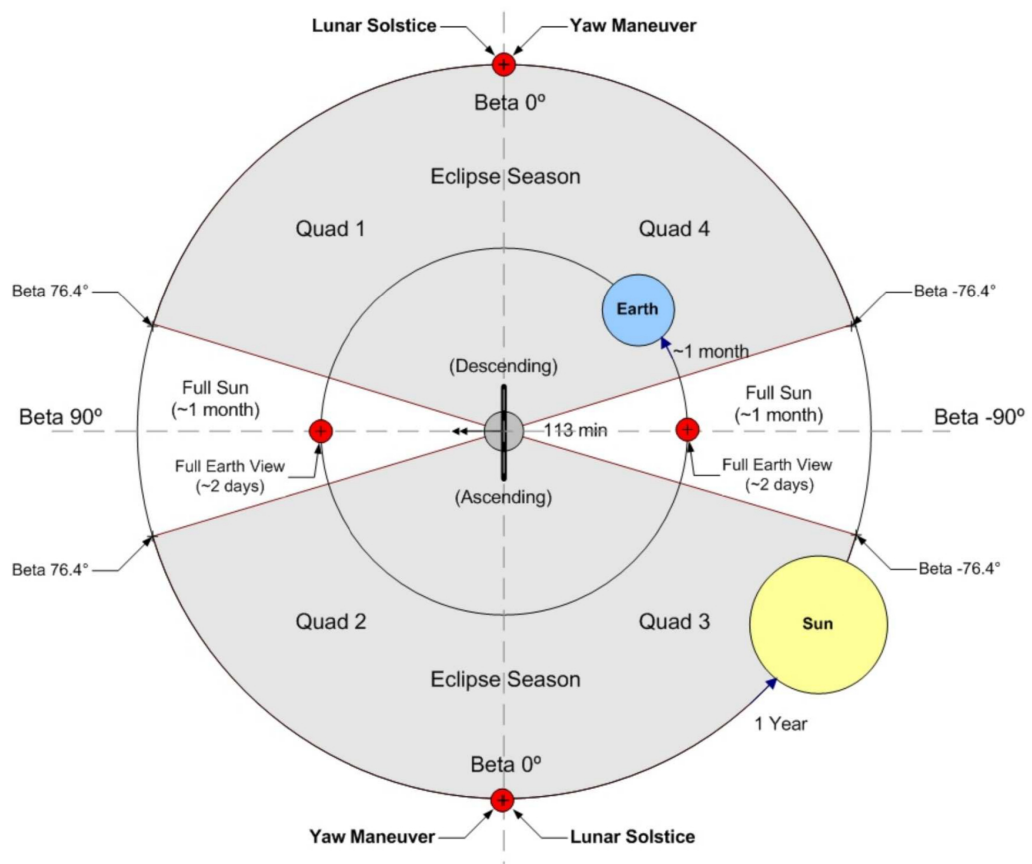


Figure 5.2: Earth and Sun from LRO's perspective (from Saylor et al., 2009).

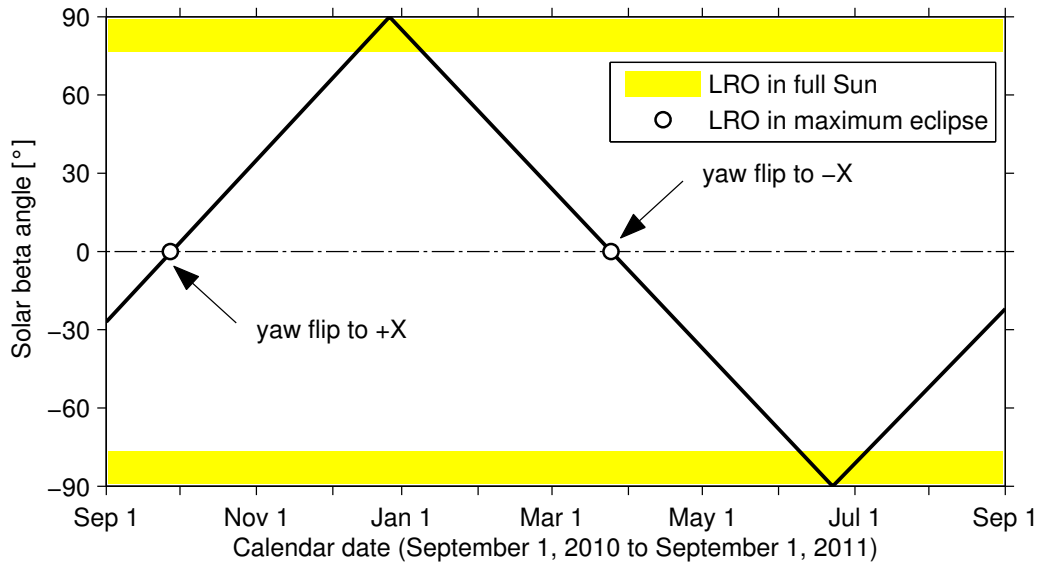


Figure 5.3: Variation of the solar beta angle from September 1, 2010 to September 1, 2011. Whenever the solar beta angle becomes zero, a yaw flip maneuver is performed to keep the Sun on the spacecraft side where the solar array is mounted. LRO starts terminator crossing at $\pm 76.4^\circ$.

5.1 Tracking data

In the sequel, one-way optical laser ranges and two-way Doppler range-rates to the LRO spacecraft are discussed. Radiometric ranges are not addressed as they were not considered for Precise Orbit Determination (POD) of LRO. The conversion from raw observational files to the GEODYN-specific format is subject of Appendix D.

5.1.1 Optical laser ranges

One of LOLA's five detectors supports both incoming signals from the Earth and the signals reflected from the lunar surface (McGarry et al., 2008). Ground stations controlling their laser fires to ensure that the pulses arrive when the LOLA Earth Window is open are referred to as synchronous stations (GO1L, HERL, ZIML). All other stations fire their lasers asynchronously to LOLA (e.g. *ibid.*). The receiver telescope mounted on the High Gain Antenna (HGA) has a wide field of view making simultaneous ranging from multiple stations to LRO possible. Simultaneous ranging can be used, for instance, to compare the ground station times, which is also known as time transfer (Sun et al., 2013). Simultaneous ranging from three

stations can, in principle, provide a geometric solution of the spacecraft position.

The processing of single laser pulses is based on the following steps: each laser pulse emitted from a ground station has to be paired with the corresponding laser pulse received by LRO. To achieve this, a time-of-flight is computed for each emitted pulse based on the station's position, Earth orientation, the LRO ephemeris provided by Goddard Space Flight Center (GSFC)'s Flight Dynamics Facility (FDF) (McGarry et al., 2013; Mao et al., 2013). After accounting for this computed time-of-flight, a low-degree polynomial is used to model the differences between reception and emittance time of the laser pulses (differences are mainly caused by orbit errors) (McGarry et al., 2013; Mao et al., 2013). To increase the measurement precision, 5-second Normal Points (NPs) are formed from the full-rate data according to the International Laser Ranging Service (ILRS) NP algorithm by Sinclair (1997). NPs to LRO have a nominal precision of 10 cm (Smith et al., 2008), which is significantly higher compared to radiometric ranges (10 m, Morinelli et al., 2010). The NPs, which are given in the Consolidated Laser Ranging Data Format (CRD) format, were downloaded from http://pds-geosciences.wustl.edu/lro/lro-1-rss-1-tracking-v1/lrors_0001/data/range/npt/.

The involvement of two non-synchronous clocks in the laser ranging observations (cf. Equation 2.51) imposes a major challenge to the processing of those data (see Figure 5.4 for an example). Whereas the ground stations time-tag the outgoing pulses using highly stable clocks such as Maser or Cesium clocks, the LRO clock suffers from a constant time offset, a linear time drift, a quadratic frequency aging, and a cubic frequency aging rate (Mao et al., 2014). Note that the clock correction term implemented in GEODYN (cf. Equation 2.54) does not contain a cubic term.

NASA's Next Generation Satellite Laser Ranging (NGSLR) station is the primary station performing laser ranging measurements to LRO. In addition, the ILRS network (Pearlman et al., 2002) participates in tracking. All stations performing laser ranges to LRO are given in Table 5.3. The number of observations per tracking station is shown in Figure 5.5. The primary station naturally observes the major part, followed by the ILRS stations YARL and MDOL.

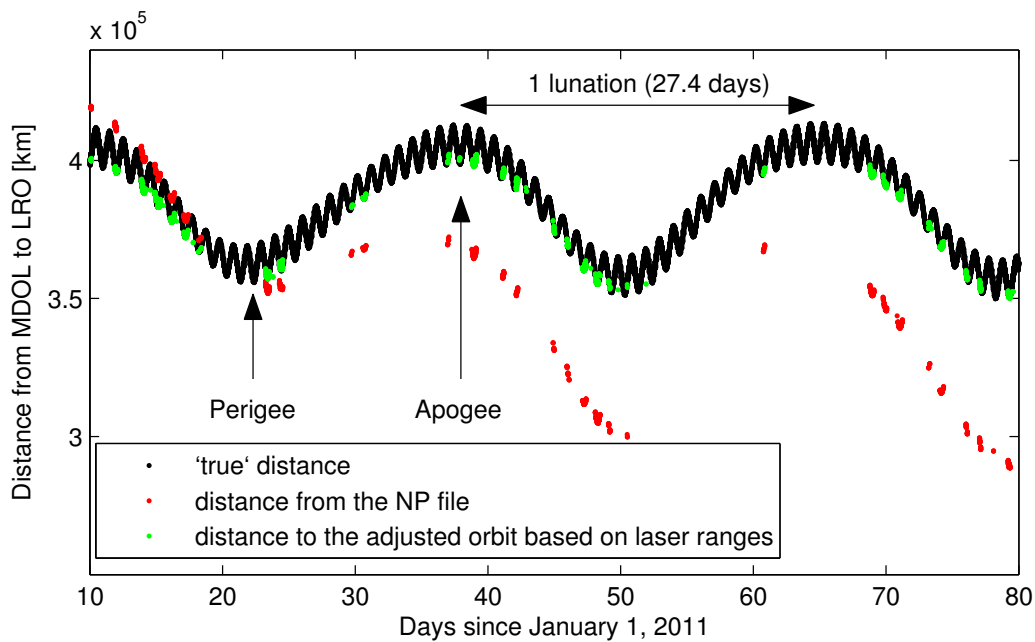


Figure 5.4: The ‘true’ distance between McDonalds, Texas, and LRO (black color) was computed based on the science orbits, which are available at <http://imbrium.mit.edu/LRORS/DATA/SPK/> in the SPICE container format (cf. Appendix E). Since LRO was orbiting the Moon at only 50 km above the lunar surface for the time span shown above, the distance between the Earth and LRO is roughly the same as the distance between the Earth and the Moon (varying between $\sim 360\,000$ km at perigee and $\sim 400\,000$ km at apogee). Further, the one-way runtime measurements of the laser signal emitted from McDonalds, which are given in the NP files, were converted to one-way distances (red color). The non-synchronous clocks at the ground station and at the spacecraft impose a bias and a drift to the range measurements. The estimation of LRO clock parameters during the orbit determination procedure based on laser ranges corrects the observed distances to realistic values (green color).

Table 5.3: Stations performing laser ranging measurements to LRO. NASA's Next Generation Satellite Laser Ranging station is designated GO1L.

Code	ID	Location
MDOL	7080	McDonalds, Texas, USA
YARL	7090	Yarragadee, Australia
GODL	7105	Greenbelt, Maryland, USA
MONL	7110	Monument Peak, California, USA
GO1L	7125	Greenbelt, Maryland, USA
HARL	7501	Hartebeesthoek, South Africa
ZIML	7810	Zimmerwald, Switzerland
HERL	7840	Herstmonceux, United Kingdom
GRSM	7845	Grasse, France
WETL	8834	Wetzell, Germany

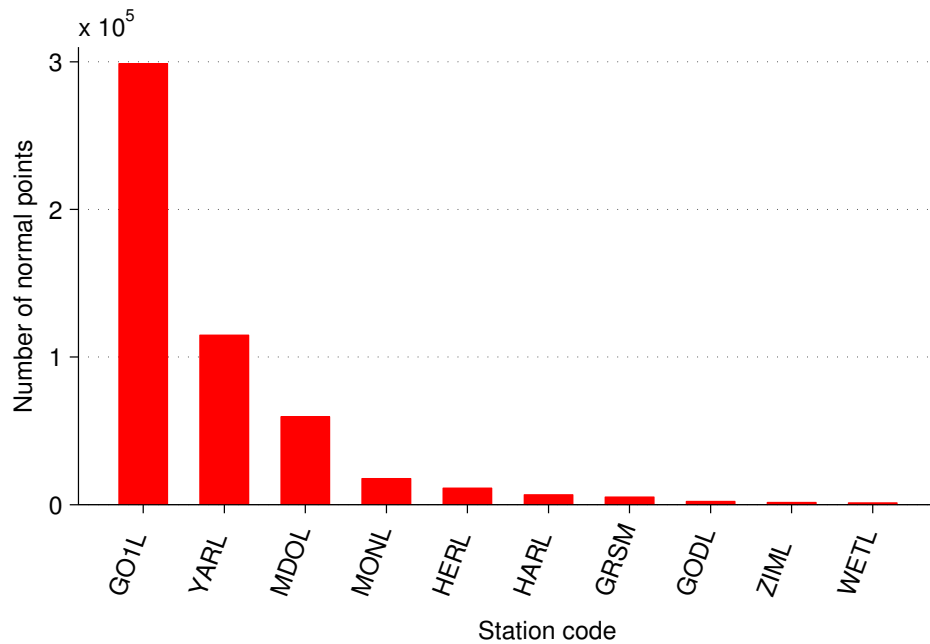


Figure 5.5: Number of NPs per station for the one-year nominal mission phase.

5.1.2 Doppler range-rates

Processing two-way Doppler range-rates is less complex than processing one-way or three-way measurements⁴ since only one clock is involved. The round-trip light time is smaller than the sampling rate (5 s), having a positive effect on noise (Berman, 1972). S-band tracking to LRO is available for about 20 hours per day (Zuber et al., 2010). The network consists of the NASA White Sands 1 antenna (WS1S), which acts as the primary station, and the Universal Space Network (USN) antennas at South Point (Hawaii), Dongara (Australia), Weilheim (Germany), and Kiruna (Sweden), cf. Table 5.4. Whereas the WS1S antenna system provides Doppler tracking data with a nominal accuracy of ≤ 1 mm/s ($1\text{-}\sigma$), the USN antenna system provides data with accuracy of ≤ 3 mm/s ($1\text{-}\sigma$), see Morinelli et al. (2010).

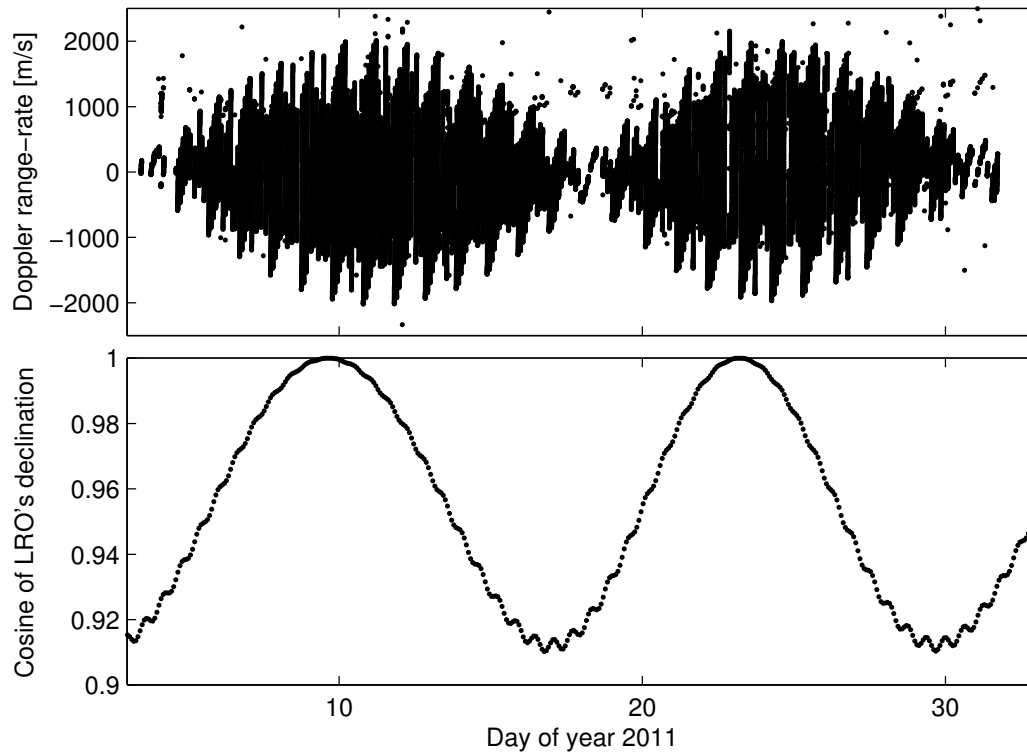


Figure 5.6: Observed Doppler range-rates during a time span of ~ 30 days (top). The magnitude depends on the cosine of LRO's declination (bottom).

Figure 5.6 (top) depicts the overall pattern of range-rates over a time span of about 30 days. The amplitude of the sinusoidal Doppler measurements

⁴in case of three-way measurements the emitting and receiving ground station is not the same

Table 5.4: Stations performing Doppler range-rate measurements to LRO.

Code	ID	Location
WS1S	119	White Sands, New Mexico, US
USPS	103	Dongara, Australia
USHS	105	South Point, Hawaii, US
KU1S	126	Kiruna, Sweden
KU2S	127	Kiruna, Sweden (back-up)
WU1S	128	Wilhelm, Germany
WU2S	128	Wilhelm, Germany (back-up)

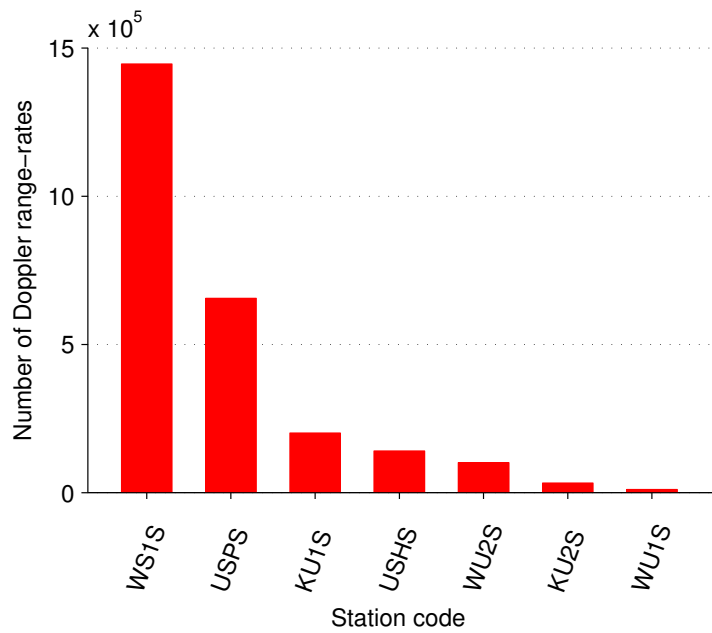


Figure 5.7: Number of Doppler range-rates per station for the one-year nominal mission phase.

is proportional to the cosine of the spacecraft's declination⁵ (cf. Figure 5.6, bottom); its phase varies with the time of day (Doody, 2009). The range-rate, i.e. the relative velocity between LRO and the ground station, is zero when the distance between the two is at its minimum (or maximum). The number of range-rates per station for the nominal mission phase is shown in Figure 5.7.

Figure 5.8 shows the number of Doppler range-rates to LRO during the nominal mission phase on top of the lunar surface. On the nearside of the Moon, observations are densest near the lunar equator. The farside data gap is easy to identify.

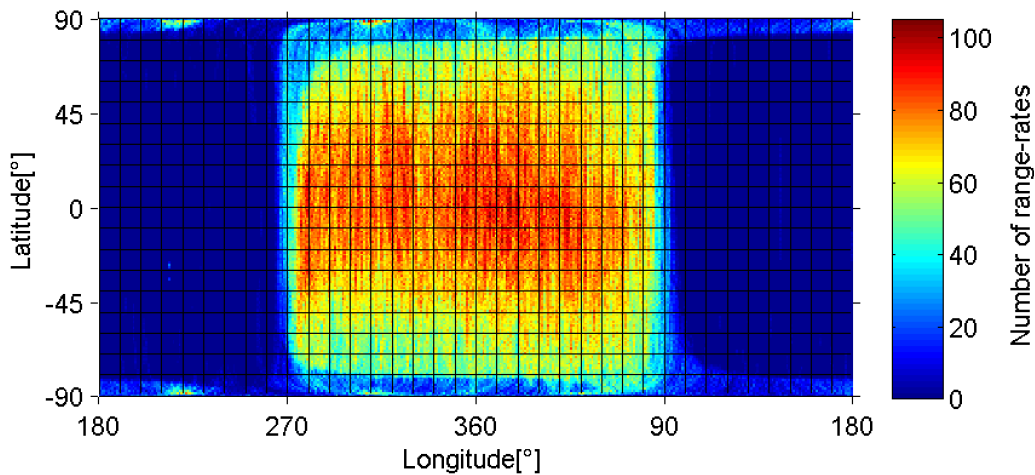


Figure 5.8: Total number of Doppler range-rates to LRO during the nominal mission phase, averaged over a $1^\circ \times 1^\circ$ grid. The western limb of the Moon as seen from the Earth is located at 270° .

To get an idea of the temporal distribution of laser ranges and Doppler range-rates, it is instructive to visualize the time of observation for each tracking station (Figure 5.9). Tracking of LRO via optical laser ranges (cf. Figure 5.9, top) is not continuous and there exist several gaps. The availability of Doppler data, in contrast, is continuous (cf. Figure 5.9, bottom).

⁵measured from the equatorial plane to the line connecting the geocenter with the spacecraft

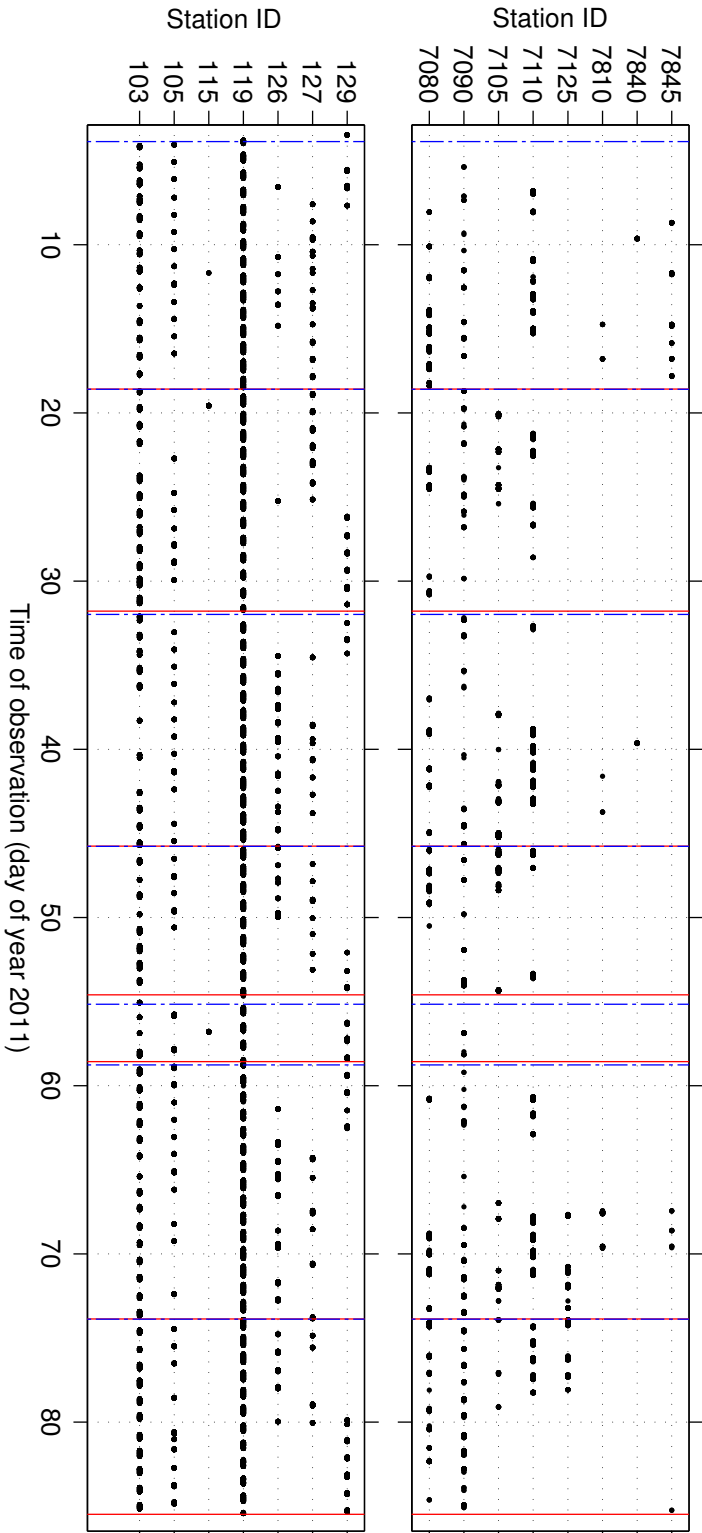


Figure 5.9: Time of observed laser ranges (top) vs. time of observed Doppler range-rates (bottom) per tracking station over a time span of 90 days (SM05 to SM07). Whereas laser tracking is sparse from time to time, the station White Sands (119) tracks LRO via Doppler range-rates whenever light-of-sight between tracking station and satellite is given. Blue and red lines indicate start and stop times of LRO's science orbits, respectively. These orbits are provided with small gaps due to performed maneuvers (see Appendix C.1 for more details).

5.2 Simulation study

A series of simulation studies has been conducted to (1) gauge the relative performance of the measurement types, (2) investigate the impact of the farside data gap on the recovery of the lunar gravity field, and (3) analyze the effect of spectral leakage.

5.2.1 Setup

Over a time span of about 100 days (January 14, 2010 to May 2, 2010), optical laser ranges and Doppler range-rates were simulated for three stations (cf. Table 5.5). The considered stations observed 82% of all laser ranges and 90% of all range-rates made during the one-year nominal mission phase. Two spatial coverage modes were considered to demonstrate the difficulty concerning POD of satellites orbiting the Moon. The first mode (referred to as ‘even coverage’) generates observations on the nearside and on the farside of the Moon. The even coverage mode is only of theoretical interest as it assumes globally available direct tracking data. The second mode (referred to as ‘uneven coverage’) represents the real case: laser ranges and Doppler data were only generated on the nearside of the Moon. Since real tracking data to LRO were already available when this simulation study was conducted, observations were simulated for the exact time spans when the stations tracked the spacecraft. The number of simulated observations for the even and uneven coverage mode is given in Table 5.6.

Table 5.5: Settings for the simulation of one-way laser ranges and two-way range-rates (cf. Tables 5.3 and 5.4 for a description of the station code).

	Laser ranges	Doppler range-rates
Station code	GO1L YARL MDOL	WS1S USPS KU1S
Elevation cut-off angle	20°	10°
Bin size/count interval	5 s	5 s
Coverage mode	even/uneven	even/uneven
Noise level	10 cm	1 mm/s

For the purpose of simulation studies it is sufficient that the simulated LRO trajectory reflects the overall characteristics of the true trajectory. Hence, the only perturbation taken into account was the lunar gravity field. JGL165P1

Table 5.6: Number of simulated observations for a time span of ~ 100 days.

Coverage mode	Number of laser ranges	Number of Doppler range-rates
even	629 000 (YARL)	718 000 (USPS)
	609 000 (MDOL)	700 000 (WS1S)
	568 000 (GO1L)	590 000 (KU1S)
	$\Sigma=1\,806\,000$	$\Sigma=2\,008\,000$
uneven	64 000 (GO1L)	371 000 (WS1S)
	46 000 (YARL)	147 000 (USPS)
	23 000 (MDOL)	50 000 (KU1S)
	$\Sigma=133\,000$	$\Sigma=568\,000$

(Konopliv et al., 2001), truncated at degree and order (d/o) 100, served as the ‘true’ model for tracking data simulation. The simulated observations were superposed with white Gaussian noise of zero mean. For laser ranges and Doppler range-rates a noise level of 10 cm and 1 mm/s has been introduced, respectively (cf. Table 5.5), since these are the nominal precisions for laser ranges and Doppler measurements from the primary station. The initial state vector was obtained from the science orbits by using the SPICE toolkit within the MATLAB environment (cf. Appendix E).

For the recovery of the orbit (and the estimation of gravity field coefficients) by means of simulated observations, a $1\text{-}\sigma$ clone of JGL165P1 (up to d/o 100) served as a priori gravity field model (cf. Table 5.7). Gravity field coefficients were estimated up to d/o 5, 12, and 16 taking gravity field omission errors into account. Again, the initial state vector was obtained from the science orbits. The typical arc length was about two weeks since this is the time span not interrupted by maneuvers (cf. Appendix C.1). More information about the simulation settings are given in Table 5.5.

Table 5.7: Standards used for POD and gravity field recovery based on simulated tracking data to LRO.

	Standard/model	Reference
<i>Reference frame</i>		
Inertial reference system	ICRF	McCarthy and Petit (2004)
EOPs	IERS 08 C04	Bizouard and Gambis (2007)
Planetary ephemeris	JPL DE-421	Folkner et al. (2009)
Precession-nutation model	IAU-2000	Capitaine et al. (2003)
Station coordinates	NGSLR: retrieved from the PDS ⁶ YARL, MDOL: SLRF2008 WS1S, USPS, KU1S: retrieved from the PDS ⁶	Pavlis (2009)
<i>Gravitational force model</i>		
Gravity field model	1- σ clone of JGL165P1 (up to d/o 100)	Konopliv et al. (2001)

5.2.2 Results

Observations were simulated by declaring JGL165P1 the ‘true’ gravity field model. Hence, the differences between the ‘true’ orbit and the estimated orbit can be used as an indicator of the quality of the recovered orbit. Figure 5.10 depicts the Root Mean Square (RMS) values of those differences for each arc in the along-track component of the spacecraft reference frame. If direct tracking data were available over the farside, the three observational cases (laser ranges, Doppler range-rates, laser ranges and Doppler range-rates) would produce orbits of about the same quality (Figure 5.10, top) as there are approximately as many laser ranges as Doppler range-rates available (cf. Table 5.6). The result is different in case of uneven coverage (Figure 5.10, bottom): despite of the larger number of Doppler observations (cf. Table 5.6), laser ranging outperforms Doppler due to its high precision. The RMS values of the orbit differences over all arcs (cf. Table 5.8) reveal that the best agreement between ‘true’ and recovered orbit in total position is achieved using both laser ranges and Doppler range-rates. The result is only marginally worse if the orbit is recovered solely from laser ranges.

⁶http://pds.nasa.gov/ds-view/pds/viewInstrumentProfile.jsp?INSTRUMENT_ID=RSS&INSTRUMENT_HOST_ID=LRO

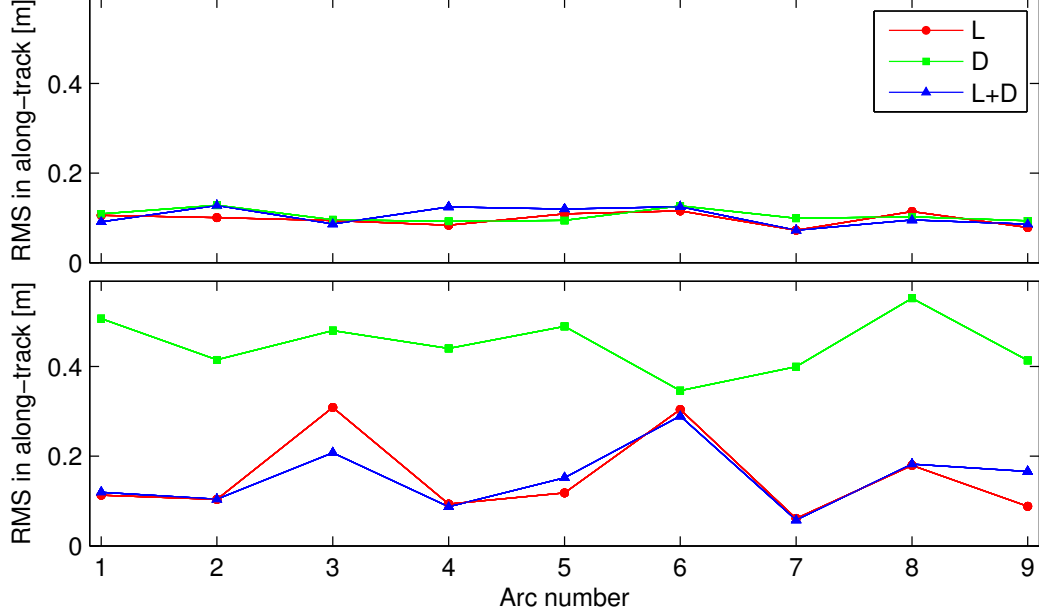


Figure 5.10: RMS values of orbit differences between ‘true’ and estimated orbit in along track direction. RMS values are given for the even coverage mode (top) and the uneven coverage mode (bottom). The orbit was estimated based on laser ranges (‘L’), on Doppler range-rates (‘D’), and on laser ranges and Doppler range-rates (‘L+D’).

Table 5.8: RMS values of the differences between ‘true’ and recovered orbit in along track, cross track, and radial direction as well as in total position. The orbit was computed from laser ranges (‘L’), from Doppler range-rates (‘D’), and from laser ranges and Doppler range-rates (‘L+D’) for the uneven coverage mode.

Observational case	RMS [m]			
	along track	cross track	radial	total
L	0.168	0.124	0.154	0.260
D	0.465	0.211	0.459	0.686
L+D	0.160	0.130	0.157	0.258

After having compared the orbits obtained for the three observational cases, the results can also be analyzed at the level of gravity field coefficients. One possibility is to interpret the estimated parameters in terms of selenoid heights. In case coefficients are estimated up to d/o 5 (Figure 5.11, column 1), the difference is well below ± 0.5 m for all observational cases (uneven coverage mode). Estimating coefficients up to d/o 12, however, considerably degrades the results particularly over the farside where no tracking data exist (Figure 5.11, column 2). An even higher d/o of 16 also affects the nearside (Figure 5.11, column 3). Note that the results presented in Figure 5.11 are

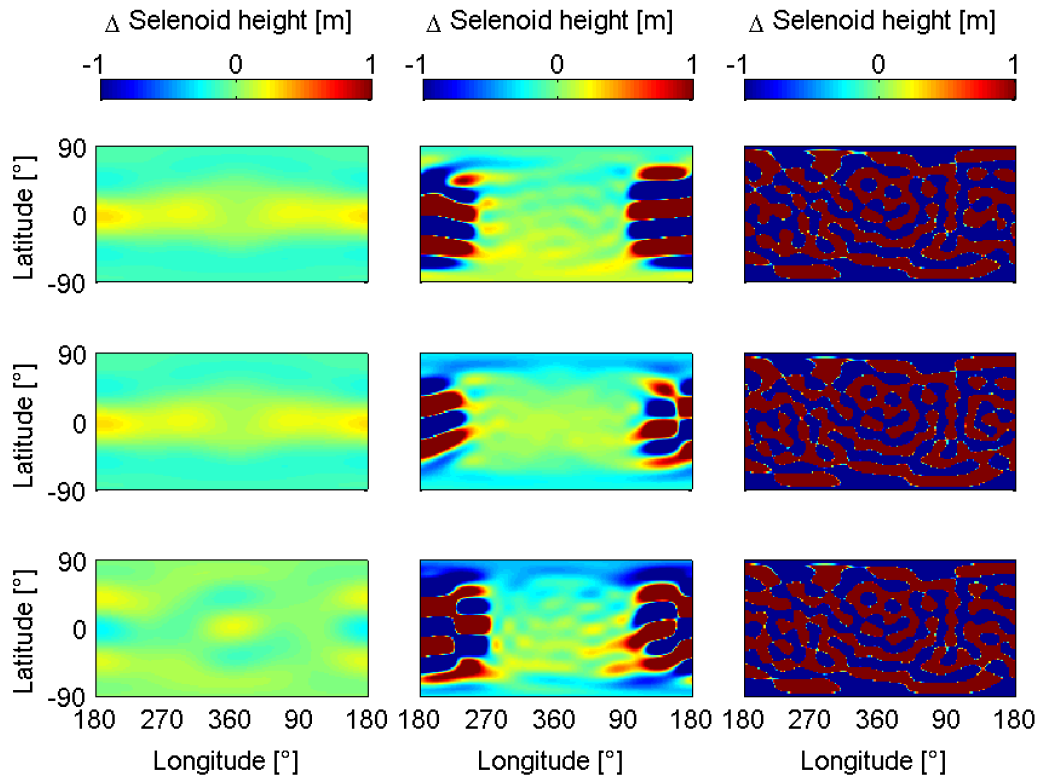


Figure 5.11: Difference in selenoid height between the ‘true’ gravity field model JGL165P1 and the estimated coefficients (uneven coverage mode). Column 1 to 3 corresponds to different maximum d/o of recovered coefficients (5, 12, 16); row 1 to 3 corresponds to the recovery of gravity field information from laser ranges only, from Doppler data only, and from laser ranges and Doppler data. The nearside of the Moon is located between 270° and 90° ; the colorbar has been limited to range from -1 to $+1$ to make a comparison easier. The differences, however, are as large as ± 30 m for d/o 12 and ± 80 m for d/o 16; they are largest at the farside where no tracking data exist.

overpessimistic as spectral leakage is not considered at this point.

Singular Value Decomposition (SVD) is a powerful tool for the analysis of ill-posed problems. The singular values of the normal equations based on Doppler range-rates are shown in Figure 5.12 for maximum d/o 5, 12, and 16. Figure 5.12 substantiates that an increase in the dimension of the normal equation system increases the range of singular values (Floberghagen, 2002, Chapter 4). Whereas the difference between smallest and largest singular value is approximately the same for d/o 5 for the even and uneven coverage mode (Figure 5.12, left), it is significantly larger for the uneven coverage mode concerning d/o 12 and d/o 16 (Figure 5.12, middle and right). From the singular values one can deduce rather large condition numbers⁷; in case of even coverage mode they are 4×10^6 , 7×10^8 , and 3×10^9 for maximum d/o 5, 12, and 16, respectively. For the uneven coverage mode, they are 4×10^6 , 1×10^{11} , and 3×10^{12} for maximum d/o 5, 12, and 16, respectively. The increasing ill-conditioning with increasing degree and order is responsible for the large differences in selenoid heights for d/o 12 and 16 (cf. Figure 5.11). Consequently, it is not possible to estimate gravity field coefficients up to d/o 12 (let alone d/o 16) without regularization.

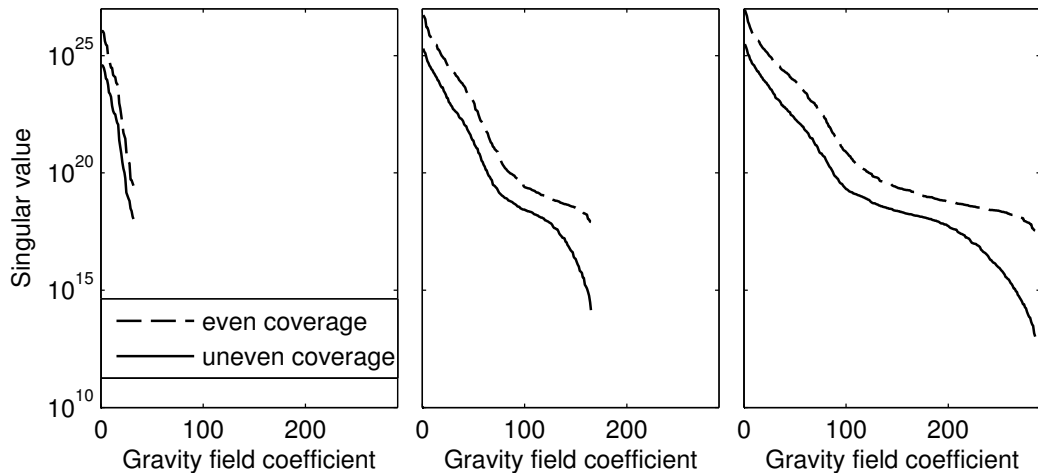


Figure 5.12: Singular values of the normal equation matrix based on Doppler range-rates for the even and uneven coverage mode for maximum degree and order 5 (left), 12 (middle), and 16 (right). The scale of the y-axis is logarithmic.

As stated in the previous paragraph, regularization is inevitable even for a resolution as low as d/o 12. As described in Chapter 3, Tikhonov-Phillips reg-

⁷the condition number is the ratio between largest and smallest singular value

ularization was applied. The L-curve criterion, implemented by Per Christian Hansen and provided as a MATLAB toolbox, was used to find the optimal regularization parameter. An example of the plots that can be generated with this tool is given in Figure 5.13. The normal equations that result from estimating coefficients up to d/o 12 based on laser ranges (uneven coverage) served as input. The L-curve for this particular case is shown in Figure 5.13 (left) on a linear scale since for the specific example the L-shape is less pronounced in the log-log scale. The optimal value for the regularization parameter η corresponds to the maximum curvature of the L-curve (cf. Figure 5.13, right) and amounts to 2.95. By applying Kaula's regularization matrix (Kaula, 1966), scaled by the optimal regularization parameter, to the normal equation system, the regularized gravity field solution is obtained (cf. Section 3).

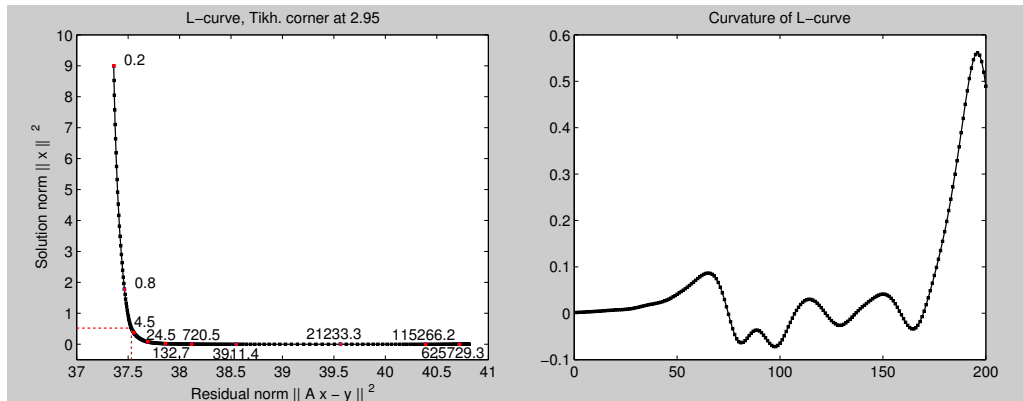


Figure 5.13: Output of the regularization tool by Per Christian Hansen, which finds the optimal regularization parameter by means of the L-curve criterion. The normal equations for estimating gravity field coefficients up to d/o 12 based on laser ranges served as input. (Left) Residual norm vs. solution norm on a linear scale for 200 regularization parameters. (Right) The optimal regularization parameter (2.95) corresponds to the maximum curvature of the L-curve.

Again, the regularized solution is compared with the ‘true’ solution in terms of selenoid height. The large differences concerning the unregularized solution of the uneven coverage mode (Figure 5.14, left), which are as large as ± 25 m over the farside, have been successfully reduced after applying regularization (Figure 5.14, middle); after regularization, the maximum differences are ± 0.5 m. To compare with, the unregularized solution for the even coverage mode is given in Figure 5.14 (right). Mind that for the nearside of the Moon the differences of the regularized solution (uneven coverage mode)

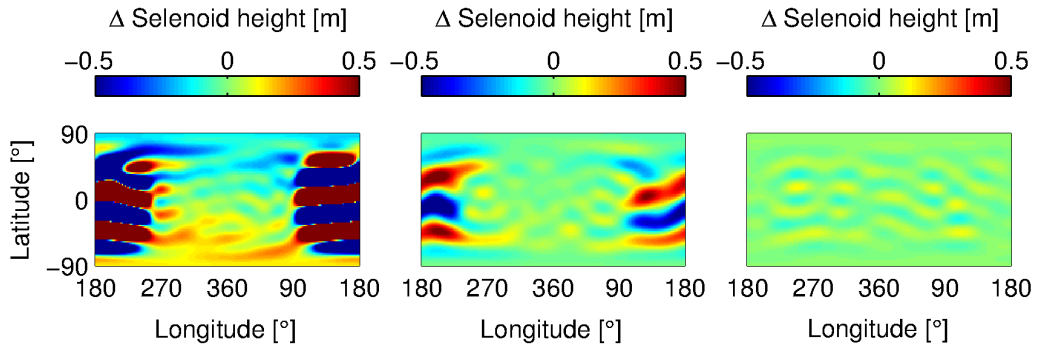


Figure 5.14: Difference in selenoid height between the ‘true’ gravity field model JGL165P1 and the estimated coefficients (maximum d/o 12) based on laser ranges. The nearside of the Moon is located between 270° and 90° . (Left) Unregularized solution of the uneven coverage mode. (Middle) Regularized solution of the uneven coverage mode using Kaula’s regularization; the optimal regularization parameter was determined with the L-curve criterion. (Right) Unregularized solution of the even coverage mode.

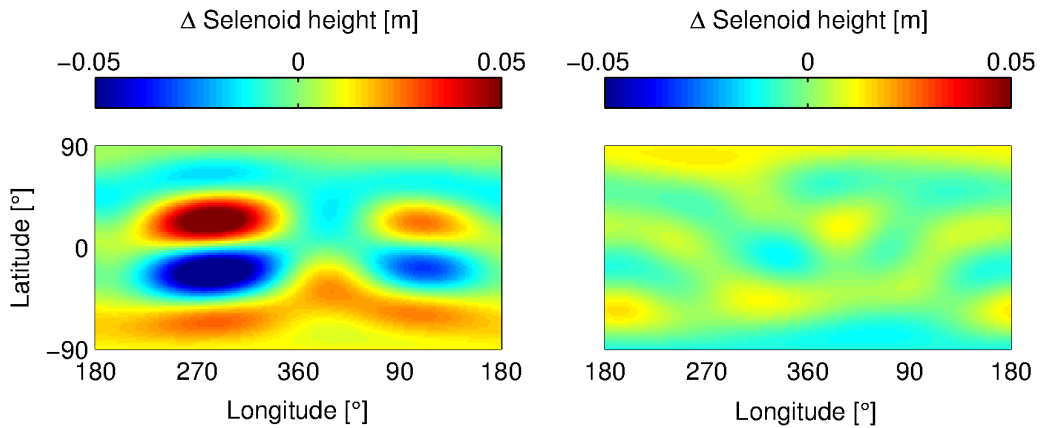


Figure 5.15: Difference in selenoid height between the ‘true’ gravity field model JGL165P1 and the estimated coefficients based on laser ranges. The nearside of the Moon is located between 270° and 90° . Coefficients were estimated based on laser ranges (even coverage mode) up to d/o 5 (left) and 16 (right), whereas all coefficients higher than d/o 5 were disregarded.

are similar to those of the unregularized solution (even coverage mode). The slightly better performance of the latter can be explained by the fact that in the even coverage mode observations were simulated whenever line of sight was given between station and satellite. In the uneven coverage mode, however, observations were only simulated when the stations actually tracked the spacecraft.

The simulation studies are perfectly suited to evidence the effect of spectral leakage (cf. Chapter 1). To this end, exemplarily for all three cases, gravity field coefficients were estimated from laser ranges (even coverage mode) up to d/o 5 and d/o 16. From the latter solution, all coefficients larger than d/o 5 were left unconsidered. The comparison of these two solutions is depicted in Figure 5.15. Estimating more coefficients than actually asked for is an effective way to mitigate spectral leakage; the differences could be reduced by about a factor of 5 (cf. Figure 5.15).

5.2.3 Discussion and conclusions

Rowlands et al. (2009) conducted a pre-launch simulation study for LRO and obtained, in accordance with the outcome of the simulation presented here, better results with laser ranges than with Doppler range-rates. This is striking to that effect that the number of Doppler data is a factor of five larger than the number of laser ranges. The high precision of the laser ranging measurements is the reason for the better performing. At this point it shall be stressed, however, that the simulations were kept very simple. The involvement of two non-synchronous clocks in the laser ranging measurements to LRO, which was disregarded for the conducted simulations, makes real data analysis a very challenging task.

To conclude, the simulation studies have shown that

1. the most precise orbits are obtained by evaluating Doppler range-rates as this is the main tracking data type,
2. it is unfeasible to estimate coefficients up to d/o 12 or higher without regularization due to the farside data gap,
3. Tikhonov-Phillips regularization successfully decreases the numerical instability of the normal equation system caused by the farside data gap,

4. it is prudent to estimate more gravity field coefficients than actually asked for to mitigate spectral leakage.

5.3 Precise orbit determination

The gravity field model GL0660B (Konopliv et al., 2013), derived from the Gravity Recovery and Interior Laboratory (GRAIL) mission and computed at the Jet Propulsion Laboratory (JPL), served as a priori gravity field model. To find out a suitable truncation level of the a priori gravity field model due to computational reasons, a simple forward integration was made over a time span of six months using two different truncation levels (maximum d/o 270 and maximum d/o 540). The two orbits were then compared; the RMS values of the differences amount to 0.66 m, 0.55 m, and 0.08 m in along track, cross track, and radial direction, respectively. In total position, the RMS value is 0.86 m. Bearing in mind that LRO's position knowledge requirement was defined as 50-100 m in total position (e.g. Mazarico et al., 2012), truncating the a priori gravity field at d/o 270 seems to be a suitable tradeoff between orbital precision and computing time.

The positions of all planetary bodies were determined by GEODYN using the Planetary and Lunar Ephemeris DE 421 (Folkner et al., 2009). All bodies, except for the Earth, were approximated as point masses. Table 5.9 lists the gravitational parameters used for the computation of third body accelerations. In addition to the approximation of third bodies as point masses, the acceleration of the LRO spacecraft due to the oblateness of the Earth and the Moon is considered (see 2.1.1 for more details).

For a lunar orbiter, GEODYN takes the relativistic Schwarzschild field and the relativistic Coriolis force into account. Regarding the correction of the computed range between station and spacecraft, the software neglects the bending term given in Equation (2.65). According to Moyer (2000), this term is only significant when the transmitter and the receiver are on opposite sides of the Sun which is never the case for LRO. Further, the relativistic light time delay is not computed for all planets as suggested by Moyer (*ibid.*) but only for Jupiter and Saturn whose gravitational parameters are significantly larger than those of the other planets (cf. Table 5.9).

Laser ranging and Doppler measurements refer to the tracking point at the HGA. Consequently, they must be transferred to the center of mass. The antenna offset relative to the satellite's center of figure and the center of

Table 5.9: Gravitational parameters, GM , used for the computation of the acceleration due to the lunar gravity field and due to third body accelerations.

Planetary body	GM [km ³ /s ²]
Mercury	22032.0805 ¹
Venus	324858.5988 ¹
Earth	398600.4415 ²
Earth's Moon	4902.8003 ³
Mars	42828.3744 ⁴
Jupiter	126712767.8578 ¹
Saturn	37940626.0611 ¹
Uranus	5794549.0071 ¹
Neptune	6836534.0639 ¹
Pluto	981.6009 ¹
Sun	132712440017.9870 ¹

¹ Standish et al. (1995)² Petit and Luzum (2010)³ Konopliv et al. (2013)⁴ Konopliv et al. (2006)

mass offset, again relative to the satellite's center of figure, are given in Table 5.10. The center of mass correction, $\Delta\rho_{\text{com}}$ (cf. Section 2.2.2), is obtained by projecting the difference between the antenna offset vector and the center of mass offset vector (this difference is denoted by \mathbf{E} in Figure 2.6) onto the unit vector pointing from the ground station to the tracking point. The dimensional layouts of LRO along with the assumed center of figure and the assumed center of mass can be found in Appendix C.2.

Table 5.10: POD standards for LRO.

	Standard/model	Reference
<i>Reference frame</i>		
Inertial reference system	ICRF	McCarthy and Petit (2004)
EOPs	IERS 08 C04	Bizouard and Gambis (2007)
Planetary ephemeris	JPL DE-421	Folkner et al. (2009)
Precession-nutation model	IAU-2000	Capitaine et al. (2003)
Station coordinates	NGSLR: retrieved from the PDS ⁸	

Continued on next page

⁸http://pds.nasa.gov/ds-view/pds/viewInstrumentProfile.jsp?INSTRUMENT_ID=RSS&INSTRUMENT_HOST_ID=LRO

Table 5.10: (continued)

	Standard/model	Reference
	ILRS stations: SLRF2008 WS1S and USN stations: retrieved from the PDS ⁸	Pavlis (2009)
<i>Gravitational force models</i>		
Gravity field model	GL0660B (up to d/o 270)	Konopliv et al. (2013)
Solid Moon tides	IERS lunar Love number $k_2=0.02405$	McCarthy and Petit (2004) Konopliv et al. (2013)
Third bodies	positions: JPL DE-421, gravitational parameters: see Table 5.9	Folkner et al. (2009)
Oblateness	direct acceleration of LRO due to Earth's oblateness indirect acceleration of the Moon due to Earth's and Moon's oblateness	Moyer (1971)
Relativistic corrections	Schwarzschild, Coriolis	
<i>Non-gravitational force models</i>		
Solar radiation pressure	$G_0=1372.54 \text{ Wm}^{-2}$ at 1 AU, conical shadow model	
Lunar radiation pressure	Albedo and emissivity: DLAM-1 (d/o 15)	Floberghagen et al. (1999)
<i>Satellite parameters</i>		
Macro-model	10-plate macro-model given by area, normal unit vector, specular and diffuse reflectivity (cf. Table 5.11) Orientation of spacecraft bus, HGA, and SA derived from quaternions Mass interpolated from SFF	
<i>Measurement models</i>		
Tropospheric refraction	Hopfield model	Hopfield (1969)
Antenna offset ⁹	$(0.3, -0.3, -2.5)^T$	
Center of mass offset ¹⁰	$(1.35, 0.00, 0.00)^T$	

Continued on next page

⁹coordinates of antenna w.r.t. center of figure in [m]; the values were retrieved from published dimensional layouts (cf. Appendix C.2)

¹⁰coordinates of center of mass w.r.t. the center of figure in [m]; the values were retrieved from published dimensional layouts (cf. Appendix C.2)

Table 5.10: (continued)

	Standard/model	Reference
Relativistic correction	Applied	
Station displacement		
Solid Earth tide loading	IERS	McCarthy and Petit (2004)

The shape of LRO is modeled by a macro-model (cf. Figure 5.16) consisting of ten flat plates; six plates form the spacecraft bus (+X, -X, +Y, -Y, +Z, -Z), two plates the Solar Array (SA+, SA-), and two plates the High Gain Antenna (HGA+, HGA-). The macro-model of LRO can be found in Smith et al. (2008). As described in Section 2.1.2, each plate is characterized by a unit normal vector, $\hat{\mathbf{n}}$, a plate area, A , and specular and diffuse reflectivity coefficients ζ and δ (see Table 5.11).

The orientation of the three components of LRO's macro-model, i.e. spacecraft bus, SA, and HGA, enter Equations (2.32) and (2.42) via $\hat{\mathbf{n}}$. In the SPICE information system (cf. Appendix E), pointing data for LRO are stored within so-called C-kernels¹¹ in terms of transformation matrices relating

- the LRO spacecraft frame to the Moon mean equator and equinox of date (J2000),
- the SA frame to the spacecraft frame, and
- the HGA frame to the spacecraft frame.

Using the SPICE toolkit, these rotation matrices are then converted to unit quaternions¹², made continuous¹³, and written to the GEODYN-specific format for external attitude information. Figure 5.16 illustrates the LRO main spacecraft bus frame along with the SA and HGA frames. No information about the location of the SA and the HGA w.r.t. the main spacecraft enters GEODYN. Consequently, self-shadowing remains unconsidered. Mazarico et al. (2009) investigated the impact of self-shadowing on the accelerations

¹¹C-kernels for LRO can be downloaded from http://naif.jpl.nasa.gov/pub/naif/pds/data/lro-1-spice-6-v1.0/lrosp_1000/data/

¹²a quaternion is a four-component representation of a rotation matrix: one component is a scalar describing the angle of rotation and the remaining three components specify the rotation axis; within the SPICE information system (and also within GEODYN), a quaternion has a magnitude of one

¹³this is necessary because the rotation angle in SPICE format is limited between 0° and 180°; in GEODYN format, however, it is defined to range from 0° to 360°

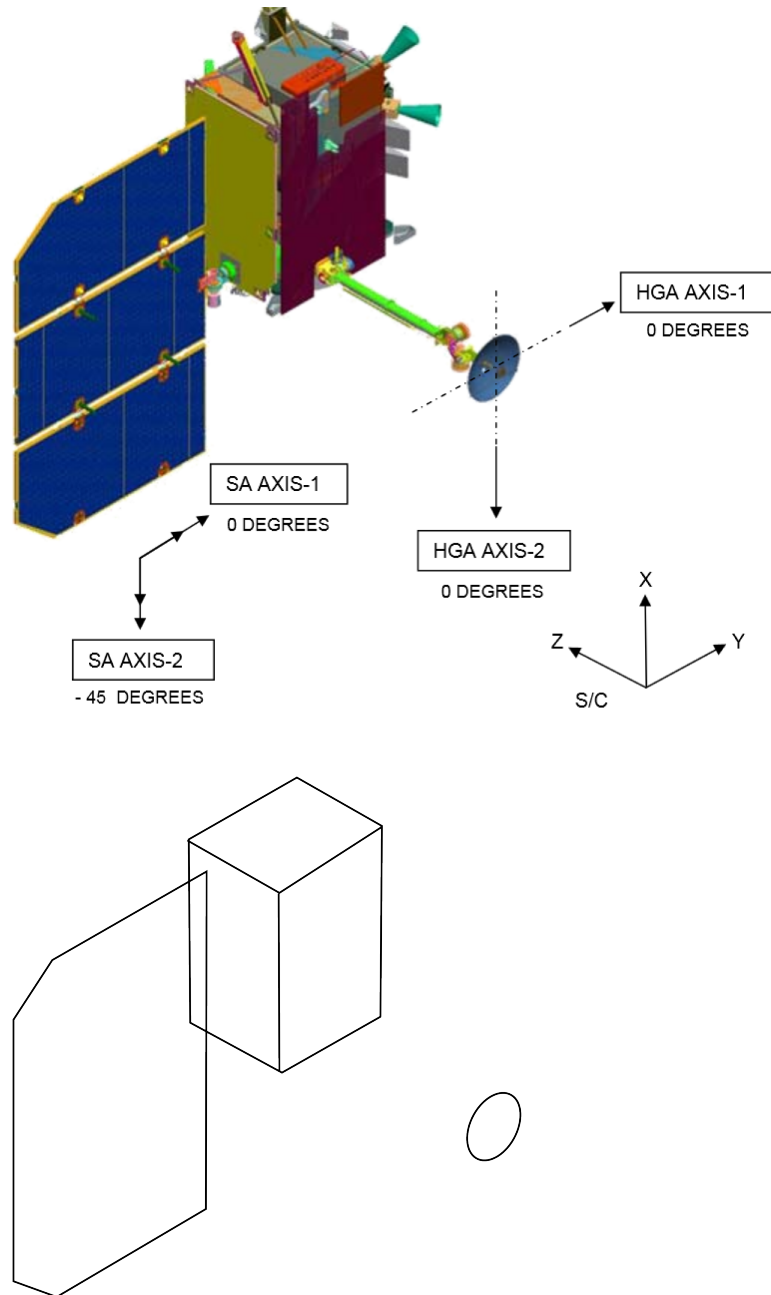


Figure 5.16: (Top) The LRO spacecraft with coordinate systems from Saylor et al. (2009). S/C denotes spacecraft, SA solar array, and HGA high gain antenna. (Bottom) Macro-model approximation.

Table 5.11: LRO macro-model. For each panel, the plate normal unit vector, $\hat{\mathbf{n}}$, is given in the respective frame (cf. Figure 5.16, top), that is the spacecraft bus frame for the spacecraft bus panels (+X, -X, +Y, -Y, +Z, -Z), the solar array frame for the solar array panels (SA+, SA-), and the antenna frame for the high gain antenna panels (HGA+, HGA-). Further, the plate area, A , is given as well as specular reflectivity, ζ , and diffuse reflectivity, δ .

Panel	$\hat{\mathbf{n}}$	A [m ²]	ζ	δ
+X	$\begin{pmatrix} +1 \\ 0 \\ 0 \end{pmatrix}$	2.82	0.29	0.22
-X	$\begin{pmatrix} -1 \\ 0 \\ 0 \end{pmatrix}$	2.82	0.39	0.19
+Y	$\begin{pmatrix} 0 \\ +1 \\ 0 \end{pmatrix}$	3.69	0.32	0.23
-Y	$\begin{pmatrix} 0 \\ -1 \\ 0 \end{pmatrix}$	3.69	0.32	0.23
+Z	$\begin{pmatrix} 0 \\ 0 \\ +1 \end{pmatrix}$	5.14	0.32	0.18
-Z	$\begin{pmatrix} 0 \\ 0 \\ -1 \end{pmatrix}$	5.14	0.54	0.15
SA+	$\begin{pmatrix} 0 \\ -0.7071068 \\ -0.707110 \end{pmatrix}$	11.00	0.05	0.05
SA-	$\begin{pmatrix} 0 \\ +0.7071068 \\ +0.707110 \end{pmatrix}$	11.00	-	-
HGA+	$\begin{pmatrix} 0 \\ 0 \\ -1 \end{pmatrix}$	1.00	0.18	0.28
HGA-	$\begin{pmatrix} 0 \\ 0 \\ +1 \end{pmatrix}$	1.00	0.02	0.05

of the Mars Reconnaissance Orbiter (MRO) and of Mars Odyssey due to solar radiation pressure, atmospheric drag, and albedo. He found that self-shadowing has a significant impact on MRO due to the large HGA and due to the presence of two solar panels. For Mars Odyssey, in contrast, the effect of self-shadowing is minor due its small HGA and its single SA. Since LRO is similar to Mars Odyssey in these respects, self-shadowing is not expected to have a significant impact on the the accelerations of the LRO spacecraft.

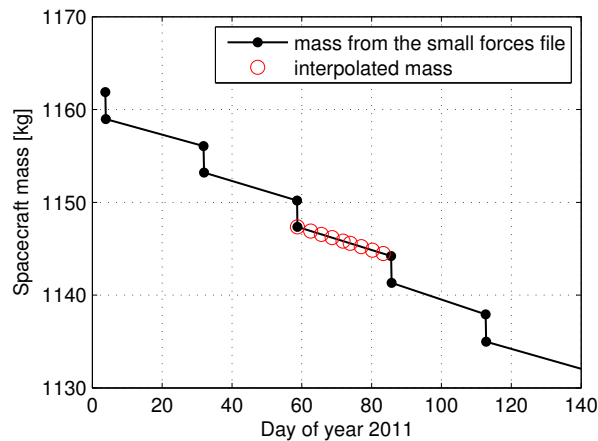


Figure 5.17: The spacecraft mass decreases primarily due to Station Keeping maneuvers (cf. Appendix C.1). The Small Forces Files, which contain the mass before and after each burn, were used to interpolate the mass for the initial state; piecewise linear interpolation was applied. This example shows the spacecraft mass after the two-step burns for the first 140 days of 2011 along with the interpolated mass for all arcs of Science Mission Phase 7. Note that the total mass of LRO before orbit insertion was 1916 kg.

The spacecraft mass, which enters the expressions for the accelerations due to solar radiation and lunar radiation [cf. Equation (2.43) and (2.44)], decreases with increasing life time due to maneuvers. Therefore, the spacecraft mass at the epochs of initial state has been interpolated from the post-burn fuel masses (see Figure 5.17 for an example) that are given in so-called Small Forces Files (SFF). These files contain the type of maneuver, the burn start and stop times, and the pre- and post-burn fuel masses, among other information¹⁴. Figure 5.17 clearly shows the two-burn sequence of the SK

¹⁴SFF were retrieved from <http://pds-geosciences.wustl.edu/lro/lro-1-rss-1-tracking-v1/lrors.0001/data/sff/>; as of August 4, 2014, the last available SFF covers SK31 on December 11, 2011. Since the investigated period ends about two months later, a mass of 1070 kg has been assigned to all arcs after December 11, 2011.

maneuvers. One SK maneuver dissipates about 3 kg of fuel.

5.3.1 Finding the optimal parametrization

Orbit accuracy can only be as good as orbit precision. To assess the latter, orbit overlap tests were conducted over three science mission phases, SM05 to SM07, lasting from January 3, 2011 to March 27, 2011. The objective was to find (1) the optimal set of empirical accelerations and (2) the optimal arc length. Mind that all tests are based solely on Doppler range-rates since this is the major measurement type. In addition to orbit overlaps, observation residuals were analyzed. Concerning the estimation of empirical accelerations, the following five scenarios were tested:

- along track constant,
- along track 1-cycle per revolution (1-cpr),
- along track constant and along track 1-cpr,
- along track constant and cross track constant,
- along track constant and cross track 1-cpr.

Further, three different arc lengths were evaluated: an arc length of 1.25 days (short arcs), an arc length of 2.5 days (medium arcs), and an arc length of 4.5 days (long arcs). Short, medium, and long arcs overlap by 6 hours, 12 hours, and 36 hours, respectively (cf. Figure 5.18).

In case of short arcs, the RMS value of overlap differences amounts to 25.64 m in total position when estimating one constant empirical parameter in along track direction (Table 5.12). The overall RMS value of the residuals (3.9 mm/s) is larger than the nominal precision (1 mm/s for WS1S and 3 mm/s for the USN stations). Figure 5.19 (left) reveals, however, that the RMS value of the residuals that high comes from a few very large residuals. For time spans when these large residuals are missing, the residuals of the short arcs are smaller than those of the medium arcs (cf. Figure 5.19, right). Due to the large orbit overlap differences compared to medium arcs, the short arcs were not further investigated. When it comes to medium arcs, the RMS values of overlap differences are significantly lower than for short arcs. In addition, the residuals are more homogenous compared to the short arcs (cf. Figure 5.19, left). Among all five scenarios of empirical accelerations listed above, estimating a constant empirical acceleration in along track direction yields the smallest RMS value of overlap differences in total position, i.e.

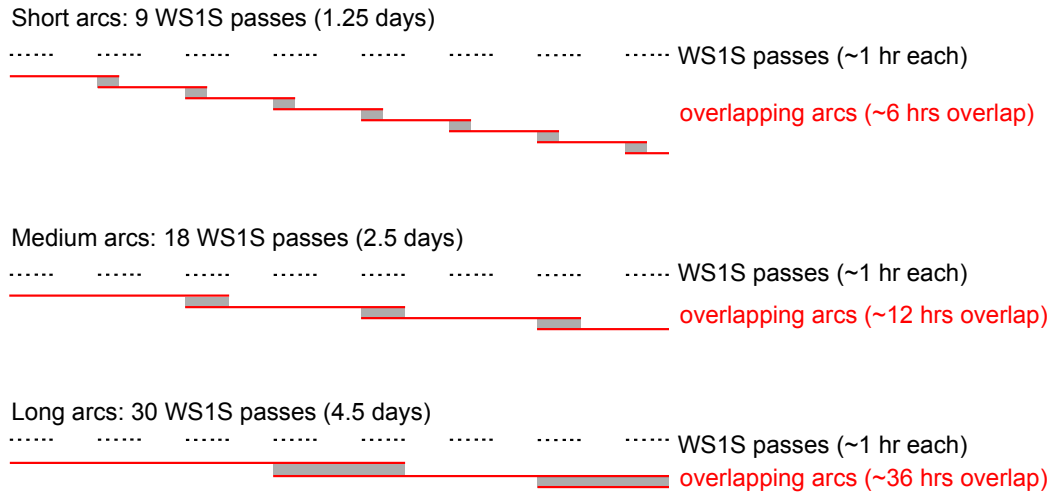


Figure 5.18: Illustration of dividing a time span of 7.5 days into short arcs (top), medium arcs (middle), and long arcs (bottom) that overlap by 6 hours, 12 hours, and 36 hours, respectively. Start and stop time of overlapping arcs were chosen according to observed White Sands (WS1S) passes.

3.57 m (cf. Table 5.13). For long arcs the RMS values of overlap differences and residuals tend to increase compared to medium arcs (Table 5.14).

Table 5.12: Short arcs (1.25 days): averaged RMS values of overlap differences and RMS value of observation residuals.

Empirical acceleration	RMS of orbit overlaps [m]				RMS of residuals [mm/s]
	Along	Cross	Radial	Total	
Along track constant	19.01	14.76	1.06	25.64	3.90

The analysis of orbit overlaps and observation residuals revealed that the highest precision is achieved using medium arcs of 2.5 days in length and estimating constant empirical accelerations in along track direction. The optimal arc length of 2.5 days is in perfect agreement with the statement in Rowlands et al. (2009) that arcs for LRO are usually limited to 2 or 3 days due to force model errors and orbital maneuvers. The optimal arc length and the optimal choice of empirical accelerations have been adopted for all further investigations.

The nominal precision of the primary station's tracking data is by a factor of 3 better compared to the USN stations (cf. Section 5.1.2). Hence, one would

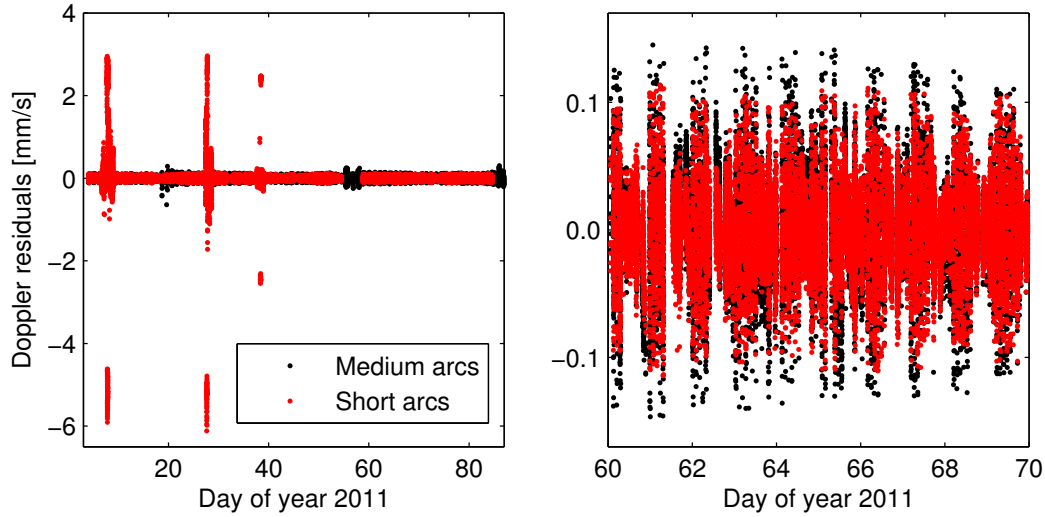


Figure 5.19: Wide view (left) and narrow view (right) of range-rate residuals for short arcs and medium arcs.

Table 5.13: Medium arcs (2.5 days): averaged RMS values of overlap differences and RMS value of observation residuals.

Empirical acceleration	RMS of orbit overlaps [m]				RMS of residuals [mm/s]
	Along	Cross	Radial	Total	
Along track constant	2.44	2.22	0.22	3.57	0.30
Along track 1-cpr	11.56	11.12	0.70	17.43	0.60
Along track constant, along track 1-cpr	4.81	3.08	0.48	6.47	1.20
Along track constant, cross track const.	2.61	2.47	0.20	3.89	0.30
Along track constant, cross track 1-cpr	4.60	4.60	0.21	6.94	0.30

Table 5.14: Long arcs (4.5 days): averaged RMS values of overlap differences and RMS value of observation residuals.

Empirical acceleration	RMS of orbit overlaps [m]				RMS of residuals
	Along	Cross	Radial	Total	[mm/s]
Along track constant	3.86	5.20	0.35	6.75	0.40
Along track 1-cpr	56.74	57.72	7.60	85.00	3.80
Along track constant, along track 1-cpr	2.68	3.55	0.23	4.66	0.40
Along track constant, cross track const.	4.16	5.52	0.35	7.19	0.40
Along track constant, cross track 1-cpr	6.54	8.62	0.38	11.14	0.30

expect that assigning a standard deviation of 1 mm/s to the observations of the primary station and 3 mm/s to those of the USN stations would result in more precise orbits than using the same standard deviation for all observations. This was, however, not the case. Computing RMS values of the Doppler range-rate residuals averaged over all arcs (13 months) for the primary station on one hand and for the secondary stations on the other hand gave an RMS value of 0.72 mm/s for the primary station and 0.82 mm/s for the USN stations. Hence, the performance of primary and secondary stations is much more alike than the nominal values would suggest.

5.3.2 Results

About 13 months (January 3, 2011 to February 9, 2012) of Doppler data were processed as overlapping arcs of 2.5 days in length to assess orbital precision. These 13 months relate to 15 science mission phases (SM05 to SM19) or more than 130 arcs. Extreme outliers were deleted prior to orbit determination by using information from the science orbits¹⁵. The advantage is primarily a shorter computational time because orbit convergence is met sooner¹⁶. Estimated arc and global parameters are summarized in Table 5.15.

¹⁵all observations that differed from the range-rates generated to the science orbits of LRO by more than 10 m/s were removed

¹⁶Moreover, prior outlier detection is necessary when laser ranges and Doppler shall be processed together. In this case the edit level must be chosen very generously due to the huge bias in laser ranges. With a high edit level, however, the anomalous Doppler data are not detected as outliers by GEODYN resulting in a degraded orbit in the best case and abortion due to hyperbolic trajectory in the worst case.

Table 5.15: Estimated arc and global parameters for orbits based on Doppler range-rates

<i>Arc parameters</i>	
Solar radiation pressure coefficient	1 per arc
Empirical acceleration	along track constant (1 per arc)
Measurement bias	1 per station and arc
Satellite state vector	1 per arc
<i>Global parameters</i>	
Gravity field coefficients	up to degree and order 60

Figure 5.20 depicts the estimated measurement biases for each ground station. Whereas the biases of the primary station WS1S are generally very small (on average 0.1 mm), they are at the level of 10 mm for the USN stations.

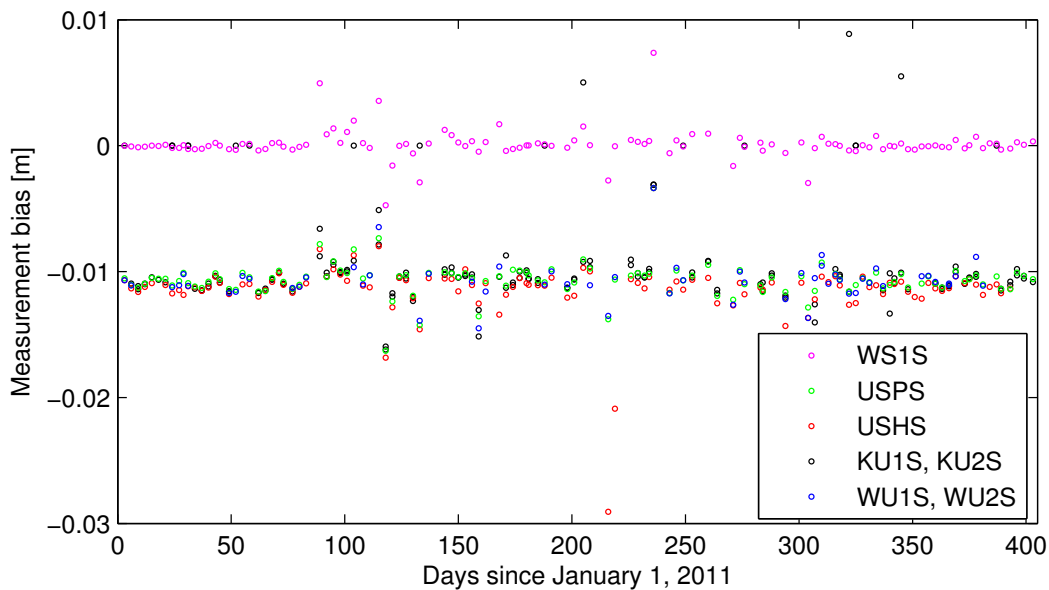


Figure 5.20: Estimated measurement biases for the ground stations tracking LRO via two-way Doppler range-rates

The range-rate residuals are correlated with the Earth viewing geometry angle (Figure 5.21), which is the angle between LRO's orbital plane and the line-of-sight direction between station and satellite. They are smaller for face-on geometries, where the cosine of the angle is zero, and higher for edge-on geometries, where the cosine of the angle is 1. The better fits do

not indicate better orbits though (Mazarico et al., 2012). The different color coding for range-rate residuals from White Sands and those from the USN stations (Figure 5.21, top) demonstrates the slightly better performing of the primary station. The residuals are generally smaller than the nominal precision (1 mm/s for WS1S and 3 mm/s for USN stations). Three arcs, which showed significantly larger values, were not considered for gravity field estimation. Figure 5.22 depicts the RMS values of observation residuals per orbital arc. The RMS values show a systematic pattern. They are small at the beginning and at the end of the investigated time span with larger values in between.

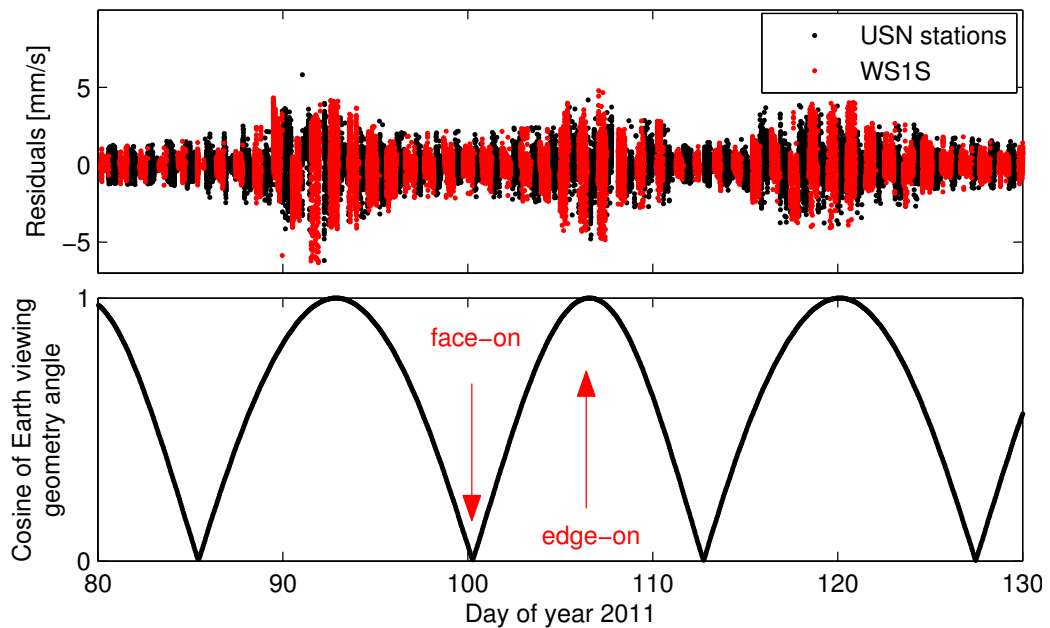


Figure 5.21: Range-rate residuals for the primary station White Sands and the USN stations (top) and the dependence on the Earth viewing geometry angle (bottom).

The RMS values of orbit overlap differences are depicted in Figure 5.23 (top). The pattern is similar to the one we have seen for the observation residuals (cf. Figure 5.22): small at the beginning and at the end of the time span with larger values in between. It is not clear to the author where this pattern originates from. Park et al. (2012) states that for solar beta angles less than the value at terminator crossing ($\pm 76.4^\circ$ for LRO)

“... modeling non-gravitational forces becomes much more difficult, as the perturbations are changing more rapidly due to part of the orbit being in shadow, ... ”.

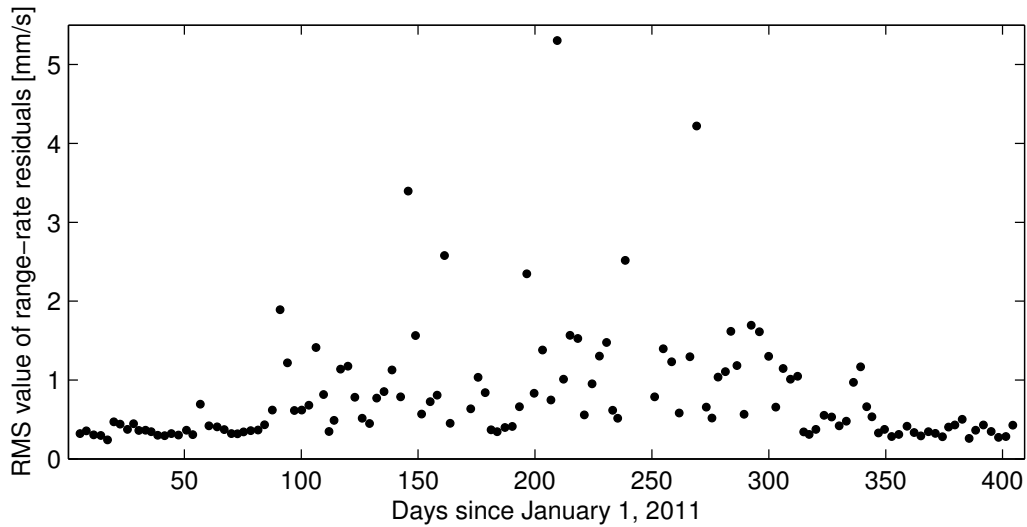


Figure 5.22: RMS values of Doppler range-rate residuals per arc.

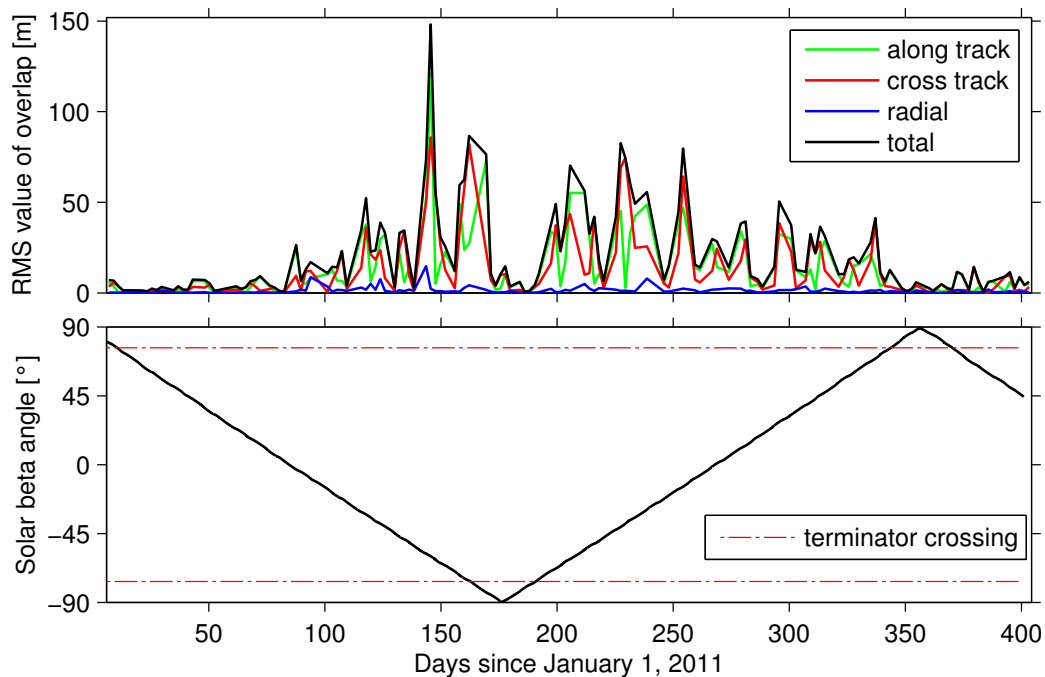


Figure 5.23: (Top) RMS values of orbit overlaps in the spacecraft reference frame. There seems to be a connection between the RMS values and the solar beta angle (bottom). LRO start terminator crossing at $\pm 76.4^\circ$.

Hence, the solar beta angle is depicted in Figure 5.23 (bottom). A correlation between orbital precision and the solar beta angle cannot be clearly identified though.

The RMS values of the orbit overlaps averaged over the investigated science mission phases are given in Table 5.16. Over the entire investigated time span, the overlap tests indicate that the orbit determined from Doppler range-rates is precise to 13.79 m, 14.17 m, and 1.28 m in along track, cross track, and radial direction, respectively, as well as 21.32 m in total position.

Table 5.16: RMS values of orbit overlap differences and of orbit differences w.r.t. the science orbits averaged over the considered science mission phases (SM).

SM	RMS of orbit overlaps [m]				RMS of orbit differences [m]			
	along track	cross track	radial	total	along track	cross track	radial	total
5	1.87	2.03	0.25	2.99	4.76	3.08	0.64	6.02
6	2.54	2.38	0.15	3.68	3.96	2.72	0.42	5.09
7	2.91	2.28	0.24	4.06	3.16	2.97	0.49	4.69
8	9.34	8.73	2.34	14.42	10.68	6.42	1.80	13.16
9	18.08	17.49	2.34	26.89	10.48	6.53	1.34	12.97
10	36.43	45.09	3.13	61.57	13.46	14.25	1.55	20.95
11	10.63	6.06	0.53	12.92	10.71	4.29	1.83	12.84
12	24.84	23.48	1.95	37.45	14.54	10.34	2.40	19.03
13	37.06	45.10	3.07	61.71	11.95	11.41	2.95	18.58
14	23.60	20.46	1.70	32.27	9.77	5.59	2.00	11.68
15	17.73	14.57	1.27	23.67	9.55	6.99	2.24	12.75
16	12.48	14.62	1.14	20.92	10.65	9.93	1.30	15.35
17	11.18	14.93	1.14	19.93	17.48	12.81	1.86	23.02
18	3.11	1.94	0.58	4.16	4.82	2.33	0.80	5.82
19	3.71	4.11	0.61	6.54	6.47	4.95	0.88	8.74

The estimated LRO orbit is compared against the science orbits provided by Navigation and Ancillary Information Facility (NAIF). The tracking data the orbits are based on are not the same though. Here, solely Doppler measurements are used, whereas the science orbits additionally incorporate radiometric ranges and altimetric crossovers (Mazarico et al., 2012). Table 5.16 summarizes the RMS values per orbital arc (cf. Figure 5.24) according to science mission phases. Averaged over the entire time span, the computed

orbits agree within 9.50 m, 6.98 m, and 1.50 m in along track, cross track, and radial direction, respectively, and within 12.71 m in total position.

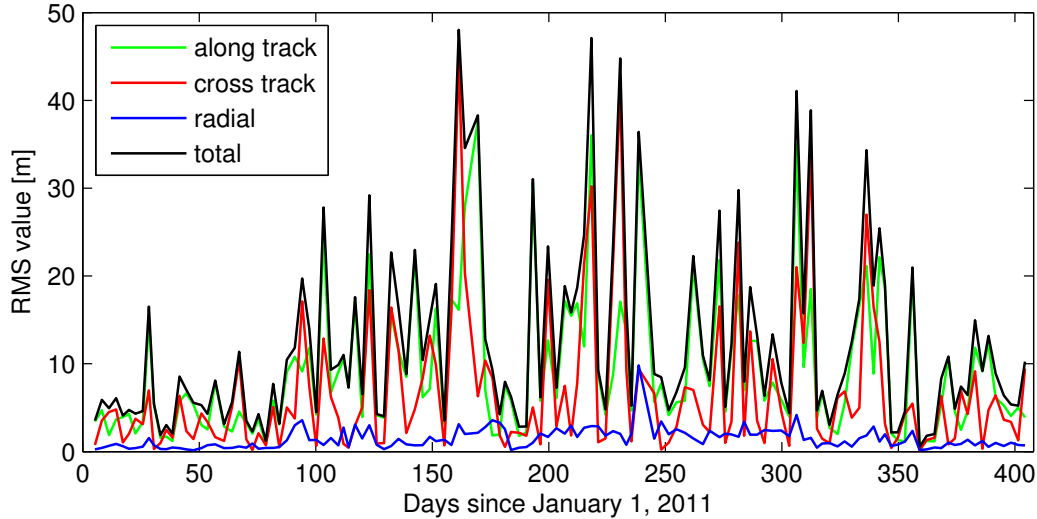


Figure 5.24: RMS values of differences per arc between the computed orbit that is based solely on Doppler range-rates and the science orbit that is based on Doppler range-rates, radiometric ranges, and altimetric crossovers.

An attempt was made to determine LRO's orbit solely from laser ranges. An arc length of ~ 2.5 days did not prove successful though. Thus, a time span of about three months (SM05 to SM07) was subdivided into longer arcs of about 7 days in length. The estimated arc parameters can be found in Table 5.17. Since the LRO clock parameters play a crucial role in processing one-way laser ranges to LRO, they shall be discussed at this point. Figure 5.25 shows the estimated measurement biases for four stations set up for each pass. These biases account mostly for the difference between the reference time at the station and the reference time at the spacecraft. In most cases, the bias of one pass is very similar to the previous one as it is expected. The distinct jumps in the biases are due to jumps in the observed one-way laser range. The estimated drift of the LRO clock (see Figure 5.26, top) agrees well with the drift rate published by Mao et al. (2014) who estimated the clock parameters solely from the primary station. The drift should, however, follow a straight line which is only partly the case.

Estimating the orbit solely from laser ranges, the RMS values of orbit differences w.r.t. the science orbits are 373 m, 23 m, and 17 m in along track, cross track, and radial direction, respectively. The RMS value of range residuals is 3.4 m, which is one order of magnitude larger than the nominal precision

(10 cm). The reason for this rather poor precision is probably due to the insufficient modeling of the LRO clock using a polynomial of second degree. Due to the bad performance of orbits solely computed from laser ranges, LRO's final orbit presented in this thesis is based on Doppler range-rates.

Table 5.17: Estimated arc parameters for orbits based solely on laser ranges

Solar radiation pressure coefficient	1 per arc
Empirical acceleration	along track constant (1 per arc)
Measurement bias	1 per station and pass
LRO clock drift rate and aging rate	1 per arc
Satellite state vector	1 per arc

The author also tried to determine LRO's orbit from laser ranges and Doppler range-rates in a combined estimation process. A series of tests has shown, however, that no convergence is achieved using the respective nominal precision, i.e. 1 mm/s for Doppler range-rates and 10 cm for laser ranges. An increased standard deviation for laser ranges of ~ 1 m results in convergence; the orbit turned out to be of much poorer quality compared to that one determined from Doppler-only data. Increasing the standard deviation further to several meters results in an orbit similar to the Doppler-only orbit since then the laser ranges have only a tiny contribution. Consequently, the orbits on which gravity field recovery is based on were reconstructed solely from two-way Doppler range-rates.

Once we have settled on how the final LRO orbits are estimated, it might be interesting to have a look at the accelerations acting on the satellite (note that the acceleration due to the lunar gravity field is dealt with separately in Section 5.4). Representative for the entire time span, the acceleration due to all modeled gravitational and non-gravitational forces is shown for 24 hours. To start with the gravitational forces, the acceleration due to third bodies is illustrated in Figure 5.27. The Earth has the largest effect due to its proximity, followed by the Sun because of its huge gravitational parameter (cf. Table 5.9). Among the relativistic forces, the Schwarzschild field is the major contributor (cf. Figure 5.28). It depends on the distance between spacecraft and central body (Park et al., 2005). The closer Moon and Sun the larger the effect (cf. Figure 5.29). Figure 5.28 gives an overall picture of the acceleration due to gravitational forces. Third bodies have the largest impact, followed by the solid Moon tide.

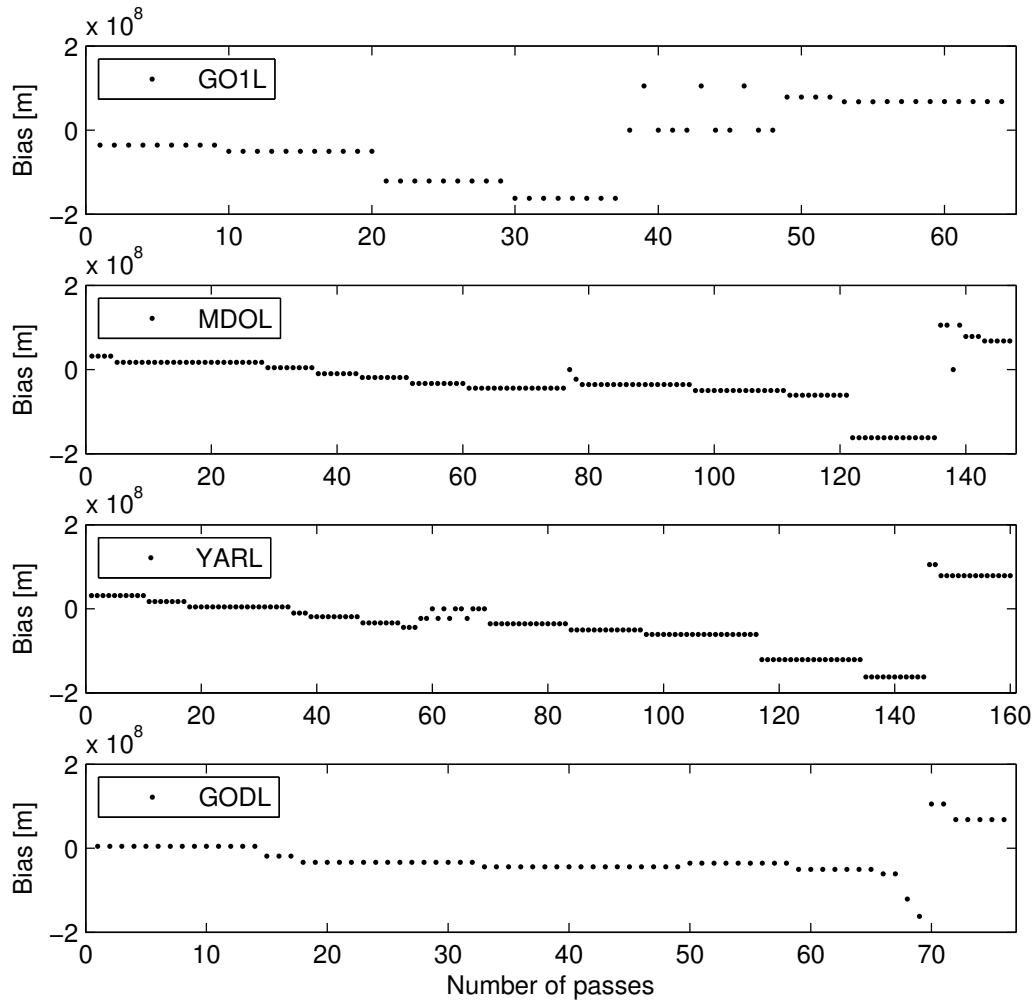


Figure 5.25: Pass per pass measurement biases for four stations tracking LRO via optical laser ranges.

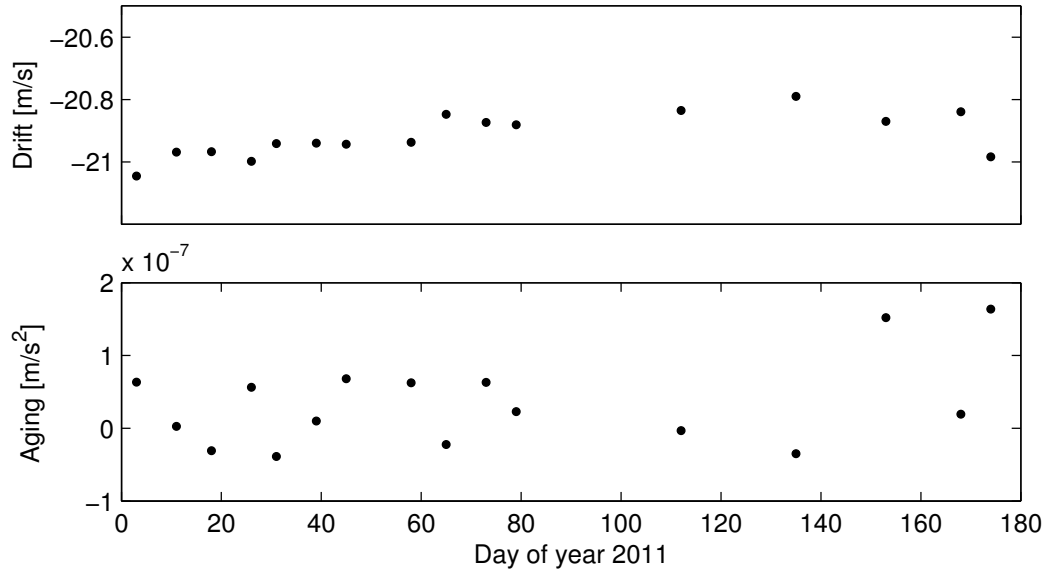


Figure 5.26: LRO clock drift (top) and aging rate (bottom) estimated from all stations.

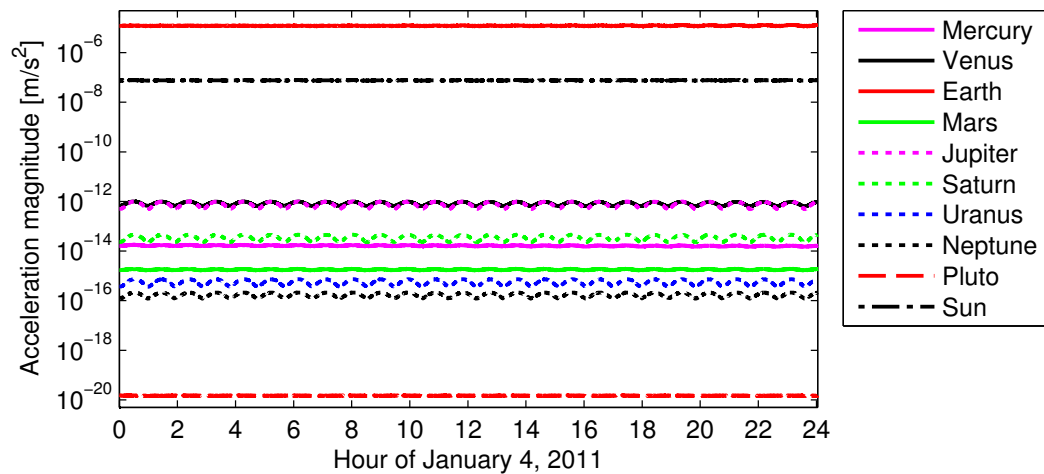


Figure 5.27: Acceleration due to third bodies modeled as point-masses on a logarithmic scale. All eight planets of our solar system are considered as well as Pluto and the Sun.

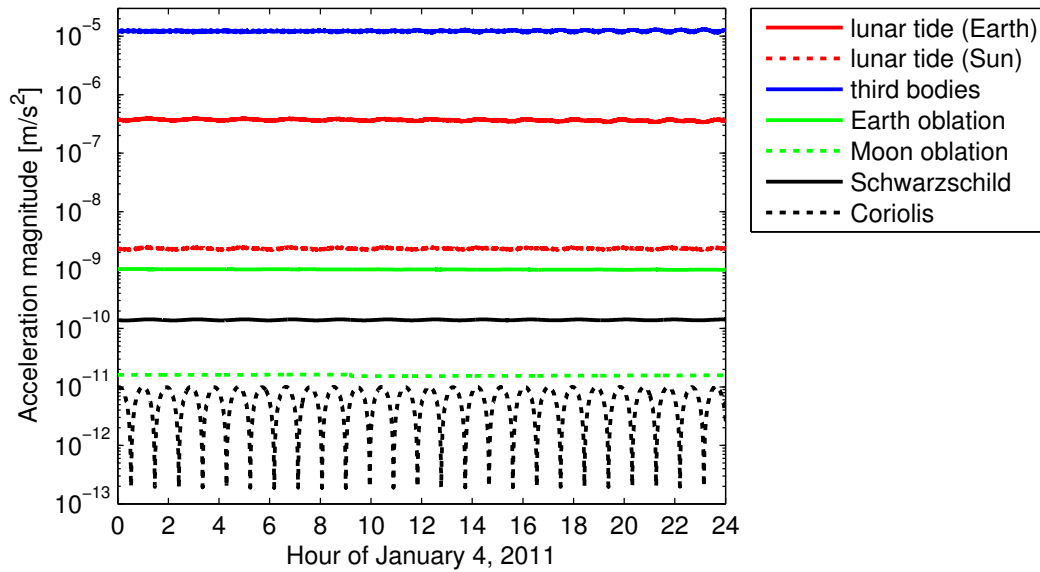


Figure 5.28: Acceleration magnitude acting on LRO due to solid Moon tides, third bodies, Earth and Moon oblation, and general relativity (Schwarzschild and Coriolis).

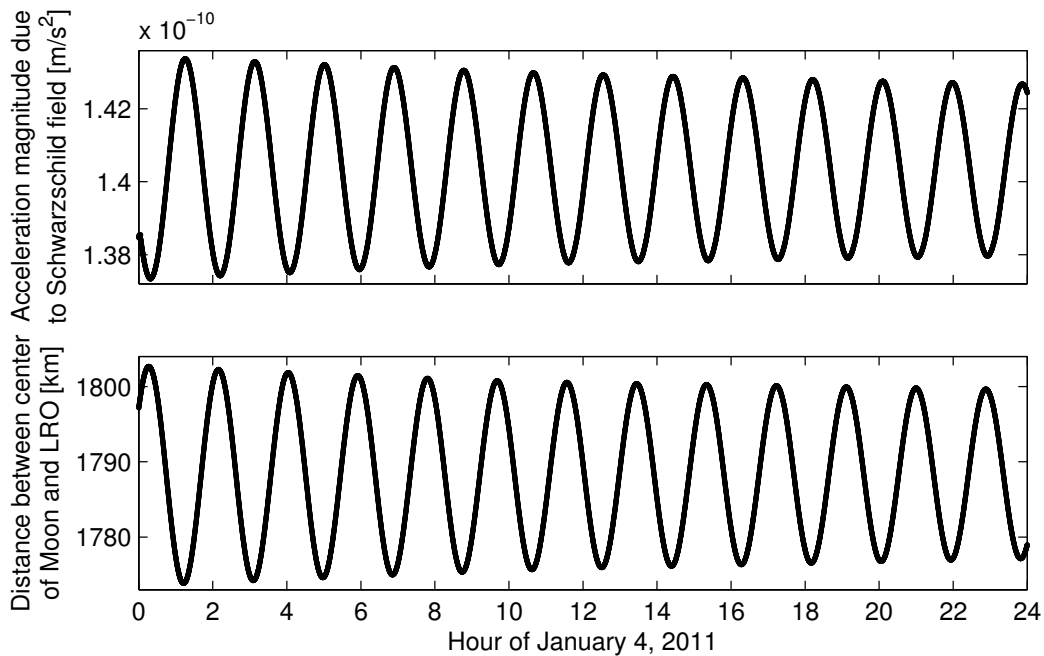


Figure 5.29: (Top) Acceleration due to the general relativistic Schwarzschild field. This effect is at its maximum in close proximity to the Moon (bottom).

Figure 5.30 depicts the acceleration on LRO due to the modeled non-gravitational forces, i.e. solar radiation pressure and lunar radiation pressure (albedo and emissivity). At a low solar beta angle (cf. Figure 5.30, top) the perturbations change rapidly as part of the orbit is in shadow. At a high solar beta angle (cf. Figure 5.30, bottom), in contrast, the perturbations are smoother. Because emissivity is independent on illumination conditions (cf. Section 2.1.2), the acceleration acting on LRO is nearly constant (cf. Figure 5.30). The acceleration due to albedo, on the other hand, is highly variable even for high solar beta angles (cf. Figure 5.30, bottom).

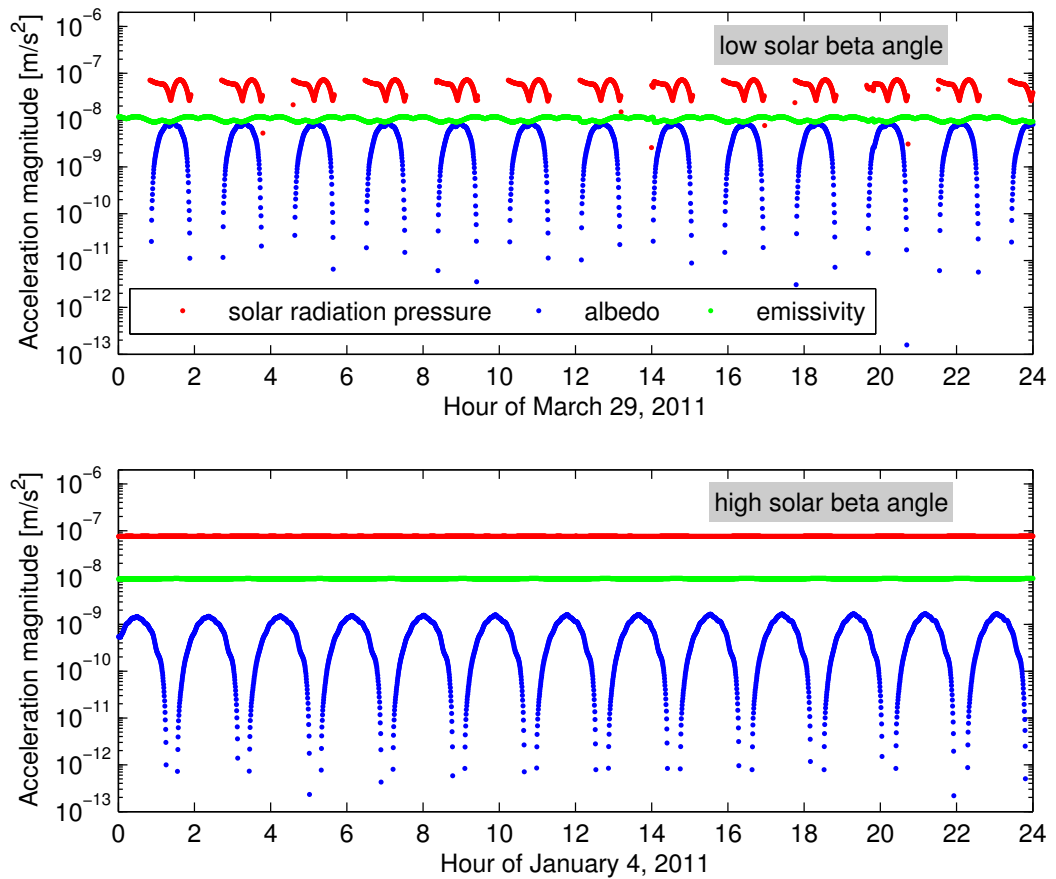


Figure 5.30: Acceleration magnitude acting on LRO due to solar radiation pressure and lunar radiation pressure (albedo and emissivity). Acceleration at low solar beta angle (top) and at high solar beta angle (bottom).

5.4 Gravity field recovery

For the estimation of lunar gravity field coefficients, the orbit was computed without overlapping periods. Otherwise, the observations within the overlaps would count twice. The arc length was approximately 3 days¹⁷ including 18 White Sands passes as well as passes from secondary stations. Over the entire investigated time span of 13 months, all orbital arcs were combined for the estimation of gravity field coefficients up to d/o 60 (those from d/o 51 to 60 shall absorb spectral leakage). The gravity field solution is based on 1 908 507 Doppler range-rates.

As for the simulation studies, Tikhonov-Phillips regularization was applied. Again, the L-curve criterion was used to find the optimal regularization parameter, albeit the large dimension of the design matrix precluded usage of the `regtools` toolbox (cf. Section 3). Figure 5.31 shows the L-curve for regularization parameters varying between 0.5 and 2500. The curve does not have a distinct corner. Since the numerical values of the regularization parameters are very similar in the central part, the lack of a distinct corner is not thought to be critical. By visual inspection of Figure 5.31, the optimal regularization parameter was set to 9.

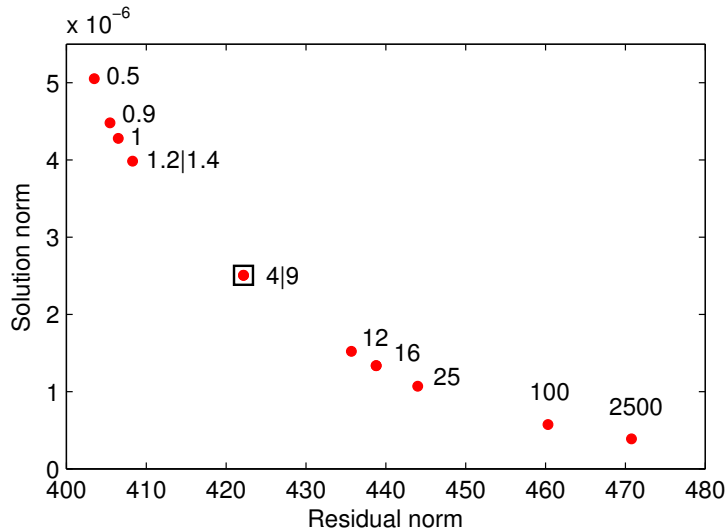


Figure 5.31: Residual norm vs. solution norm for regularization parameters varying between 0.5 and 2500. The curve lacks a distinct corner. The optimal regularization parameter (marked with a box) was set to 9.

¹⁷arc 1: first observation from WS1S pass 1 to first observation from WS1S pass 19, arc 2: first observation from WS1S pass 19 to first observation from WS1S pass 37, etc.

To find out from which spherical harmonic d/o onwards the coefficients have to be regularized, four gravity field solutions were computed by regularizing all coefficients of $d/o \geq 2, 6, 11,$ and 16 . Whereas the formal errors of the very first two solutions are nearly identical (Figure 5.32), a significant increase of the formal errors can be seen when the gravity field is regularized from $d/o 11$ or 16 onwards. Based on Figure 5.32 the decision was made to freely adjust all coefficients up to $d/o 5$ and starting regularization from $d/o 6$.

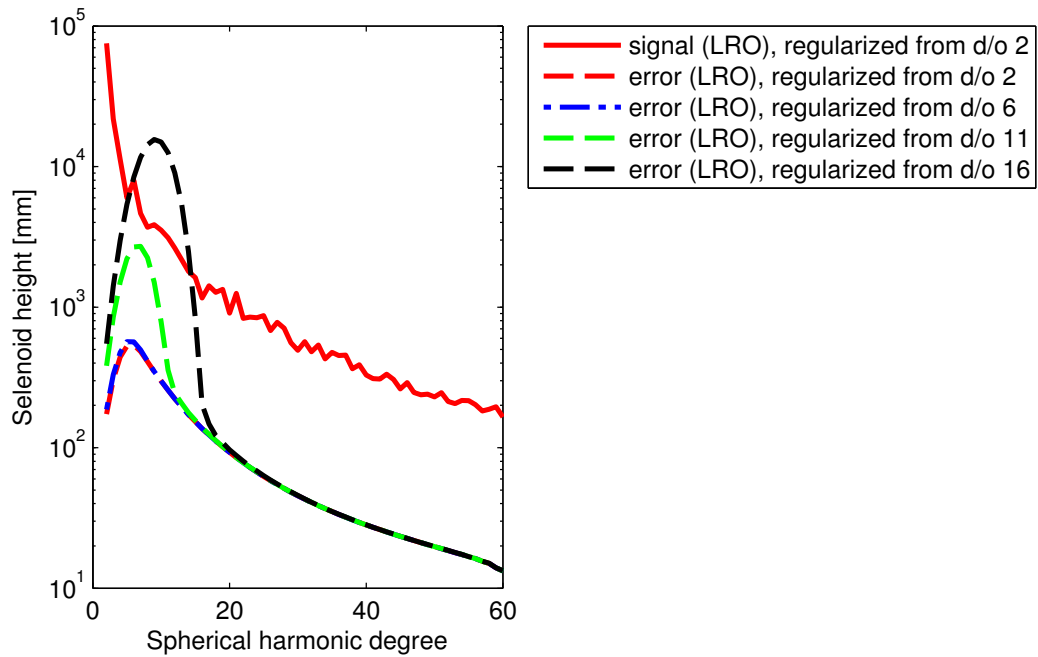


Figure 5.32: Degree-wise signal and errors of the gravity field coefficients estimated from Doppler range-rates to LRO in terms of selenoid height. The formal errors are shown for solutions regularized from $d/o 2, 6, 11,$ and 16 .

Accounting for the variance of the unit weight¹⁸, the signal and errors of the estimated gravity field coefficients can be compared against those of the a priori gravity field model GL0660B (Figure 5.33). Whereas the signals agree well, the errors of the LRO-derived solution are significantly larger than those of the GRAIL-derived model GL0660B. Note that GRAIL provided a substantial leap of knowledge due to the concept of low-low satellite-to-satellite tracking (Zuber et al., 2013). Since no model is available that is solely based on tracking data to LRO, the errors of the Lunar Prospector (LP)

¹⁸the variance of the unit weight is defined as $\frac{\hat{\mathbf{v}}^T \mathbf{P} \hat{\mathbf{v}}}{l-u}$, where $\hat{\mathbf{v}}$ are the estimated observation errors, \mathbf{P} is the observation weight matrix, and l and u are the number of observations and unknowns, respectively

model JGL165P1 are shown in Figure 5.33 to compare the LRO-derived solution with; this comparison is justified as JGL165P1 is also based on ground-based tracking data. The errors of JGL165P1 steadily increase up to d/o 15 since regularization was applied from d/o 16 onwards (Konopliv et al., 2001). The error level of SGM150J (Goossens et al., 2011a), a SELENE-derived gravity field model including data to LP, is slightly lower compared to JGL165P1 and the LRO-derived model as some tracking data are available over the farside.

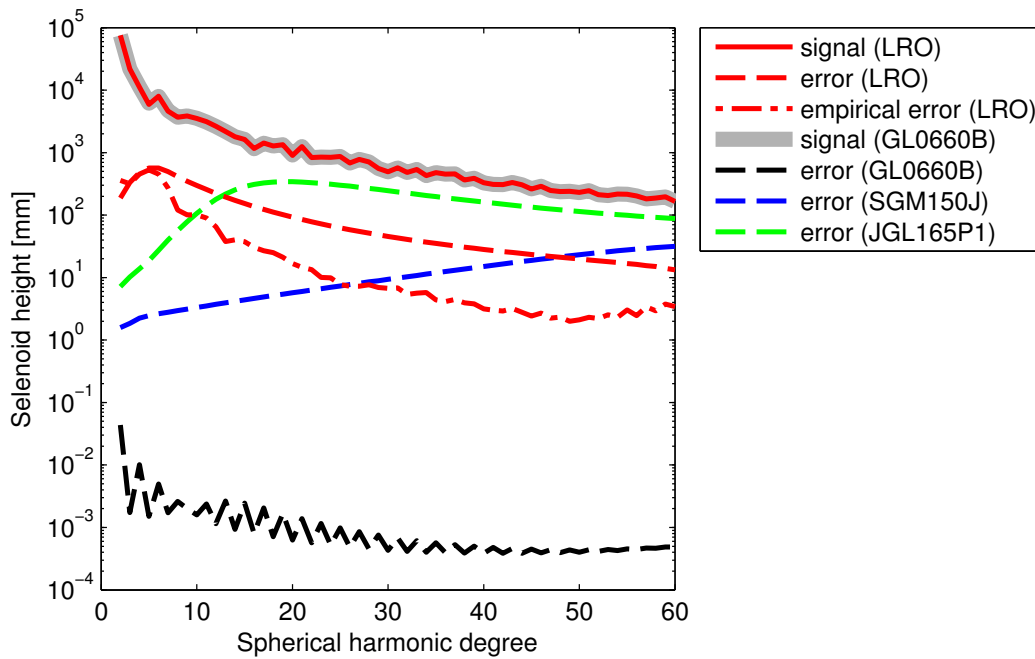


Figure 5.33: Degree-wise signal, formal errors, and empirical errors (w.r.t. GL0660B) of the recovered gravity field solution based on Doppler range-rates to LRO in terms of selenoid height (in red color). In addition, the signal and the errors of the a priori GRAIL-derived model (GL0660B) are shown. Further, the errors of JGL165P1 (based on LP) and those of SGM150J (based on LP and SELENE) are depicted.

Figure 5.34 depicts the differences in selenoid height between the regularized gravity field solution and the a priori gravity field model GL0660B. At the farside of the Moon, the differences are as large as ± 15 m. At the nearside (Figure 5.35), the differences are smallest near the lunar equator where tracking data are densest (cf. Figure 5.8). The differences on the nearside are at maximum ± 2 m.

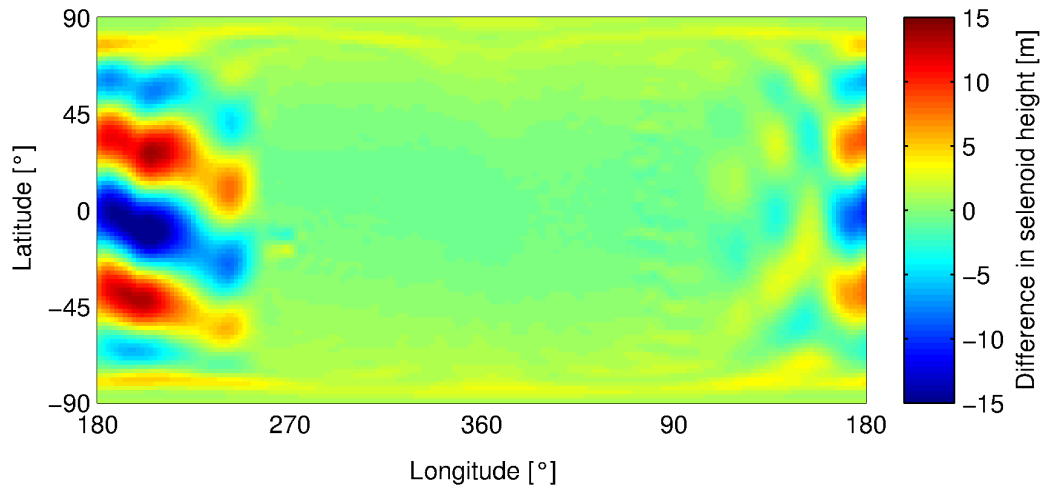


Figure 5.34: Differences in selenoid height between the regularized gravity field solution (truncated at degree and order 50) and the a priori gravity field model GL0660B. The larger discrepancies at the farside (located between 90° and 270° in longitude) due to the lack of direct tracking data is clearly visible.

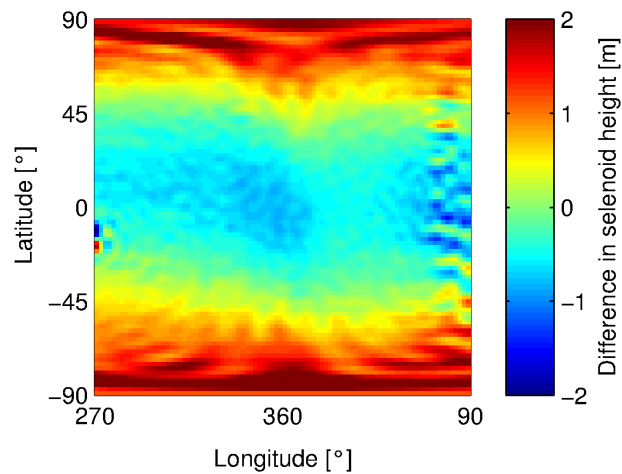


Figure 5.35: Differences in selenoid height between the regularized gravity field solution (truncated at degree and order 50) and the a priori gravity field model GL0660B (nearside). The differences are largest at the poles where Doppler tracking is sparsest.

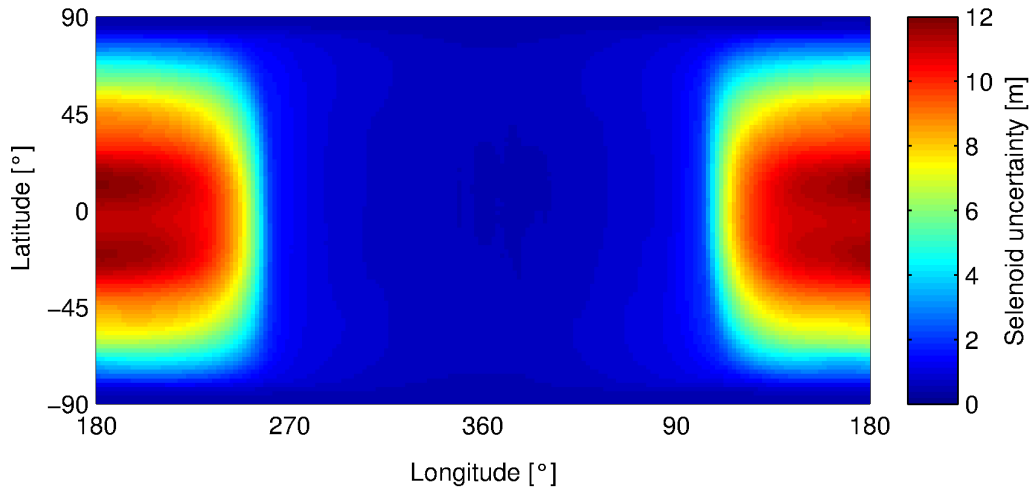


Figure 5.36: Selenoid uncertainties for the regularized gravity field solution derived from Doppler range-rates to LRO. Error propagation was implemented according to Haagmans and Gelderen (1991) using the full variance-covariance information. The uncertainties are illustrated for coefficients up to degree and order 50.

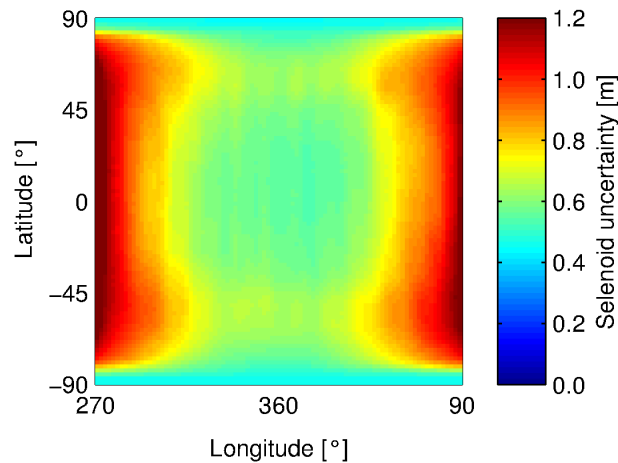


Figure 5.37: Selenoid uncertainties for the regularized gravity field solution derived from Doppler range-rates to LRO (nearside). The uncertainties are illustrated for coefficients up to degree and order 50.

The selenoid uncertainties of the derived gravity field solution, shown in Figure 5.36, can be as large as 12m on the deep farside. On the nearside of the Moon (Figure 5.37), where direct tracking data are available, the uncertainties are one order of magnitude smaller.

5.5 Discussion and conclusions

The low precision of the LRO orbit when computed solely from optical one-way laser ranges is attributed to the insufficient parametrization of the LRO clock. The estimation of a cubic frequency aging rate, as suggested by Mao et al. (2014), was not supported by the software version at hand. Further, an arc length of seven days might be too short for a robust estimation of clock parameters. Mao et al. (2013), for instance, used an arc length of two weeks to infer the LRO clock parameters. In the work presented here, longer arcs did not improve the results.

To some extent, the temporal variation of the Doppler residuals can be explained by the solar beta angle. The correlation, however, is far from perfect. Since the parametrization is the same for the entire time span, the reason for the varying magnitude of the residuals (apart from the solar beta angle) remains unclear.

The largest gravitational force LRO is exposed to (apart from the lunar gravity field), is due to the presence of third bodies (cf. Figure 5.28). Among the third bodies, the Earth and the Sun have the largest impact due to the small distance and the large mass, respectively. The most prominent non-gravitational force acting on LRO is solar radiation pressure (cf. Figure 5.30). The acceleration due to lunar radiation pressure is approximately one order of magnitude smaller. Whenever the satellite's orbit is partially shadowed by the Moon, force modeling is more demanding since then the accelerations due to non-gravitational forces change rapidly (cf. Figure 5.30). Insufficiencies coming from this side are reflected in the RMS values of the orbit overlaps (cf. Figure 5.23).

Up to d/o 12, the formal errors of the LRO-based gravity field solution are larger than those of JGL165P1. This might be due to the fact that the latter contains 18 months of radio tracking data to LP as well as historical data to Lunar Orbiter 1 to 5, Apollo 15 and 16 subsatellites, and Clementine (Konopliv et al., 2001). From d/o 16 on, the formal errors of the LRO solution are smaller than those of JGL165P1 since the former was regularized from d/o 6 onwards as opposed to the latter which was regularized from d/o 16

onwards.

A decrease of the errors of the recovered gravity field solution (cf. Figure 5.33), albeit a moderate one, could be achieved by increasing the analyzed time span. The limiting factor, however, is clearly the single-hemisphere data coverage. The awesome effect of global data coverage in combination with a very precise measurement type on the degree-wise errors can be seen in Figure 5.33 for the GRAIL-derived gravity field model GL0660B.

The selenoid uncertainties (Figures 5.36 and 5.37), which were computed from the formal errors, are in good agreement with the differences between the estimated gravity field signal and the a priori model (Figures 5.34 and 5.35). Hence, the conclusion is drawn that the formal errors are realistic.

Chapter 6

Discussion

Gravity field recovery from Satellite Laser Ranging (SLR) measurements to geodetic satellites on the one hand, and from Doppler data to the Lunar Reconnaissance Orbiter (LRO) on the other hand, tackles the same problem: the gravity field shall be derived from satellite perturbations triggered by changes in the central body's gravity field. Although the concept is the same for the Earth and the Moon, the practical implementation is not.

First, the quality of available tracking data is different. The nominal precision of two-way optical laser ranges to geodetic satellites is a factor of 70 to 100 times better than the precision of one-way optical laser ranges to LRO. For both the Earth and the Moon the data coverage is not uniform. Whereas for the Earth the data gaps are primarily located in oceanic areas and polar regions, the Moon suffers from a farside data gap being almost as large as one half of the entire lunar surface. Consequently, ill-conditioning is a major issue for lunar gravity field recovery from Doppler range-rates to LRO and a minor issue for terrestrial gravity field recovery from SLR measurements to geodetic satellites.

Laser ranges to LRO are extremely precise and should therefore be an integral part of Precise Orbit Determination (POD). A significant effort was put into the analysis of laser ranges – unfortunately without much success. Mao et al. (2013) demonstrated that it is possible to deduce LRO orbits from laser ranges only, albeit of reduced quality compared to S-band only orbits. Since in Mao et al. (2014) the LRO clock is modeled by a third-degree polynomial, it is suspected that the second-degree polynomial, which is used by the software, is not able to capture the entire signature of the spacecraft clock.

Second, the dominant perturbing forces are different for Earth and Moon

orbiting satellites. The lower orbiting geodetic satellites (Stella, Starlette, Larets) are significantly perturbed by atmospheric drag, which is difficult to model. Consequently, the range residuals to these satellites are larger than those to higher orbiting satellites such as LAGEOS-1/2. For a lunar orbiter, the dominant non-gravitational force is solar radiation pressure since the Moon has no atmosphere. The acceleration due to lunar radiation pressure is approximately one order of magnitude smaller.

Third, non-gravitational force modeling is different for geodetic satellites and LRO due to the satellites' shape. Whereas the former are simple spheres, the latter is complex due to the attached Solar Array (SA) and the High Gain Antenna (HGA). In particular, LRO's single SA is large (11 m^2) requiring a proper modeling of its orientation. The non-gravitational force modeling for LRO is even more demanding for time spans when its orbit is partially shadowed since then the forces change rapidly. Insufficiencies coming from this side might be (at least to some extent) responsible for the larger range-rate residuals whenever parts of the orbit is in shadow.

Regarding the derived gravity field solutions, spectral leakage is negligible for geodetic satellites because of their high orbital altitude. For LRO, however, leakage is crucial to account for as the spacecraft is orbiting the Moon at only 50 km above the lunar surface. The easiest way, which was also pursued in this work, is to estimate more coefficients than actually needed.

To sum up the author's achievements, the quality of the estimated orbits and the derived gravity field information are in good agreement with published results by other established research groups. The presented gravity field solutions for the Earth and the Moon, however, should not be seen as stand-alone solutions. SLR-based normal equations are an integral part of combined satellite-only gravity field models such as the models of the Gravity Observation Combination (GOCO) series¹. Concerning the Moon, future will tell whether LRO-based normal equations contribute to gravity field solutions derived from Gravity Recovery and Interior Laboratory (GRAIL) data (Zuber et al., 2013).

¹visit <http://www.goco.eu/> for more information

Bibliography

- Acton, C. H. J. (1996). Ancillary data services of NASA's Navigation and Ancillary Information Facility. *Planet. Space Sci.* 44(1), pp. 65–70.
- Asmar, S. W. (2005). Spacecraft Doppler tracking: Noise budget and accuracy achievable in precision radio science observations. *Radio Sci.* 40(2), pp. 1–9.
- Asmar, S. W., A. S. Konopliv, M. M. Watkins, J. G. Williams, R. S. Park, G. Kruizinga, M. Paik, D.-N. Yuan, E. Fahnestock, D. Strelakov, N. Harvey, W. Lu, D. Kahan, K. Oudrhiri, D. E. Smith, and M. T. Zuber (2013). The Scientific Measurement System of the Gravity Recovery and Interior Laboratory (GRAIL) Mission. *Space Sci. Rev.* 178(1), pp. 25–55.
- Baur, O. and N. Sneeuw (2011). Assessing Greenland ice mass loss by means of point-mass modeling: a viable methodology. *J. Geod.* 85(9), pp. 607–615.
- Beckman, M. (2006). *Mission Design for the Lunar Reconnaissance Orbiter*. 29th Annual AAS Guidance and Control Conference, Breckendridge, Colorado. URL: http://lunar.gsfc.nasa.gov/library/LRO_AAS_Paper_07-057.pdf.
- Berman, A. L. (1972). *Mariner 9 Doppler Noise Study*. The Deep Space Network Progress Report, TR 32-1526, pp. 227–235.
- Bettadpur, S. (2012). *GRACE UTCSR Level-2 Processing Standards Document For Level-2 Product Release 0005*. URL: ftp://podaac.jpl.nasa.gov/allData/grace/docs/L2-CSR0005_ProcStd_v4.0.pdf.
- Biancale, R., A. Cazenave, and K. Dominh (1991). Tectonic plate motions derived from LAGEOS. *Earth Planet. Sci. Lett.* 103, pp. 379–394.
- Bizouard, C. and D. Gambis (2007). *The combined solution C04 for Earth Orientation Parameters consistent with International Terrestrial Reference Frame 2008*. URL: <ftp://hpiers.obspm.fr/iers/eop/eopc04/C04.guide.pdf>.
- Böhm, J., B. Werl, and H. Schuh (2006). Troposphere mapping functions for GPS and very long baseline interferometry from European Centre for

- Medium-Range Weather Forecasts operational analysis data. *J. Geophys. Res.* 111(B2), B02406.
- Bowman, B. R., W. K. Tobiska, F. A. Marcos, C. Y. Huang, C. S. Lin, and W. J. Burke (2008). A New Empirical Thermospheric Density Model JB2008 Using New Solar and Geomagnetic Indices. In: *Proceedings of the AIAA/AAS Astrodynamics Specialist Conference*. Honolulu, USA. URL: http://sol.spacenvironment.net/jb2006/pubs/AIAA_2008-6438_JB2008_Model.pdf.
- Bruinsma, S. L., N. Sánchez-Ortiz, E. Olmedo, and N. Guijarro (2012). Evaluation of the DTM-2009 thermosphere model for benchmarking purposes. *J. Sp. Weather Sp. Clim.* 2, A04.
- Bruinsma, S. L., C. Förste, O. Abrikosov, J.-C. Marty, M.-H. Rio, S. Mulet, and S. Bonvalot (2013). The new ESA satellite-only gravity field model via the direct approach. *Geophys. Res. Lett.* 40(14), pp. 3607–3612.
- Capitaine, N., P. T. Wallace, and J. Chapront (2003). Expressions for IAU 2000 precession quantities. *Astron. Astrophys.* 412, pp. 567–586.
- Chao, B. F. and W. P. O’Connor (1988). Global surface-water-induced seasonal variations in the Earth’s rotation and gravitational field. *Geophys. J. Int.* 94(2), pp. 263–270.
- Chao, B. F. and A. Y. Au (1991). Temporal Variation of the Earth’s Low-Degree Zonal Gravitational Field Caused by Atmospheric Mass Redistribution: 1980-1988. *J. Geophys. Res.* 96(B4), pp. 6569–6575.
- Chen, J. L., C. R. Wilson, R. J. Eanes, and B. D. Tapley (2000). A new assessment of long-wavelength gravitational variations. *J. Geophys. Res.* 105(B7), pp. 271–277.
- Chen, J. L., C. R. Wilson, B. D. Tapley, J. S. Famiglietti, and M. Rodell (2005). Seasonal global mean sea level change from satellite altimeter, GRACE, and geophysical models. *J. Geod.* 79(9), pp. 532–539.
- Chen, J. L., C. R. Wilson, and K.-W. Seo (2009). S2 tide aliasing in GRACE time-variable gravity solutions. *J. Geod.* 83(7), pp. 679–687.
- Cheng, M. and B. D. Tapley (2004). Variations in the Earth’s oblateness during the past 28 years. *J. Geophys. Res.* 109(B09402), pp. 1–9.
- Cheng, M., J. C. Ries, and B. D. Tapley (2011). Variations of the Earth’s figure axis from satellite laser ranging and GRACE. *J. Geophys. Res.* 116(B1), pp. 1–14.
- Chin, G., S. Brylow, M. Foote, J. Garvin, J. Kasper, J. Keller, M. Litvak, I. Mitrofanov, D. Paige, K. Raney, M. Robinson, A. Sanin, D. Smith, H. Spence, P. Spudis, S. A. Stern, and M. Zuber (2007). Lunar Reconnaissance Orbiter Overview: The Instrument Suite and Mission. *Space Sci. Rev.* 129(4), pp. 391–419.

- Ciufolini, I. and E. C. Pavlis (2004). A confirmation of the general relativistic prediction of the LenseThirring effect. *Nature* 431(7011), pp. 958–960.
- Colombo, O. L. (1989). The dynamics of global positioning system orbits and the determination of precise ephemerides. *J. Geophys. Res. Solid Earth* 94(B7), pp. 9167–9182.
- Combrinck, L. (2013). General Relativity and Space Geodesy. In: *Sciences of Geodesy - II*. Ed. by G. Xu. Springer Berlin Heidelberg, pp. 53–95.
- Cook, D. G. (2001). Solar radiation pressure modeling issues for high altitude satellites. Master’s Thesis. Air University. URL: <http://www.dtic.mil/dtic/tr/fulltext/u2/a390187.pdf>.
- Degnan, J. J. (2013). Millimeter Accuracy Satellite Laser Ranging: a Review. In: *Contributions of Space Geodesy to Geodynamics: Technology*. Ed. by D. E. Smith and D. L. Turcotte. Geodynamics Series Volume 25. American Geophysical Union, Washington, D. C., pp. 133–162. URL: <http://ilrs.gsfc.nasa.gov/docs/1993/MillimeterAccuracySatelliteLaserRangingReview.pdf>.
- Doody, D. (2009). *Deep Space Craft: An Overview of Interplanetary Flight*. Springer Berlin Heidelberg New York.
- Drinkwater, M., R. Haagmans, D. Muzi, A. Popescu, R. Floberghagen, M. Kern, and M. Fehringer (2006). The GOCE gravity mission: ESA’s first core explorer. In: *Proceedings of the 3rd International GOCE User Workshop*. Frascati, Italy, ESA SP-627, 1–8. URL: http://esamultimedia.esa.int/docs/GOCE_3rd_Workshop_Drinkwater_et_al.pdf.
- EGG-C (2010). *GOCE Standards*. GO-TN-HPF-GS-0111, Issue 3.2. URL: https://earth.esa.int/c/document_library/get_file?folderId=14168&name=DLFE-572.pdf.
- Flechtner, F., H. Dobslaw, and E. Fagiolini (2014a). *AOD1B Product Description Document for Product Release 05*. Rev. 4.2, GRACE 327-750, pp. 1–33. URL: ftp://podaac.jpl.nasa.gov/allData/grace/docs/AOD1B_20140520.pdf.
- Flechtner, F., M. Watkins, P. Morton, F. Webb, F.-H. Massmann, and L. Grunwaldt (2014b). *Status of the GRACE follow-on mission*. EGU General Assembly 2014, Geophysical Research Abstracts 16: EGU2014-4460.
- Floberghagen, R., R. Noomen, P. N. A. M. Visser, and G. D. Racca (1996). Global lunar gravity recovery from satellite-to-satellite tracking. *Planet. Space Sci.* 44(10), pp. 1081–1097.
- Floberghagen, R., P. Visser, and F. Weischede (1999). Lunar albedo force modelling and its effect on low lunar orbit and gravity field determination. *Adv. Sp. Res.* 23(4), pp. 733–738.
- Floberghagen, R. (2002). *Lunar Gravimetry: Revealing the Far-Side*. Vol. 273. Astrophysics and Space Science Library. Kluwer Academic Publishers.

- Folkner, W. M., J. G. Williams, and D. H. Boggs (2009). *The Planetary and Lunar Ephemeris DE 421*. Interplanetary Network Progress Report 42-178, pp. 1–34. URL: http://ipnpr.jpl.nasa.gov/progress_report/42-178/178C.pdf.
- Förste, C., F. Flechtner, R. Schmid, R. Stubenvoll, M. Rothacher, J. Kusche, H. Neumayer, R. Biancale, J.-M. Lemoine, F. Barthelmes, S. Bruinsma, R. König, and U. Meyer (2008). *EIGEN-5C: A new global combined high-resolution GRACE-based gravity field model of the GFZ-GRGS cooperation*. Presented at the EGU general assembly in Vienna, Austria. URL: http://op.gfz-potsdam.de/grace/results/grav/g007_eigen-05c_files/foerste_EGU2008-A-03426.pdf.
- Goossens, S. (2010). Applying spectral leakage corrections to gravity field determination from satellite tracking data. *Geophys. J. Int.* 181, pp. 1459–1472.
- Goossens, S., K. Matsumoto, Q. Liu, F. Kikuchi, K. Sato, H. Hanada, Y. Ishihara, H. Noda, N. Kawano, N. Namiki, T. Iwata, F. G. Lemoine, D. D. Rowlands, Y. Harada, and M. Chen (2011a). Lunar gravity field determination using SELENE same-beam differential VLBI tracking data. *J. Geod.* 85(4), pp. 205–228.
- Goossens, S., K. Matsumoto, D. D. Rowlands, F. G. Lemoine, H. Noda, and H. Araki (2011b). Orbit determination of the SELENE satellites using multi-satellite data types and evaluation of SELENE gravity field models. *J. Geod.* 85(8), pp. 487–504.
- Haagmans, R. H. N. and M. V. Gelderen (1991). Error Variances-Covariances of GEM-T1: Their Characteristics and Implications in Geoid Computation. *J. Geophys. Res.* 96(B12), pp. 11–22.
- Hansen, P. C. (1998). *Rank-Deficient and Discrete Ill-Posed Problems: Numerical Aspects of Linear Inversion*. Siam Monographs on Mathematical Modeling and Computation.
- Hansen, P. C. (2000). The L-Curve and its Use in the Numerical Treatment of Inverse Problems. In: *Computational Inverse Problems in Electrocardiology*. Ed. by P. Johnston. Advances in Computational Bioengineering. WIT Press, pp. 119–142.
- Hansen, P. C. (2008). *Regularization Tools: A Matlab Package for Analysis and Solution of Discrete Ill-Posed Problems*. URL: <http://www.imm.dtu.dk/~pcha/Regutools/RTv4manual.pdf>.
- Hedin, A. E. (1987). MSIS-86 Thermospheric Model. *J. Geophys. Res.* 92(A5), pp. 4649–4662.
- Heiskanen, W. A. and H. Moritz (1967). *Physical Geodesy*. San Francisco, W.H. Freeman.

- Hopfield, H. S. (1963). The Effect of Tropospheric Refraction on the Doppler Shift of a Satellite Signal. *J. Geophys. Res.* 68(18), pp. 5157–5168.
- Hopfield, H. S. (1969). Two-Quartic Tropospheric Refractivity Profile for Correcting Satellite Data. *J. Geophys. Res.* 74(18), pp. 4487–4499.
- Hopfield, H. S. (1971). Tropospheric effect on electromagnetically measured range: Prediction from surface weather data. *Radio Sci.* 6(3), pp. 357–367.
- Houghton, M. B., C. R. Tooley, and R. S. Saylor (2007). Mission design and operations considerations for NASA’s Lunar Reconnaissance Orbiter. In: *Proceedings of the 58th International Astronautical Congress*. Hyderabad, India, pp. 1–8. URL: <http://lunar.gsfc.nasa.gov/library/IAC-07-C1.7.06.pdf>.
- Huang, C., J. C. Ries, B. D. Tapley, and M. M. Watkins (1990). Relativistic effects for near-earth satellite orbit determination. *Celest. Mech. Dyn. Astron.* 48(2), pp. 167–185.
- Iorio, L. (2001). Testing General Relativity with LAGEOS, LAGEOS II and Ajisai laser-ranged satellites. *J. Geodet. Soc. Jap.* 48, pp. 13–20.
- Iorio, L. (2002). Testing General Relativity in the gravitational field of the Moon with SELENE mission. *Class. Quantum Gravity* 19, pp. 2393–2398.
- IPCC (2013). *Climate Change 2013: The Physical Science Basis. Contribution of Working Group I to the Fifth Assessment Report of the Intergovernmental Panel on Climate Change*. Ed. by T. F. Stocker, D. Qin, G.-K. Plattner, M. Tignor, S. K. Allen, J. Boschung, A. Nauels, Y. Xia, V. Bex, and P. M. Midgley. Cambridge University Press, Cambridge, United Kingdom and New York, NY, USA.
- Johnson, T. J., C. R. Wilson, and B. F. Chao (2001). Nontidal oceanic contributions to gravitational field changes: Predictions of the Parallel Ocean Climate Model. *J. Geophys. Res.* 106(B6), pp. 315–334.
- Kang, Z., B. Tapley, S. Bettadpur, J. Ries, P. Nagel, and R. Pastor (2006). Precise orbit determination for the GRACE mission using only GPS data. *J. Geod.* 80(6), pp. 322–331.
- Kaula, W. M. (1966). *Theory of Satellite Geodesy*. London: Blaisdell Pub. Co., p. 124.
- Keller, J. W., N. E. Petro, T. P. McClanahan, R. R. Vondrak, and J. B. Garvin (2014). Recent Results from the Lunar Reconnaissance Orbiter Mission and Plans for a Second Extended Science Mission. In: *Proceedings of the 45th Lunar and Planetary Science Conference*. The Woodlands, Texas. URL: <http://www.hou.usra.edu/meetings/lpsc2014/pdf/2294.pdf>.
- Kikuchi, F., Q. Liu, H. Hanada, N. Kawano, K. Matsumoto, T. Iwata, S. Goossens, K. Asari, Y. Ishihara, S. Tsuruta, T. Ishikawa, H. Noda, N.

- Namiki, N. Petrova, Y. Harada, J. Ping, and S. Sasaki (2009). Picosecond accuracy VLBI of the two subsatellites of SELENE (KAGUYA) using multifrequency and same beam methods. *Radio Sci.* 44(2).
- King-Hele, D. G. (1962). The Earth's Gravitational Potential, deduced from the Orbits of Artificial Satellites. *Geophys. J. R. Astron. Soc.* 4(S0), pp. 270–272.
- King-Hele, D. G. and G. E. Cook (1965). The Even Zonal Harmonics of the Earth's Gravitational Potential. *Geophys. J. Int.* 10, pp. 17–29.
- Knocke, P. C., J. C. Ries, and B. D. Tapley (1988). Earth radiation pressure effects on satellites. In: *Proceedings of the AIAA/AAS Astrodynamics Conference*. Minneapolis.
- Knocke, P. (1989). Earth radiation pressure effects on satellites. PhD thesis. The University of Texas at Austin. URL: <ftp://ftp.csr.utexas.edu/pub/reports/CSR-89-1.pdf>.
- Konopliv, A., S. W. Asmar, E. Carranza, W. L. Sjogren, and D. N. Yuan (2001). Recent Gravity Models as a Result of the Lunar Prospector Mission. *Icarus* 150, pp. 1–18.
- Konopliv, A., C. Yoder, E. Standish, D. Yuan, and W. Sjogren (2006). A global solution for the Mars static and seasonal gravity, Mars orientation, Phobos and Deimos masses, and Mars ephemeris. *Icarus* 182(1), pp. 23–50.
- Konopliv, A. S., R. S. Park, D.-N. Yuan, S. W. Asmar, M. M. Watkins, J. G. Williams, E. Fahnestock, G. Kruizinga, M. Paik, D. Strelakov, N. Harvey, D. E. Smith, and M. T. Zuber (2013). The JPL lunar gravity field to spherical harmonic degree 660 from the GRAIL Primary Mission. *J. Geophys. Res. Planets* 118(7), pp. 1415–1434.
- Kucharski, D., H.-C. Lim, G. Kirchner, and F. Koidl (2014). Spin parameters of Low Earth Orbiting satellites Larets and Stella determined from Satellite Laser Ranging data. *Adv. Sp. Res.* 53(1), pp. 90–96.
- Kusche, J. and R. Klees (2002). Regularization of gravity field estimation from satellite gravity gradients. *J. Geod.* 76(6-7), pp. 359–368.
- Lavallée, D. A., P. Moore, P. J. Clarke, E. J. Petrie, T. van Dam, and M. A. King (2010). J2: An evaluation of new estimates from GPS, GRACE, and load models compared to SLR. *Geophys. Res. Lett.* 37(22), pp. 3–7.
- Lemoine, F. G., S. Goossens, T. J. Sabaka, J. B. Nicholas, E. Mazarico, D. D. Rowlands, B. D. Loomis, D. S. Chinn, D. S. Caprette, G. A. Neumann, D. E. Smith, and M. T. Zuber (2013). High-degree gravity models from GRAIL primary mission data. *J. Geophys. Res. Planets* 118, pp. 1676–1698.
- Lense, J. and H. Thirring (1918). The influence of the self-rotation of central bodies on the movements of the planets and the moon according to Ein-

- stein's theory of gravitation. *Transl. from Phys. Zeitschrift* 19, pp. 156–163.
- Luthcke, S. B., N. P. Zelensky, D. D. Rowlands, F. G. Lemoine, and T. A. Williams (2003). The 1-Centimeter Orbit: Jason-1 Precision Orbit Determination Using GPS, SLR, DORIS, and Altimeter Data. *Mar. Geod.* 26, pp. 399–421.
- Lyard, F., F. Lefevre, T. Letellier, and O. Francis (2006). Modelling the global ocean tides: modern insights from FES2004. *Ocean Dyn.* 56(5-6), pp. 394–415.
- Maier, A., S. Krauss, W. Hausleitner, and O. Baur (2012). Contribution of satellite laser ranging to combined gravity field models. *Adv. Sp. Res.* 49(3), pp. 556–565.
- Maier, A., S. Krauss, and O. Baur (2014). The role of Satellite Laser Ranging in terrestrial gravity field recovery. *Österr. Zeitschr. Verm. Geoinf.* 1/2014.
- Mao, D., J. McGarry, M. Torrence, G. Neumann, E. Mazarico, M. Barker, X. Sun, D. Rowlands, J. Golder, T. Zagwodzki, J. Cavanaugh, M. Zuber, and D. Smith (2011). Laser Ranging Experiment on Lunar Reconnaissance Orbiter: Timing Determination and Orbit Constraints. In: *Proceedings of the 17th International Workshop on Laser Ranging*. Bad Kötzing, Germany, pp. 1–4. URL: http://cddis.gsfc.nasa.gov/lw17/docs/papers/session13/02-Mao_LR0-LR_Kotzting2011_paper_final.pdf.
- Mao, D., X. Sun, J. McGarry, E. Mazarico, M. Torrence, D. Rowlands, G. Neumann, M. Barker, J. Golder, D. Smith, and M. Zuber (2013). LRO Orbit Determination with Laser Ranging Data. In: *Proceedings of the 18th International Workshop on Laser Ranging*. Fujiyoshida, Japan, pp. 1–6. URL: <http://cddis.gsfc.nasa.gov/lw18/docs/papers/Posters/13-Po26-Mao.pdf>.
- Mao, D., J. McGarry, M. Torrence, X. Sun, J. Horvath, C. Clarke, M. Barker, J. Golder, E. Mazarico, G. Neumann, D. Smith, and M. Zuber (2014). *Summary of Ground Station Performance in Five Years of Laser Ranging Operation to Lunar Reconnaissance Orbiter*. Presented at the 19th International Workshop on Laser Ranging, Annapolis MD. URL: http://ilrs.gsfc.nasa.gov/ilrw19/docs/2014/Posters/3158_Mao_poster.pdf.
- Marini, J. W. and C. W. Murray (1973). *Correction of laser range tracking data for atmospheric refraction at elevations above 10 degrees*. Tech. rep. Goddard Space Flight Center, Greenbelt, MD. URL: <http://hdl.handle.net/2060/19740007037>.
- Marshall, J. A., S. B. Luthcke, P. G. Antreasian, and G. W. Rosborough (1992). *Modeling Radiation on TOPEX/Poseidon for Precision Orbit Forces*

- Acting Determination*. NASA Technical Memorandum 104564. URL: https://archive.org/details/nasa_techdoc_19920019100.
- Mashhoon, B., F. W. Hehl, and D. S. Theiss (1984). On the Gravitational Effects of Rotating Masses: The Thirring-Lense Papers. *Gen. Relativ. Gravit.* 16(8), pp. 711–750.
- Mayer-Gürr, T., R. Pail, T. Gruber, T. Fecher, M. Rexer, W.-D. Schuh, J. Kusche, J.-M. Brockmann, I. Krasbutter, S. Becker, A. Eicker, J. Schall, D. Rieser, N. Zehentner, O. Baur, E. Höck, W. Hausleitner, A. Maier, S. Krauss, A. Jäggi, M. Ulrich, and L. Prange (2012). *The new combined satellite only model GOCO03s*. Presented at the GGHS 2012, Venice, Italy. URL: <http://www.goco.eu/>.
- Mazarico, E., M. T. Zuber, F. G. Lemoine, and D. E. Smith (2009). Effects of Self-Shadowing on Nonconservative Force Modeling for Mars-Orbiting Spacecraft. *J. Spacecr. Rockets* 46(3), pp. 662–669.
- Mazarico, E., D. D. Rowlands, G. A. Neumann, D. E. Smith, M. H. Torrence, F. G. Lemoine, and M. T. Zuber (2012). Orbit determination of the Lunar Reconnaissance Orbiter. *J. Geod.* 86(3), pp. 193–207.
- McCarthy, D. D. and G. Petit, eds. (2004). *IERS Conventions (2003)*. IERS Technical Note No. 32. Verlag des Bundesamtes für Kartographie und Geodäsie, Frankfurt am Main 2004. URL: http://202.127.29.4/cddisa/data_base/IERS/Conventions/Convention_2003/tn32_IERS_Conventions_2003.pdf.
- McCarthy, J., S. Rowton, D. Moore, D. Pavlis, S. Luthcke, and L. Tsaoussi (1993). *GEODYN II systems description*. 4400 Forbes Blvd., Lanham, MD 20706.
- McGarry, J., R. Zellar, N. G., C. Noll, M. Torrence, J. Horvath, C. Clarke, R. Ricklefs, M. Pearlman, and A. Mallama (2008). Laser Ranging to the Lunar Reconnaissance Orbiter: a Global Network Effort. In: *Proceedings of the 16th International Workshop on Laser Ranging*. Poznań, Poland.
- McGarry, J., X. Sun, D. Mao, J. Horvath, H. Donovan, C. Clarke, E. Hoffman, J. Cheek, T. Zagwodzki, M. Torrence, M. Barker, E. Mazarico, G. Neumann, D. Smith, and M. Zuber (2013). LRO-LR : Four Years of History-Making Laser Ranging. In: *Proceedings of the 18th International Workshop on Laser Ranging*. Fujiyoshida, Japan. URL: <http://cddis.gsfc.nasa.gov/lw18/docs/papers/Session9/13-04-05-McGarry.pdf>.
- Mendes, V. B., G. Prates, E. Pavlis, D. Pavlis, and R. Langley (2002). Improved mapping functions for atmospheric refraction correction in SLR. *Geophys. Res. Lett.* 29(10).
- Mendes, V. B. and E. C. Pavlis (2004). High-accuracy zenith delay prediction at optical wavelengths. *Geophys. Res. Lett.* 31.

- Milani, A., A. M. Nobili, and P. Farinella (1987). *Non-gravitational perturbations and satellite geodesy*. Adam Hilger Ltd., Bristol, UK.
- Milani, A. and G. Gronchi (2010). *Theory of Orbit Determination*. Cambridge University Press.
- Montenbruck, O. and E. Gill (2001). *Satellite Orbits*. Springer Berlin Heidelberg.
- Morinelli, P. J., J. Socoby, S. Hendry, and R. Campion (2010). Tracking Data Certification for the Lunar Reconnaissance Orbiter. In: *Proceedings of the SpaceOps 2010 Conference*. Huntsville, Alabama, pp. 1–16. URL: <http://arc.aiaa.org/doi/pdf/10.2514/6.2010-2129>.
- Moyer, T. (1971). Techn. Report 32-1527, NASA, Jet Propulsion Lab., California Inst. Technology, Pasadena, California.
- Moyer, T. D. (2000). *Formulation for Observed and Computed Values of Deep Space Network Data Types for Navigation*. Ed. by J. H. Yuen. Vol. 2. Deep Space Communications and Navigation Series. Hoboken, NJ, USA: John Wiley & Sons, Inc. URL: http://www.dm.unipi.it/cluster-pages/tommey/mc/Descanso2_Moyer.pdf.
- Namiki, N., H. Hanada, T. Tsubokawa, N. Kawano, M. Ooe, K. Heki, T. Iwata, M. Ogawa, and T. Takano (1999). Selenodetic experiments of SELENE: relay subsatellite, differential VLBI and laser altimeter. *Adv. Sp. Res.* 23(11), pp. 1817–1820.
- Nerem, R. S. and J. Wahr (2011). Recent changes in the Earth’s oblateness driven by Greenland and Antarctic ice mass loss. *Geophys. Res. Lett.* 38(13), pp. 1–6.
- Noll, C. E. (2010). The crustal dynamics data information system: A resource to support scientific analysis using space geodesy. *Adv. Sp. Res.* 45(12), pp. 1421–1440.
- Otsubo, T. and G. M. Appleby (2003). System-dependent center-of-mass correction for spherical geodetic satellites. *J. Geophys. Res.* 108 (B4).
- Park, R. S., D. J. Scheeres, G. Giampieri, J. M. Longuski, and E. Fischbach (2005). Estimating Parameterized Post-Newtonian Parameters from Spacecraft Radiometric Tracking Data. *J. Spacecr. Rockets* 42(3), pp. 559–568.
- Park, R., S. W. Asmar, E. G. Fahnestock, A. S. Konopliv, W. Lu, and M. M. Watkins (2012). Gravity Recovery and Interior Laboratory Simulations of Static and Temporal Gravity Field. *J. Spacecr. Rockets* 49(2), pp. 390–400.
- Pavlis, E. C. (2009). *SLRF2008: The IERS Reference Frame for SLR POD Contributed to ITRF2008*. URL: <http://www.aviso.altimetry.fr/fileadmin/documents/OSTST/2009/oral/Pavlis.pdf>.

- Pearlman, M. R., J. J. Degnan, and J. M. Bosworth (2002). The International Laser Ranging Service. *Adv. Sp. Res.* 30(2), pp. 135–143.
- Peters, T., J. Müller, and N. Sneeuw (2002). Temporal variations in the Earth's gravity field with emphasis on atmospheric effects. In: *Vorträge beim 4. DFG-Rundgespräch im Rahmen des Forschungsvorhabens 'Rotation der Erde', DGK, Reihe A, Heft 118*. Ed. by H. Schuh, M. Soffel, and H. Hornik. Verlag der Bayerischen Akademie der Wissenschaften, pp. 133–140.
- Petit, G. and B. Luzum, eds. (2010). *IERS Conventions (2010)*. IERS Technical Note 36. Verlag des Bundesamts für Kartographie und Geodäsie, Frankfurt am Main, p. 179. URL: <http://www.iers.org/IERS/EN/Publications/TechnicalNotes/tn36.html>.
- Pfister, H. (2007). On the history of the so-called Lense-Thirring effect. *Gen. Relativ. Gravit.* 39, pp. 1735–1748.
- Phillips, D. L. (1962). A technique for the numerical solution of certain integral equations of the first kind. *Journal of the ACM* 9, pp. 84–97.
- Picone, J. M., A. Hedin, D. Drob, and A. Aikin (2002). NRLMSISE-00 empirical model of the atmosphere: Statistical comparisons and scientific issues. *J. Geophys. Res.* 107(A12).
- Ray, R. (1999). *A Global Ocean Tide model from TOPEX/Poseidon Altimetry, GOT99.2*. NASA/TM-1999-209478, 58MD. Goddard Space Flight Center, NASA, Greenbelt. URL: http://denali.gsfc.nasa.gov/personal_pages/ray/MiscPubs/19990089548_1999150788.pdf.
- Reigber, C. (2002). CHAMP mission status. *Adv. Sp. Res.* 30(2), pp. 129–134.
- Ries, J. C., C. Huang, and M. M. Watkins (1988). Effect of General Relativity on a Near-Earth Satellite in the Geocentric and Barycentric Reference Frames. *Phys. Rev. Lett.* 61(8), pp. 903–906.
- Ries, J. C., C. K. Shum, and B. D. Tapley (1993). Surface Force Modeling for Precision Orbit Determination. In: *Environmental Effects on Spacecraft Positioning and Trajectories*. Ed. by A. V. Jones. Vol. 73. Geophys. Monogr. Ser. Washington, D. C: American Geophysical Union, pp. 111–124.
- Rim, H. and B. Schutz (2002). *Precision Orbit Determination (POD)*. Geoscience Laser Altimeter System (GLAS), Algorithm Theoretical Basis Document Version 2.2. URL: http://www.csr.utexas.edu/glas/pdf/atbd_pod_10_02.pdf.
- Rowlands, D. D., R. D. Ray, D. S. Chinn, and F. G. Lemoine (2002). Short-arc analysis of intersatellite tracking data in a gravity mapping mission. *J. Geod.* 76(6-7), pp. 307–316.

- Rowlands, D. D., F. G. Lemoine, D. S. Chinn, and S. B. Luthcke (2009). A simulation study of multi-beam altimetry for lunar reconnaissance orbiter and other planetary missions. *J. Geod.* 83(8), pp. 709–721.
- Rudenko, S., D. Dettmering, S. Esselborn, T. Schöne, C. Förste, J.-M. Lemoine, M. Ablain, D. Alexandre, and K.-H. Neumayer (2014). Influence of time variable geopotential models on precise orbits of altimetry satellites, global and regional mean sea level trends. *Adv. Sp. Res.* 54(1), pp. 92–118.
- Saylor, R., C. Peddie, M. B. Houghton, M. Kohout, J. McGarry, J. Clapsadle, O. Hsu, J. Murphy, R. Lamb, M. Mesarch, S. Scott, M. Hillyard, M. J. Golightly, C. Avis, M. Sullivan, K. Harshman, M. Torrence, J. Parker, E. Bowman-Cisneros, D. Waters, R. Casasanta, M. Blau, S. Snell, and R. Kolecki (2009). *Lunar Reconnaissance Orbiter Flight Operations Review (FOR)*. URL: <http://snebulos.mit.edu/projects/crater/docs/presentations/mission-for.pdf>.
- Seeber, G. (2003). *Satellite Geodesy*. 2nd edition. Walter de Gruyter Berlin New York 2003.
- Sinclair, A. (1997). *Data screening and normal point formation: a re-statement of Herstmonceux normal point recommendation*. URL: http://ilrs.gsfc.nasa.gov/data_and_products/data/npt/npt_algorithm.html.
- Smith, D., M. Zuber, F. Lemoine, M. Torrence, and E. Mazarico (2008). *Orbit Determination of LRO at the Moon*. Presented at the 16th International Workshop on Laser Ranging, Poznań, Poland. URL: http://cddis.gsfc.nasa.gov/lw16/docs/papers/sci_2_Smith_p.pdf.
- Smith, D. E., M. T. Zuber, G. B. Jackson, J. F. Cavanaugh, G. A. Neumann, H. Riris, X. Sun, R. S. Zellar, C. Coltharp, J. Connelly, R. B. Katz, I. Kleyner, P. Liiva, A. Matuszeski, E. M. Mazarico, J. F. McGarry, A.-M. Novo-Gradac, M. N. Ott, C. Peters, L. A. Ramos-Izquierdo, L. Ramsey, D. D. Rowlands, S. Schmidt, V. S. Scott, G. B. Shaw, J. C. Smith, J.-P. Swinski, M. H. Torrence, G. Unger, A. W. Yu, and T. W. Zagwodzki (2010). The Lunar Orbiter Laser Altimeter Investigation on the Lunar Reconnaissance Orbiter Mission. *Space Sci. Rev.* 150(1-4), pp. 209–241.
- Sośnica, K., D. Thaller, R. Dach, A. Jäggi, and G. Beutler (2011). *Availability of SLR Normal Points at ILRS Data Centers*. Presented at the 17th International Workshop on Laser Ranging, Bad Kötzing, Germany. URL: http://www.bernese.unibe.ch/publist/publist_2011.php.
- Sośnica, K., D. Thaller, A. Jäggi, R. Dach, C. Baumann, and G. Beutler (2012). *Can we improve LAGEOS solutions by combining with LEO satellites?* Presented at the International Technical Laser Ranging Workshop. URL: http://www.lnf.infn.it/conference/laser2012/2tuesday/3_4_8sosnica/sosnica_p.pdf.

- Sośnica, K. J. (2014). Determination of Precise Satellite Orbits and Geodetic Parameters using Satellite Laser Ranging. PhD thesis. University of Bern. URL: http://www.bernese.unibe.ch/publist/publist_2014.php#thesis.
- Sośnica, K. J., A. Jäggi, M. Weigelt, U. Meyer, T. van Dam, N. Zehentner, and T. Mayer-Gürr (2014). *Time varying gravity from SLR and combined SLR and high-low satellite-to-satellite tracking data*. Presented at the GRACE Science Team Meeting, Potsdam, Germany. URL: http://www.bernese.unibe.ch/publist/2014/pres/KS_GRACE-SLR.pdf.
- Standish, E. M., X. X. Newhall, J. G. Williams, and W. M. Folkner (1995). *JPL Planetary and Lunar Ephemerides, DE403/LE403*.
- Sun, X., D. Skillman, J. McGarry, G. Neumann, D. Mao, M. Torrence, and E. Hoffman (2013). Time Transfer between Satellite Laser Ranging Stations via Simultaneous Laser Ranging to the Lunar Reconnaissance Orbiter. In: *Proceedings of the 18th International Workshop on Laser Ranging*. Fujiyoshida, Japan. URL: <http://space-geodesy.nasa.gov/docs/2013/13-Po54-Sun.pdf>.
- Svehla, D. and M. Rothacher (2005). Kinematic precise orbit determination for gravity field determination. In: *A Window on the Future of Geodesy, IAG Symposia*. Ed. by F. Sans. Vol. 128. Springer, pp. 181–188.
- Tapley, B. D. (1973). Statistical orbit determination theory. *Recent Adv. Dyn. Astron.* 39, pp. 396–425.
- Tapley, B. D., J. C. Ries, G. W. Davis, R. J. Eanes, B. E. Schutz, C. K. Shum, M. M. Watkins, J. A. Marshall, R. S. Nerem, B. H. Putney, S. M. Klosko, S. B. Luthcke, D. Pavlis, R. G. Williamson, and N. P. Zelensky (1994). Precision orbit determination for TOPEX/POSEIDON. *J. Geophys. Res.* 99(C12), pp. 24,383–24,404.
- Tapley, B. D., S. Bettadpur, M. Watkins, and C. Reigber (2004a). The gravity recovery and climate experiment: Mission overview and early results. *Geophys. Res. Lett.* 31(9).
- Tapley, B. D., B. E. Schutz, and G. H. Born (2004b). *Statistical Orbit Determination*. Elsevier.
- Tikhonov, A. N. (1963). Solution of incorrectly formulated problems and the regularization method. *Soviet Math. Dokl.* 4, pp. 1035–1038.
- Tooley, C. (2006). *Lunar Reconnaissance Orbiter Spacecraft & Objectives*. Presented at the AIAA-Houston Annual Technical Symposium. URL: <http://lunar.gsfc.nasa.gov/library/tooley-scoobjectives-51906.pdf>.
- Ullman, R. E. (1994). *SOLVE Program: Mathematical formulation and guide to user input*. Hughes/STX contractor report, contract NAS5-31760. NASA Goddard Space Flight Center, Greenbelt, Maryland.

- Vallado, D. A. and D. Finkleman (2008). A Critical Assessment of Satellite Drag and Atmospheric Density Modeling. In: *Proceedings of the AIAA/AAS Astrodynamics Specialist Conference*. Honolulu, USA. URL: <http://www.agi.com/downloads/resources/white-papers/A-Critical-Assessment-of-Satellite-Drag-and-Atmospheric-Density-Modeling.pdf>.
- Weigelt, M., N. Sneeuw, E. Schrama, and P. Visser (2013). An improved sampling rule for mapping geopotential functions of a planet from a near polar orbit. *Journal of Geodesy* 87(2), pp. 127–142.
- Williams, J. G. and J. O. Dickey (2002). Lunar Geophysics, Geodesy, and Dynamics. In: *Proceedings of the 13th International Workshop on Laser Ranging*. Washington, D.C., pp. 1–17. URL: http://ilrs.gsfc.nasa.gov/docs/williams_lw13.pdf.
- Yoder, C. F., J. G. Williamson, J. O. Dickey, B. E. Schutz, R. J. Eanes, and B. D. Tapley (1983). Secular variation of Earth’s gravitational harmonic J2 coefficient from Lageos and nontidal acceleration of Earth rotation. *Nature* 303, pp. 757–762.
- Yunck, T. P. (1993). Coping with the Atmosphere and Ionosphere in Precise Satellite and Ground Positioning. In: *Environmental Effects on Spacecraft Positioning and Trajectories*. Geophysical Monograph 73, IUGG Volume 13.
- Zandbergen, R., M. Otten, P. L. Righetti, D. Kuijper, and J. M. Dow (2003). Routine operational and high-precision orbit determination of ENVISAT. *Adv. Sp. Res.* 31(8), pp. 1953–1958.
- Zuber, M. T., D. E. Smith, R. S. Zellar, G. A. Neumann, X. Sun, R. B. Katz, I. Kleyner, A. Matuszeski, J. F. McGarry, M. N. Ott, L. A. Ramos-Izquierdo, D. D. Rowlands, M. H. Torrence, and T. W. Zagwodzki (2010). The Lunar Reconnaissance Orbiter Laser Ranging Investigation. *Space Sci. Rev.* 150, pp. 63–80.
- Zuber, M. T., D. E. Smith, M. M. Watkins, S. W. Asmar, A. S. Konopliv, F. G. Lemoine, H. J. Melosh, G. A. Neumann, R. J. Phillips, S. C. Solomon, M. A. Wieczorek, J. G. Williams, S. J. Goossens, G. Kruizinga, E. Mazarico, R. S. Park, and D.-N. Yuan (2013). Gravity field of the Moon from the Gravity Recovery and Interior Laboratory (GRAIL) mission. *Science* 339(6120), pp. 668–71.

Appendices

Appendix A

Computation of the light time τ

The computation of the light travel times starts at the final received time, t , which is assumed to be known, and proceeds backwards until the model is complete: whereas one-way measurements require the computation of only one light travel time (downlink), two-way measurements require the computation of two light travel times (downlink and uplink). Table A.1 illustrates the iteration process for the computation of the downlink light travel time, τ_d , between ground station, \mathbf{r}_{stat} , and satellite, \mathbf{r} , for geodetic satellites. All position vectors are given in the geocentric reference frame. More details to the relativistic correction term can be found in Section 2.2.5. Convergence is met when $\tau_d^{(n)} - \tau_d^{(n-1)} < 1 \times 10^{-8}$ seconds. The computation of the uplink light travel time, τ_u , is done in an analogous manner.

For the computation of the downlink and uplink light travel time for the Lunar Reconnaissance Orbiter (LRO) satellite, some changes must be made regarding Table A.1. First, all position vectors have to refer to a solar-system barycentric reference frame (cf. Section 2.2.5). Second, the relativistic light time correction is defined differently (column 3 of Table A.1 has to be replaced with Equation 2.65).

Table A.1: Computation of the downlink light travel time for geodetic satellites

iteration #	ρ_d	$\Delta\rho_{\text{rel}}$	τ_d
1	$\rho_d^{(1)} = \ \mathbf{r}(t) - \mathbf{r}_{\text{stat}}(t)\ $	$\Delta\rho_{\text{rel}}^{(1)} = 2 \frac{GM_{\oplus}}{c^2} \ln \frac{\ \mathbf{r}_{\text{stat}}(t)\ + \ \mathbf{r}(t)\ + \rho_d^{(1)}}{\ \mathbf{r}_{\text{stat}}(t)\ + \ \mathbf{r}(t)\ - \rho_d^{(1)}}$	$\tau_d^{(1)} = \frac{\rho_d^{(1)}}{c} + \frac{\Delta\rho_{\text{rel}}^{(1)}}{c}$
2	$\rho_d^{(2)} = \left\ \mathbf{r} \left(t - \tau_d^{(1)} \right) - \mathbf{r}_{\text{stat}}(t) \right\ $	$\Delta\rho_{\text{rel}}^{(2)} = 2 \frac{GM_{\oplus}}{c^2} \ln \frac{\ \mathbf{r}_{\text{stat}}(t)\ + \ \mathbf{r}(t - \tau^{(1)})\ + \rho_d^{(2)}}{\ \mathbf{r}_{\text{stat}}(t)\ + \ \mathbf{r}(t - \tau^{(1)})\ - \rho_d^{(2)}}$	$\tau_d^{(2)} = \frac{\rho_d^{(2)}}{c} + \frac{\Delta\rho_{\text{rel}}^{(2)}}{c}$
\vdots			
n	$\rho_d^{(n)} = \left\ \mathbf{r} \left(t - \tau_d^{(n-1)} \right) - \mathbf{r}_{\text{stat}}(t) \right\ $	$\Delta\rho_{\text{rel}}^{(n)} = 2 \frac{GM_{\oplus}}{c^2} \ln \frac{\ \mathbf{r}_{\text{stat}}(t)\ + \ \mathbf{r}(t - \tau^{(n-1)})\ + \rho_d^{(n)}}{\ \mathbf{r}_{\text{stat}}(t)\ + \ \mathbf{r}(t - \tau^{(n-1)})\ - \rho_d^{(n)}}$	$\tau_d^{(n)} = \frac{\rho_d^{(n)}}{c} + \frac{\Delta\rho_{\text{rel}}^{(n)}}{c}$

Appendix B

Weighting SLR measurements

For a time span of five years (January 2006 to December 2010), the impact of using the bin Root Mean Square (RMS), given in the Normal Point (NP) files for each observation, instead of assigning all observations equal weights was tested. Figure B.1 shows the variation of the degree-two gravity field coefficients for these two weighting types. Whereas there are no noticeable differences in the variations of C_{20} , the variations of all other degree-two terms tend to be larger using the bin RMS. This is why equal weights were assigned to the laser observations.

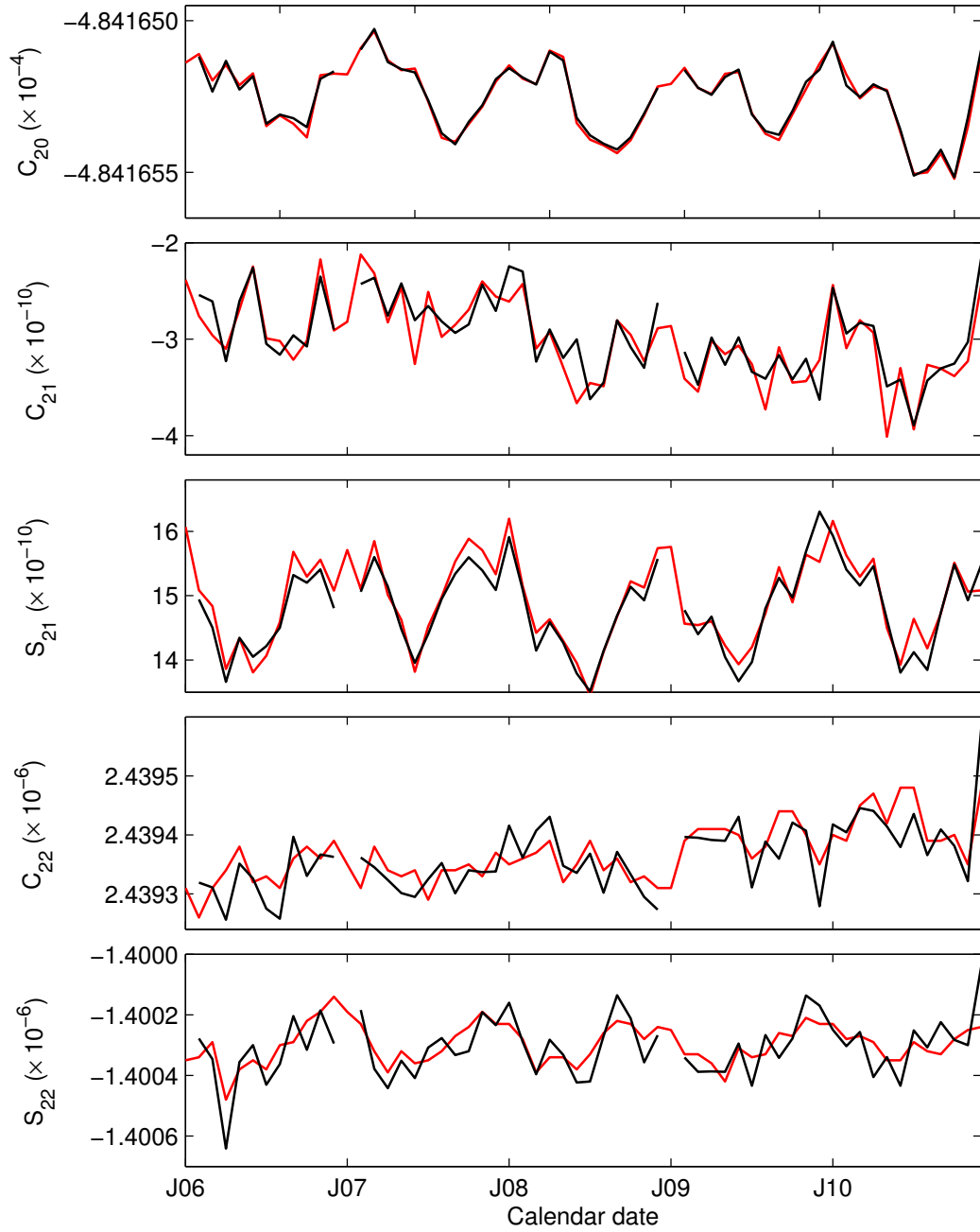


Figure B.1: Monthly gravity field coefficients of degree 2. The gravity field solution in red color is based on equally weighted observations. For the solution in black the bin RMS, which is available for each NP, was used to weight the observations.

Appendix C

LRO

C.1 Maneuvers

The binary SPK files provided by the Navigation and Ancillary Information Facility (NAIF) and computed at the Goddard Space Flight Center (GSFC), which contain ephemeris data of the Lunar Reconnaissance Orbiter (LRO), were downloaded from <http://imbrium.mit.edu/LRORS/DATA/SPK/>. One SPK file covers one science mission phase¹. Gaps in the coverage exist because around maneuvers the trajectory was not reconstructed. Type and duration of maneuvers were extracted from the SPK files using the command line tool COMMNT provided by NAIF. Table C.1 contains a list of performed maneuvers including Station Keeping (SK) maneuvers (the letters ‘a’ and ‘b’ denote first and second burn), delta-H (dH) maneuvers, and yaw flips during the nominal and the science mission phase². SK maneuvers are numbered in a continuous manner.

Table C.1: List of maneuvers for the nominal and the science mission phase.

maneuver	type	from	to
	dH	25 Sep 2009 15:45:00.00	25 Sep 2009 15:45:00.00
SK01a		25 Sep 2009 18:27:56.00	25 Sep 2009 18:29:28.00
SK01b		26 Sep 2009 17:55:25.00	26 Sep 2009 17:56:46.60
yaw flip	to +X	26 Sep 2009 17:56:46.60	26 Sep 2009 18:45:00.00
	dH	05 Oct 2009 21:55:00.00	05 Oct 2009 21:55:00.00
SK02a		23 Oct 2009 14:28:29.47	23 Oct 2009 14:30:01.79
SK02b		23 Oct 2009 17:21:28.33	23 Oct 2009 17:23:05.39

Continued on next page

¹a science mission phase spans approximately four weeks

²a yaw flip to -X in March 2011 is missing

Table C.1: (continued)

maneuver type		from				to			
	dH	06	Nov	2009	14:10:00.00	06	Nov	2009	14:10:00.00
	SK03a	20	Nov	2009	14:05:07.00	20	Nov	2009	14:06:29.60
	SK03b	20	Nov	2009	16:54:53.00	20	Nov	2009	16:56:28.80
	dH	04	Dec	2009	16:05:00.00	04	Dec	2009	16:09:00.00
	SK04a	17	Dec	2009	18:16:08.50	17	Dec	2009	18:17:33.90
	SK04b	17	Dec	2009	21:08:23.50	17	Dec	2009	21:09:51.50
	dH	30	Dec	2009	17:15:00.00	30	Dec	2009	17:15:00.00
	SK05a	13	Jan	2010	16:50:58.50	13	Jan	2010	16:52:23.90
	SK05b	13	Jan	2010	19:41:59.70	13	Jan	2010	19:43:26.50
	dH	28	Jan	2010	13:40:00.00	28	Jan	2010	13:40:00.00
	SK06a	09	Feb	2010	15:24:28.70	09	Feb	2010	15:25:52.70
	SK06b	09	Feb	2010	18:18:24.70	09	Feb	2010	18:19:57.10
	dH	23	Feb	2010	16:43:00.50	23	Feb	2010	16:48:28.70
	dH	09	Mar	2010	13:15:00.60	09	Mar	2010	13:24:01.90
	SK07a	09	Mar	2010	14:29:13.60	09	Mar	2010	14:30:32.60
	SK07b	09	Mar	2010	17:22:28.60	09	Mar	2010	17:23:56.10
	dH	23	Mar	2010	15:49:00.60	23	Mar	2010	15:56:35.40
yaw flip to	-X	30	Mar	2010	19:20:00.00	30	Mar	2010	19:51:00.00
	dH	05	Apr	2010	15:00:00.70	05	Apr	2010	15:05:15.90
	SK08a	05	Apr	2010	16:54:50.90	05	Apr	2010	16:56:14.50
	SK08b	05	Apr	2010	19:48:21.40	05	Apr	2010	19:49:46.40
	dH	19	Apr	2010	14:26:00.80	19	Apr	2010	14:33:38.00
	dH	03	May	2010	14:20:00.90	03	May	2010	14:27:11.90
	SK09a	03	May	2010	15:59:54.10	03	May	2010	16:01:24.50
	SK09b	03	May	2010	18:52:54.90	03	May	2010	18:54:18.70
	dH	17	May	2010	14:20:00.90	17	May	2010	14:25:33.70
	dH	30	May	2010	14:15:01.00	30	May	2010	14:20:57.00
	SK10a	30	May	2010	16:25:06.20	30	May	2010	16:26:29.80
	SK10b	30	May	2010	19:20:56.20	30	May	2010	19:22:16.20
	dH	14	Jun	2010	17:15:01.10	14	Jun	2010	17:18:19.70
	dH	27	Jun	2010	15:00:00.20	27	Jun	2010	15:02:34.20
	SK11a	27	Jun	2010	17:15:52.40	27	Jun	2010	17:17:18.00
	SK11b	27	Jun	2010	20:10:35.40	27	Jun	2010	20:11:59.20
	dH	24	Jul	2010	13:15:00.30	24	Jul	2010	13:19:00.30
	SK12a	24	Jul	2010	15:41:54.30	24	Jul	2010	15:43:20.20
	SK12b	24	Jul	2010	18:39:35.60	24	Jul	2010	18:40:59.10
	dH	06	Aug	2010	14:35:00.50	06	Aug	2010	14:37:40.30
	dH	20	Aug	2010	10:10:00.50	20	Aug	2010	10:15:54.50
	SK13a	20	Aug	2010	12:18:46.70	20	Aug	2010	12:20:11.90

Continued on next page

Table C.1: (continued)

maneuver type	from		to	
	SK13b	20 Aug 2010 15:14:10.50	20 Aug 2010 15:15:32.30	
	dH	03 Sep 2010 15:35:00.60	03 Sep 2010 15:39:47.80	
	dH	16 Sep 2010 16:15:00.70	16 Sep 2010 16:22:06.90	
	SK14a	16 Sep 2010 18:15:39.70	16 Sep 2010 18:17:09.90	
	SK14b	16 Sep 2010 21:10:23.90	16 Sep 2010 21:11:46.70	
yaw flip	to +X	29 Sep 2010 18:00:00.80	29 Sep 2010 18:30:11.80	
	dH	30 Sep 2010 15:00:00.80	30 Sep 2010 15:04:50.80	
	dH	14 Oct 2010 15:00:00.90	14 Oct 2010 15:07:33.30	
	SK15a	14 Oct 2010 17:20:56.10	14 Oct 2010 17:22:41.40	
	SK15b	14 Oct 2010 20:15:49.10	14 Oct 2010 20:17:14.30	
	dH	27 Oct 2010 17:17:00.90	27 Oct 2010 17:22:41.40	
	dH	10 Nov 2010 22:10:01.00	10 Nov 2010 22:15:30.00	
	SK16a	10 Nov 2010 23:10:51.20	10 Nov 2010 23:12:14.90	
	SK16b	11 Nov 2010 02:05:18.10	11 Nov 2010 02:06:41.60	
	dH	22 Nov 2010 13:46:01.00	22 Nov 2010 13:50:39.70	
	dH	07 Dec 2010 11:50:00.20	07 Dec 2010 11:54:06.80	
	SK17a	07 Dec 2010 14:11:43.20	07 Dec 2010 14:13:00.00	
	SK17b	07 Dec 2010 17:06:55.20	07 Dec 2010 17:08:22.60	
	dH	19 Dec 2010 19:40:00.30	19 Dec 2010 19:42:21.50	
	dH	03 Jan 2010 16:35:00.40	03 Jan 2010 16:36:20.60	
	SK18a	03 Jan 2010 17:48:35.40	03 Jan 2010 17:50:01.00	
	SK18a	03 Jan 2010 20:43:22.60	03 Jan 2010 20:44:41.20	
	dH	18 Jan 2010 14:00:00.50	18 Jan 2010 14:02:55.30	
	dH	31 Jan 2010 18:45:00.60	31 Jan 2010 18:48:05.80	
	SK19a	31 Jan 2010 20:36:20.70	31 Jan 2010 20:37:40.10	
	SK19a	31 Jan 2010 23:26:40.50	31 Jan 2010 23:28:01.70	
	dH	14 Feb 2011 18:05:00.70	14 Feb 2011 18:07:37.70	
	dH	27 Feb 2011 13:35:00.70	27 Feb 2011 13:39:27.50	
	SK20a	27 Feb 2011 15:12:17.70	27 Feb 2011 15:13:37.90	
	SK20b	27 Feb 2011 18:08:50.70	27 Feb 2011 18:10:10.30	
	dH	14 Mar 2011 20:55:00.70	14 Mar 2011 21:01:43.90	
	dH	26 Mar 2011 11:25:00.70	26 Mar 2011 11:30:38.10	
	SK21a	26 Mar 2011 13:51:35.70	26 Mar 2011 13:52:54.70	
	SK21b	26 Mar 2011 16:49:00.70	26 Mar 2011 16:50:24.50	
	dH	05 Apr 2011 18:50:00.80	05 Apr 2011 18:58:20.00	
	dH	08 Apr 2011 14:53:00.80	08 Apr 2011 14:55:15.60	
	dH	22 Apr 2011 13:30:00.80	22 Apr 2011 13:38:27.30	
	SK22a	22 Apr 2011 15:51:26.80	22 Apr 2011 15:52:54.70	
	SK22b	22 Apr 2011 18:47:03.80	22 Apr 2011 18:48:21.50	

Continued on next page

Table C.1: (continued)

maneuver type	from			to		
dH	07	May	2011 19:40:00.90	07	May	2011 19:44:59.40
dH	20	May	2011 14:55:01.00	20	May	2011 14:59:31.00
SK23a	20	May	2011 16:57:00.00	20	May	2011 16:58:19.70
SK23b	20	May	2011 19:48:54.00	20	May	2011 19:50:13.00
dH	02	Jun	2011 17:50:01.10	02	Jun	2011 17:53:40.90
dH	16	Jun	2011 13:15:00.21	16	Jun	2011 13:17:22.41
SK24a	16	Jun	2011 15:24:12.21	16	Jun	2011 15:25:30.21
SK24b	16	Jun	2011 18:21:16.41	16	Jun	2011 18:22:33.01
dH	30	Jun	2011 22:30:00.30	30	Jun	2011 22:32:56.30
dH	13	Jul	2011 12:22:00.40	13	Jul	2011 12:23:35.40
SK25a	13	Jul	2011 13:56:39.40	13	Jul	2011 13:57:59.60
SK25b	13	Jul	2011 16:53:22.60	13	Jul	2011 16:54:42.00
dH	27	Jul	2011 12:30:00.50	27	Jul	2011 12:32:59.30
dH	10	Aug	2011 11:20:00.50	10	Aug	2011 11:23:05.70
SK26a	10	Aug	2011 13:04:53.80	10	Aug	2011 13:07:09.90
SK26b	10	Aug	2011 15:55:24.70	10	Aug	2011 15:57:42.10
dH	24	Aug	2011 13:25:00.60	24	Aug	2011 13:29:00.20
dH	31	Aug	2011 16:50:00.40	31	Aug	2011 16:53:15.90
dH	06	Sep	2011 15:14:00.70	06	Sep	2011 15:19:29.30
SK27a	06	Sep	2011 17:16:16.70	06	Sep	2011 17:16:55.70
SK27b	06	Sep	2011 20:32:52.70	06	Sep	2011 20:33:22.30
dH	13	Sep	2011 16:55:00.76	13	Sep	2011 17:01:04.36
dH	20	Sep	2011 19:35:00.80	20	Sep	2011 19:38:58.00
yaw flip to +X	27	Sep	2011 13:00:00.00	27	Sep	2011 13:30:11.00
dH	28	Sep	2011 17:30:00.80	28	Sep	2011 17:32:07.20
dH	03	Oct	2011 15:50:00.90	03	Oct	2011 15:53:30.90
SK28a	03	Oct	2011 17:48:35.10	03	Oct	2011 17:49:50.30
SK28b	03	Oct	2011 20:46:44.90	03	Oct	2011 20:48:03.90
dH	11	Oct	2011 16:17:00.90	11	Oct	2011 16:20:17.10
dH	17	Oct	2011 18:20:01.00	17	Oct	2011 18:22:29.00
dH	24	Oct	2011 20:00:01.00	24	Oct	2011 20:03:15.80
dH	31	Oct	2011 14:50:01.00	31	Oct	2011 14:52:04.20
SK29a	31	Oct	2011 17:03:50.20	31	Oct	2011 17:05:18.00
SK29b	31	Oct	2011 19:55:09.20	31	Oct	2011 19:57:25.80
dH	14	Nov	2011 13:40:01.10	14	Nov	2011 13:43:42.10
dH	27	Nov	2011 12:10:01.20	27	Nov	2011 12:12:17.80
SK30a	27	Nov	2011 13:53:55.40	27	Nov	2011 13:54:48.40
SK30b	27	Nov	2011 16:44:59.20	27	Nov	2011 16:45:27.00
dH	11	Dec	2011 11:55:00.30	11	Dec	2011 11:56:33.50

Continued on next page

Table C.1: (continued)

maneuver type	from		to	
SK31a	11 Dec 2011	13:00:20.50	11 Dec 2011	13:07:43.90
SK31b	11 Dec 2011	16:02:58.80	11 Dec 2011	16:03:28.10
dH	23 Dec 2011	15:10:00.30	23 Dec 2011	15:13:43.50
dH	10 Jan 2012	12:30:00.50	10 Jan 2012	12:31:45.90
dH	10 Jan 2012	12:30:00.50	10 Jan 2012	12:31:45.90
dH	24 Jan 2012	16:50:00.50	24 Jan 2012	16:54:53.30
dH	17 Feb 2012	12:40:00.70	17 Feb 2012	12:43:42.30
dH	28 Feb 2012	20:45:00.80	28 Feb 2012	20:48:49.60
dH	15 Mar 2012	15:55:00.80	15 Mar 2012	15:57:38.40
dH	15 Mar 2012	15:55:00.80	15 Mar 2012	15:57:38.40
yaw flip to -X	19 Mar 2012	11:05:00.00	19 Mar 2012	11:35:11.00
dH	27 Mar 2012	15:50:00.91	27 Mar 2012	15:52:37.82
dH	11 Apr 2012	15:15:01.00	11 Apr 2012	15:18:17.00
dH	11 Apr 2012	15:15:01.00	11 Apr 2012	15:18:17.00
dH	24 Apr 2012	16:55:01.10	24 Apr 2012	16:59:08.10
dH	08 May 2012	14:30:01.20	08 May 2012	14:32:24.80
dH	08 May 2012	14:30:01.20	08 May 2012	14:32:24.80
dH	30 May 2012	15:40:00.30	30 May 2012	15:43:19.30
dH	30 May 2012	15:40:00.30	30 May 2012	15:43:19.30
dH	26 Jun 2012	14:45:00.50	26 Jun 2012	14:47:54.10
dH	26 Jul 2012	13:10:00.60	26 Jul 2012	13:13:24.40
dH	26 Jul 2012	13:10:00.60	26 Jul 2012	13:13:24.40
dH	15 Aug 2012	17:20:00.70	15 Aug 2012	17:22:13.30
dH	29 Aug 2012	15:55:00.80	29 Aug 2012	15:59:21.20
dH	29 Aug 2012	15:55:00.80	29 Aug 2012	15:59:21.20
dH	12 Sep 2012	20:03:01.00	12 Sep 2012	20:07:26.20

C.2 Dimensional layouts

The dimensional layouts of LRO are depicted in Figures C.1 and C.2. They are essential to derive the antenna offset (coordinates of the antenna w.r.t the center of figure) and the center of mass offset (coordinates of center of mass w.r.t. the center of figure). Hence, center of figure and center of mass have to be known. The latter depends mainly on the orientation of the Solar Array (SA). Further, fuel decreases with time, causing a shift of the center of mass. The assumption is made, however, that the center of mass remains fixed at the center of the main spacecraft bus (cf. Figure C.2). The

center of figure (or the origin of the spacecraft bus frame) is at the center of the spacecraft/launch vehicle interface. The exact location though is not known to the author. The assumed center of figure is shown in Figure C.2. It is possible that the assumed center of figure differs from the ‘true’ center of figure by up to a few decimeters. This is not thought to be critical, however, since the center of figure differs from the center of mass solely in the x-component, which is aligned with the along track direction of the spacecraft reference system. The empirical accelerations estimated in along track direction are expected to absorb possible deficiencies in the assumed location of the center of figure.

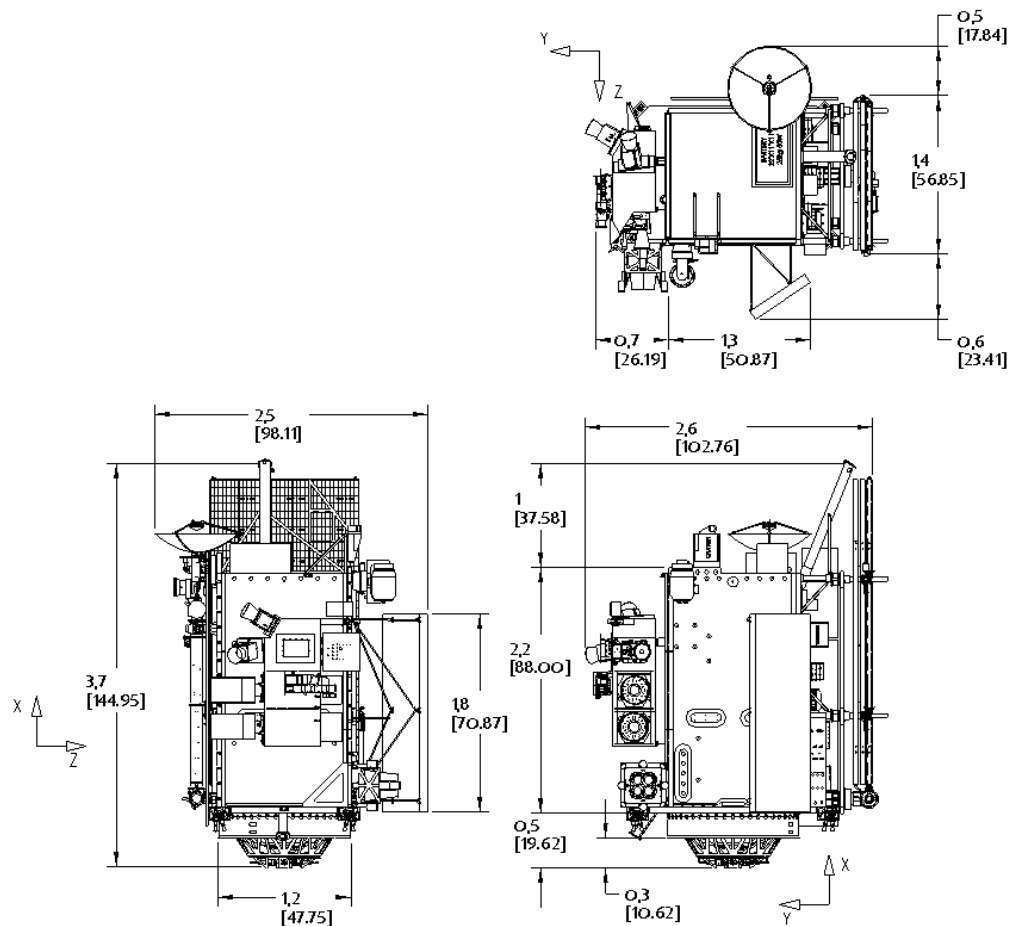


Figure C.1: Dimensional layout of LRO (stowed) from Tooley (2006). The dimensions are given in meters and inches (square brackets).

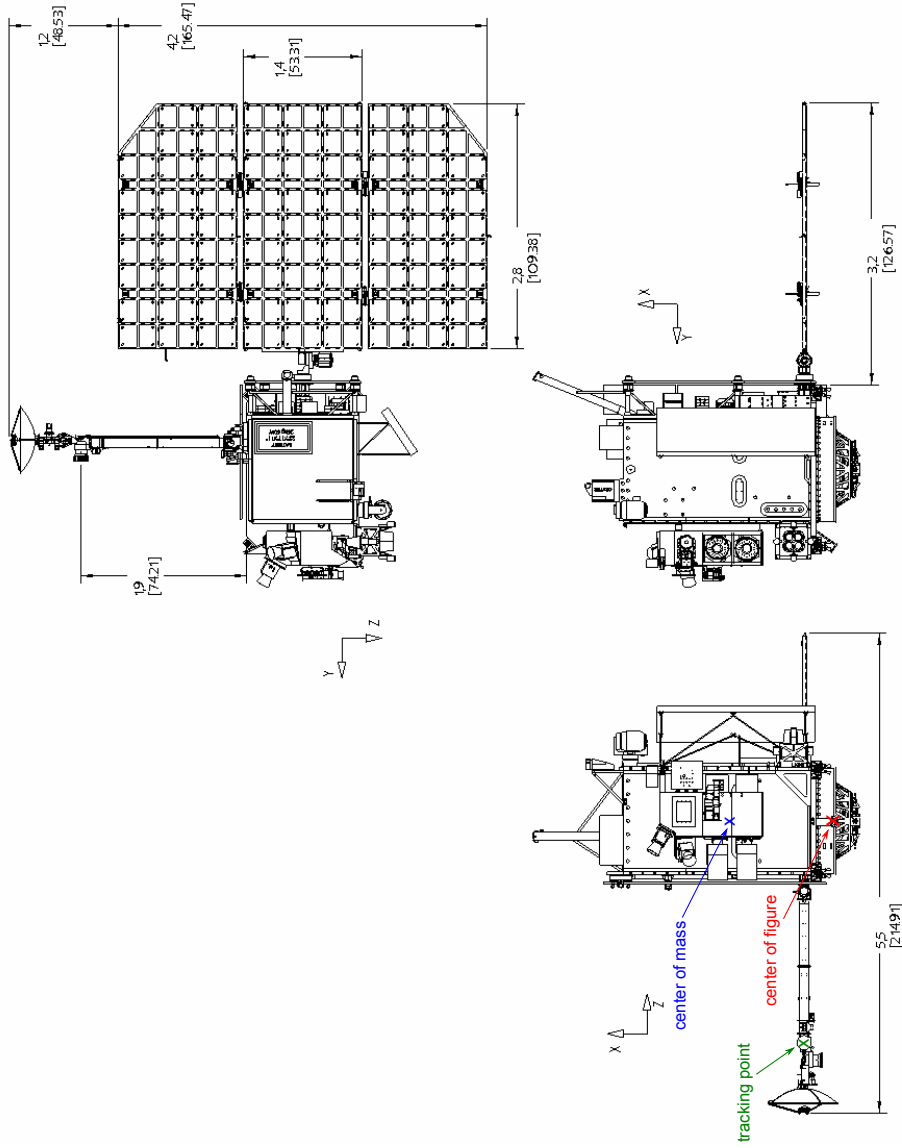


Figure C.2: Dimensional layout of LRO (deployed) from Tooley (2006). The assumed center of figure and center of mass are indicated as well as the assumed tracking point of the high gain antenna.

Appendix D

Raw data conversions

D.1 From NPs to GEODYN format

The Normal Point (NP) files, which are available in the Consolidated Laser Ranging Data Format (CRD)¹, were retrieved from the Crustal Dynamics Data Information System (CDDIS)² for the geodetic satellites and from the Planetary Data System (PDS)³ for the Lunar Reconnaissance Orbiter (LRO). The files contain information such as the light travel time, the number of raw ranges a NP is based on, the bin Root Mean Square (RMS) value from the mean value of raw accepted time of flight values minus the trend function, and meteorological information.

There is no routine available to directly establish the observations in the GEODYN-specific format from the CRD NP files. Consequently, the CRD NP files were converted to CSTG NP files (old format) using scripts written by R. Ricklefs⁴. The CSTG NP files were then converted to the International Laser Ranging Service (ILRS) fullrate format (formerly known as MERIT II). In a final step, the MERIT II formatted NP files were converted to the GEODYN II binary format (G2B).

¹a format description is available at http://ilrs.gsfc.nasa.gov/docs/2009/crd_v1.01.pdf

²<ftp://cddis.gsfc.nasa.gov>

³http://pds-geosciences.wustl.edu/lro/lro-1-rss-1-tracking-v1/lrors_0001/data/range/npt/

⁴downloaded from http://ilrs.gsfc.nasa.gov/data_and_products/formats/crd.html

D.2 From Doppler range-rates to GEODYN format

The Perl module `Astro::UTDF` was used to read the raw radiometric tracking data (`.TRK`), which are given in the binary Universal Tracking Data Format (UTDF), and to convert relevant information such as measurement time, tracking station, and Doppler range-rate to American Standard Code for Information Interchange (ASCII). See Table D.1 for an example of the created ASCII file.

Table D.1: Example for extracted ASCII data from raw range-rate observations that are given in the binary Universal Tracking Data Format. The extracted information includes the measurement time in UTC, emitting and receiving tracking stations (ID1 and ID2), and the range-rate observation in meter per second.

year	month	day	hour	minute	second	ID1	ID2	range-rate [m/s]
2011	01	03	18	55	00	119	119	-41.2380
2011	01	03	18	55	05	119	119	-41.0913
2011	01	03	18	55	10	119	119	-40.9536

The content of Table D.1 is expanded by weather data (temperature, atmospheric pressure, relative humidity) that are used by GEODYN for the computation of tropospheric correction. The weather data were retrieved from the PDS website⁵. One weather file (`.WEA`) contains relevant data for one tracked pass of one station, such as the UTC, the station which collected the weather data, temperature in degrees Celsius, atmospheric pressure in millibars, relative humidity in percent, and wind speed⁶ in km/hr. The interval of two successive weather data records within a pass is generally five minutes.

Two conclusions can be drawn from Figure D.1, which depicts Doppler observations from White Sands along with available weather data. First, weather data are not available for all tracking passes. Second, Doppler tracking data to LRO are available every five seconds whereas the weather data are available every five minutes. The latter is solved by performing a piece-wise interpolation of the weather data to the Doppler observation time. When-

⁵http://pds-geosciences.wustl.edu/lro/lro-1-rss-1-tracking-v1/lrors_0001/data/wea/

⁶wind speed is not used by GEODYN

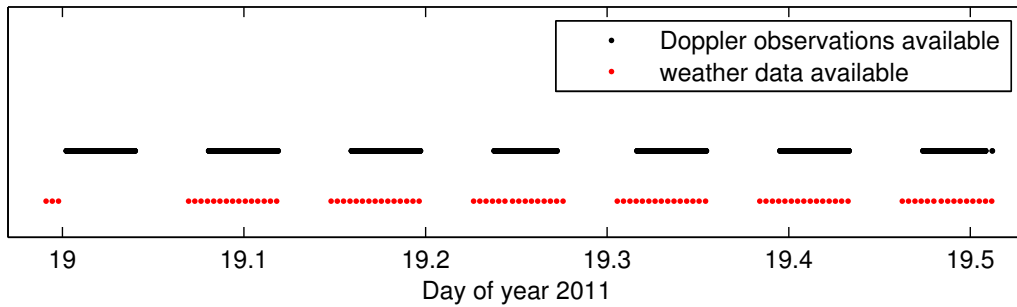


Figure D.1: Observed range-rates compared against available weather data for seven tracking passes of White Sands. Gaps in the weather data can occur. Mind the different step size (five seconds for range-rates, five minutes for weather data).

ever weather data are missing, as it is the case, e.g., for the first pass in Figure D.1, the weather data are set to zero. For all observations having no weather data available, GEODYN uses default values⁷.

The 12-column ASCII file (9 columns as in Table D.1 plus three columns for weather data) is converted to the GEODYN II binary metric tracking data format using a Formula Translating System (Fortran) routine. Finally, the tracking data formatter, which is part of the GEODYN/SOLVE software package, was used to convert the observations from the GEODYN II binary metric tracking data format to the GEODYN II binary format (G2B).

⁷temperature and relative humidity are set to 20°C and 40%, respectively; atmospheric pressure is computed by evaluating the expression $P_0 \times (1 + dPdH \times h)$, where P_0 is the mean sea level pressure, $dPdH$ is the lapse rate (change of pressure with height change), and h is the station height.

Appendix E

The SPICE module by NAIF

National Aeronautics and Space Administration (NASA)'s Navigation and Ancillary Information Facility (NAIF) provides a space geometry information system called Spacecraft Planet Instrument C-matrix Events (SPICE)¹ to assist scientists in planning and interpreting scientific observations from space-based instruments aboard robotic spacecraft (Acton, 1996). SPICE is offered in various computing languages. The author used it within the MATLAB environment. For the Lunar Reconnaissance Orbiter (LRO), numerous useful data files (also called kernels) are provided, such as

- the satellite's ephemeris and
- the attitude of the spacecraft bus, of the Solar Array (SA), of the High Gain Antenna (HGA) as well as the attitude of all instruments aboard LRO.

The author experienced the so-called geometry finder a very useful tool. With this tool it was possible to get a feeling of the overall geometry spanned by tracking stations on Earth, LRO, and the Sun. To give some examples, the geometry finder was used to

- extract the time intervals LRO is in line-of-sight of a specific station above a certain elevation angle. The stations of the Deep Space Network (DSN) are defined in the database. By using the program PINPOINT one can introduce stations that are not yet defined, such as White Sands and the stations of the Universal Space Network (USN),
- compute the solar beta angle, i.e. the angle between LRO's orbital plane and the Sun.

¹<http://naif.jpl.nasa.gov/naif/>

Moreover, SPICE proved useful for converting LRO's position from the J2000 system (GEODYN output) to the spacecraft reference frame in which the results of the overlap analysis are typically given.